

ULTRA-COLD COLLISIONS AND EVAPORATIVE COOLING OF CAESIUM IN A MAGNETIC TRAP

Angharad Mair Thomas

A thesis submitted in partial fulfilment of
the requirements for the degree of
Doctor of Philosophy at the University of Oxford



Jesus College
University of Oxford
Hilary Term 2004

ABSTRACT

Ultra-cold Collisions and Evaporative Cooling of Caesium in a Magnetic Trap

Angharad Mair Thomas, Jesus College, Oxford University

DPhil Thesis, Hilary Term 2004

Caesium-133 atoms have been evaporatively cooled in a magnetic trap to temperatures as low as 8 nK producing a final phase-space density within a factor of 4 of that required for the onset of Bose-Einstein condensation. At the end of the forced radio-frequency evaporation, 1500 atoms in the $F = 3, m_F = -3$ state remain in the magnetic trap. A decrease in the one-dimensional evaporative cooling efficiency at very low temperatures is observed as the trapped sample enters the collisionally thick (hydrodynamic) regime. Different evaporation trajectories are experimentally studied leading to a greater understanding of one-dimensional evaporation, inelastic collisions and the hydrodynamic regime. A theoretical simulation accurately reproduces the experimental data and indicates that the reduction in the evaporative cooling efficiency as the cloud enters the hydrodynamic regime is the main obstacle to the realization of Bose-Einstein condensation in the $F = 3, m_F = -3$ state.

In addition, we report measurements of the two-body inelastic collision rate coefficient for caesium atoms as a function of magnetic field and collision energy. The positions of three previously identified resonances are confirmed, with reduced uncertainties, at magnetic fields of 108.87(6), 118.46(3) and 133.52(3) Gauss. The resonance centred at 118.46 Gauss is also investigated as a function of temperature, thus demonstrating the dependence of the inelastic Feshbach resonance on collision energy. The importance of including partial waves of a higher basis in theoretical

closed channel calculations in order to accurately determine the line shape of a Feshbach resonance is also demonstrated.

ACKNOWLEDGEMENTS

This work could not have been carried out without the guidance and support of a vast number of people.

My first thanks must go to my supervisor Prof. Christopher Foot who provided me with the opportunity to work in his group and to study BEC which had first intrigued me as an undergraduate. I greatly appreciate the work he has done in reading through the various drafts of this thesis and for the suggestions and comments which have crystallized my understanding.

Where would I be without Dr. Simon Cornish? Probably still taking slosh data! His enthusiasm over the last three years has been boundless and his patience limitless. My enjoyment of my time here in Oxford has been in no small part due to his guidance and his friendship. He has also read my thesis carefully and offered advice and corrections in making the thesis intelligible.

I must also thank Prof. Paul Julienne (NIST) for the theoretical data he produced. If I absorb a hundredth of his understanding of ultra-cold collisions, it would then become my chosen specialist subject in Mastermind.

Thank you to the present and past members of the group for not only being willing to answer my questions, but actually answering them: Vincent, Gerald, Onofrio, Donatella, Rachel and Eleanor. Thanks also to all the other members of the group for providing some light in the dark basement.

The Clarendon staff must also be thanked for making my life easy: Sue, Graham, Terry, Dave and Alan in Stores, George and Rob in the Research Workshop, Reg and all in the Main Workshop, D.T. Smith and all at Central Electronics, Graham, Alan and Casper and everyone in maintenance.

Over the past three years I have been very fortunate to have many good friends. Special mention must go to Emma. Unsuccessful days in the lab were soon forgotten over a glass of wine and an episode of ‘Friends’. I must also thank Edward for his friendship and for proof-reading.

My last but by no means least thanks must go to my parents for their love and continual support. Diolch yn fawr iawn am bopeth.

I must finish these acknowledgments with some words taken from the lab song:

“No one said it would be easy”

Sheryl Crow *Tuesday Night Music Club* (1993).

CONTENTS

1	Introduction	1
1.1	Bose-Einstein Condensation	1
1.1.1	Bosons and Fermions	2
1.1.2	Bose-Einstein Condensation	3
1.1.3	Experimental Observation	4
1.1.4	Current Experiments	5
1.2	Caesium: State of Play – October 2000	6
1.2.1	$F = 4, m_F = +4$	7
1.2.2	$F = 3, m_F = -3$	9
1.2.3	$F = 3, m_F = +3$	11
1.2.4	Recent Collisional Studies	13
1.3	Overview of Thesis	17
1.3.1	Notation	17
1.3.2	Abbreviations Used in Thesis	18
1.3.3	Constants and Conversion Factors	18
1.3.4	Prior Publication of Work in this Thesis	18
2	BEC: An Experimentalist’s Guide	21
2.1	The Recipe for Creating a BEC	21
2.2	Laser Cooling	23
2.2.1	Alkali Metals	23
2.2.2	Doppler Cooling	26

2.2.3	Sub-Doppler Cooling	27
2.3	Magneto-Optical Traps	31
2.3.1	Six-Beam MOT	31
2.3.2	Pyramidal MOT	33
2.4	Magnetic Trapping	34
2.4.1	Zeeman Effect on the Hyperfine Ground States	34
2.4.2	Simple Magnetic Trap	35
2.4.3	Majorana Transitions	36
2.4.4	Ioffe-Pritchard Trap	37
2.4.5	Baseball Trap	39
2.4.6	Experimental Considerations	40
2.5	Evaporative Cooling	41
2.5.1	Radio-Frequency Evaporation	41
2.5.2	Effects of Gravity on Evaporation	42
2.5.3	Dimensionality of Evaporation	44
3	Scattering Theory and Feshbach Resonances	46
3.1	Atomic Interactions	46
3.1.1	Unperturbed Hamiltonian	47
3.1.2	van der Waals Interaction and Exchange Terms	47
3.1.3	Dipolar Interaction	50
3.2	Scattering	52
3.2.1	Partial Wave Analysis	52
3.2.2	Scattering Length	54
3.2.3	Scattering at Low Temperatures	55
3.3	Resonances	56
3.3.1	Potential Resonances	57
3.3.2	Feshbach Resonances	59
4	Evaporative Cooling	62
4.1	Elastic and Inelastic Collisions	63

4.1.1	Elastic Collisions	63
4.1.2	Inelastic Collisions	63
4.2	Efficiency of Evaporation	65
4.2.1	Hydrodynamic (Collisionally thick) regime	67
4.3	Evaporative Cooling Models	69
4.3.1	Simple Model of Evaporative Cooling	70
4.3.2	Monte-Carlo Simulation	71
4.4	Evaporation Strategy	76
5	Experimental Apparatus	77
5.1	Apparatus	77
5.1.1	Lasers	77
5.1.2	Frequency Stabilization - DAVLL	81
5.1.3	The Optical Table	88
5.1.4	Vacuum System	91
5.1.5	Pyramidal MOT	92
5.1.6	2nd MOT – Experimental MOT	95
5.1.7	Magnetic Trap	97
5.1.8	Evaporation	104
5.2	Control	104
5.2.1	Experimental Synchronization	104
5.2.2	Analogue Voltages	105
5.3	Diagnostics	107
5.3.1	Recapture	107
5.3.2	Absorption Imaging	108
5.3.3	Comparison of Recapture and Imaging	112
5.4	Optimization and Characterization	113
5.4.1	Pyramidal MOT	113
5.4.2	Experimental MOT	114
5.4.3	Loading the Experimental MOT	114

5.4.4	Compressed MOT and Molasses	117
5.4.5	Optical Pumping	119
5.4.6	Calibration of Magnetic Trapping Parameters	120
6	Loss Measurements	124
6.1	Inelastic Feshbach Resonances	125
6.1.1	Comparison of Theoretical and Experimental Data	125
6.2	Feshbach Resonances in the $F = 3, m_F = -3$ State	126
6.2.1	Determination of the Two-Body Inelastic Collision Rate Coefficient	126
6.2.2	Experimental Results	127
6.3	Temperature Dependence of the 118.5 G Resonance	130
6.3.1	Experimental Results	130
6.3.2	Theoretical Results	133
6.3.3	Experimental and Theoretical Results	135
6.3.4	Discussion	139
7	Evaporation Results	141
7.1	Initial Evaporative Cooling Attempt	142
7.1.1	Experimental Procedure	142
7.1.2	Results	144
7.2	Two-Frequency Evaporation	148
7.2.1	Experimental Procedure and Results	149
7.2.2	Discussion	150
7.2.3	Heating	153
7.3	Very Weak Trap	155
7.3.1	Experimental Procedure	155
7.3.2	Data Analysis	157
7.3.3	Results	159
7.3.4	Discussion	161

8 Conclusion	163
8.1 Outlook	164
A Bose-Einstein Condensation in Caesium	167
A.1 Experimental Setup	167
A.2 Evaporation	168
A.3 Comparison	171
B Experimental Equipment Details	173
B.1 Computer Control Boards	173
B.2 Electronic Equipment Details	174
C Caesium Atomic Data and Experimental Equations	175
C.1 Atomic Parameters	175
C.2 Magnetic Field Calculations	175
C.3 Number of Atoms	176

Introduction

Since the earliest observations of Bose-Einstein condensation (BEC) in 1995 [1, 2, 3], numerous groups have observed quantum degeneracy in many different elements: rubidium (isotopes ^{87}Rb [1] and ^{85}Rb [4]), sodium [2], lithium (^7Li [3] and ^6Li [5, 6]), hydrogen [7], helium [8, 9] and potassium (^{41}K [10] and ^{40}K [11]). Until very recently [12], a notable omission from this list was the alkali metal caesium.

What is Bose-Einstein condensation and why is it such an active area of research?

1.1 Bose-Einstein Condensation

Bose-Einstein condensation was predicted in 1925 by Albert Einstein following work by Satyendra Nath Bose. Bose derived the Planck's black body radiation law from Boltzmann statistics [13] by proposing that: photons could occupy different states, photon number was not conserved and that by putting particles into cells that there existed statistical independence of cells rather than particles. Initially, the paper was rejected. However Bose then sent Einstein a copy of the paper, who realised the importance of the work and arranged for it to be published. Einstein then applied Bose's results to material particles which are conserved, and published many papers describing the statistics of these systems [14]. The consequence of the work by Bose and Einstein was the prediction that a large occupation of particles in

the ground state can occur. For low-density systems (approximately 10^{14} cm^{-3}),¹ the temperature at which quantum degeneracy is observed must be of the order 10^{-5} K or less.

1.1.1 Bosons and Fermions

Bosons are particles which have integer spin: the angular momentum of the particles is $0, \hbar, 2\hbar, 3\hbar \dots$. A large proportion of atoms and all of the force carrying particles (e.g. photons) are bosons. Fermions are particles which have half-integer spin: the angular momentum of the particles is $\hbar/2, 3\hbar/2, 5\hbar/2 \dots$. Most of the elementary building blocks of matter are fermions e.g. protons, neutrons, electrons. Fermions obey the Pauli exclusion principle and therefore cannot occupy the same quantum state, whereas there is no exclusion on the states a boson can occupy.²

Systems of bosons and fermions are described by different distributions. The equations for these are given below (Equation 1.1). It is the presence of ± 1 in the denominator that makes the physical results of these distributions so different from one another.

$$n_i = \begin{cases} \frac{1}{\exp((\varepsilon_i - \mu)/k_B T)} & \text{Maxwell - Boltzmann distribution} \\ \frac{1}{\exp((\varepsilon_i - \mu)/k_B T) - 1} & \text{Bose - Einstein distribution} \\ \frac{1}{\exp((\varepsilon_i - \mu)/k_B T) + 1} & \text{Fermi - Dirac distribution} \end{cases} \quad (1.1)$$

where n_i is the average number of particles occupying a state i of energy ε_i and μ is the chemical potential (the amount of energy required to add a particle to the system).

¹Dilute gases are an example of low-density systems.

²In actual fact the presence of a boson in a quantum state increases the probability that another boson will go into this state.

1.1.2 Bose-Einstein Condensation

For a thermal collection of atoms, a large number of states are occupied. If the temperature is lowered to below $\hbar\omega$ (where ω is the angular frequency of single particle motion in a harmonic oscillator potential), most of the atoms in a system are in the ground state. However, at a particular temperature called the critical temperature (T_c), a large number of bosons occupy the ground state even when the temperature is high enough for atoms to populate other states. Bose-Einstein condensation is a quantum phenomena and it is the behaviour of bosons that makes BEC possible.

According to wave-particle duality atoms have an associated wavelength, the deBroglie wavelength:

$$\lambda_{\text{dB}} = \left(\frac{h^2}{2\pi m k_B T} \right)^{1/2} \quad (1.2)$$

As atoms become colder their deBroglie wavelength increases. Bose-Einstein condensation occurs when the deBroglie wavelength is comparable to the inter-particle separation ($n^{-1/3}$) and the wavefunctions of the atoms overlap. The condition for BEC for a gas in free space is when the phase-space density (PSD) exceeds 2.612:

$$n\lambda_{\text{dB}}^3 \geq 2.612 \quad (1.3)$$

where n and T (Equation 1.2) are the density and temperature of the gas respectively. In BEC experiments a dilute vapour is non-uniform as the atoms are contained in a trap. The critical temperature T_c is given by:

$$k_B T_c = 0.94 \hbar \omega N^{1/3} \quad (1.4)$$

To illustrate that BEC occurs when the temperature is high enough for occupation of many harmonic oscillator states, $N = 1 \times 10^6$ is substituted into Equation 1.4:

$$k_B T_c \approx 100(\hbar\omega)$$

Condensation can occur even when 100 harmonic oscillator states are occupied. If ω is $1 \times 10^3 \text{ s}^{-1}$ then the critical temperature is $4.5 \mu\text{K}$.

For an ideal system, the wavefunction of a BEC of N atoms is the product of N single particle wavefunctions. For a cloud of atoms with interactions, the non-linear Schrödinger equation includes a term due to the mean-field energy (U_0) of the condensate:

$$U_0 = \frac{4\pi\hbar^2 na}{m} \quad (1.5)$$

where a is the scattering length (see Chapter 3). The sign of a and therefore the mean-field energy determines the stability of a condensate. For a positive a the interactions are repulsive and therefore the condensate can be arbitrarily large. In contrast, for a negative a the interactions are attractive and the condensate is unstable for a large number of atoms.

1.1.3 Experimental Observation

In 1938 Fritz London suggested that the observation of superfluidity when helium-4 was cooled to its lambda point³ could be attributed to Bose-Einstein condensation. London's suggestion met with skepticism as Einstein's theory predicted condensation for non-interacting particles whereas the atoms interact strongly in liquid helium. The helium system is difficult to understand on an elementary level because of the strong interactions therefore it was a long-sought goal to observe Bose-Einstein condensation in a vapour.

The signature of BEC is the appearance of a narrow peak in both coordinate and momentum space. When a condensate is confined in an elliptically shaped potential, on release from the magnetic trap the short direction expands faster than the long direction and therefore after a time the cloud is elongated in the previously short direction. There are two factors that cause the aspect ratio to be inverted: the dominant effect in normal BEC experiments is the repulsive inter-atomic interactions while the Heisenberg uncertainty principle⁴ is dominant in non-interacting condensates. A thermal cloud does not behave in this manner and therefore upon release from the magnetic trap it becomes isotropic in space.

³The lambda point is equivalent to the critical temperature in dilute gases.

⁴The more precisely the position is determined, the less precisely the momentum is known.

It took until 1995 for Bose-Einstein condensation in a gas to be observed [1, 2, 3]. A dilute atom vapour condensate can be described as a near ideal gas (weakly interacting system) as the inter-particle separation is much larger than the particle size. The observation of a gaseous condensate created a test bed for theories that described non-interacting systems.

1.1.4 Current Experiments

Since the observation of BEC in 1995, the research field has grown and blossomed. The paths which the experiments have taken are many and diverse. For example, a demonstration of an atom laser⁵ has already been observed at MIT [15]. The areas of physics involved in some aspect of BEC research already include: atomic physics, quantum optics, statistical mechanics, condensed matter physics and quantum computing.

The first observation of a Feshbach resonance in a BEC [16] led to some very exciting physics. Atom-atom interactions could be tuned leading to the possibility of examining repulsive, attractive and non-interacting systems. The existence of a Feshbach resonance in the scattering structure of ^{85}Rb allowed for the creation of a BEC [4]. Using the magnetic tunability of the Feshbach resonance the ^{85}Rb group at JILA have studied the collapse of the condensate [17, 18] and have created a quantum superposition of atoms and diatomic molecules [19].

The most recent developments have been the creation of molecular condensates by groups at Innsbruck [5], JILA [20], and MIT [6]. Each group starts with a cloud of Fermi atoms (^6Li at Innsbruck and MIT, ^{40}K at JILA) and evaporatively cool their sample before creating molecules and detecting them by use of a Feshbach resonance. Molecules cannot be imaged directly and therefore the existence of molecules is inferred by imaging the atoms created by disassociating the molecules by sweeping the magnetic field across a Feshbach resonance.

Condensation of fermionic atom pairs in the BCS-BEC crossover regime has been observed [11]. The previous experiments had demonstrated BEC of molecules

⁵Atoms in a BEC are coherent due to the overlap of the atoms' individual wavefunctions.

which is the extreme end of the BCS-BEC crossover and is created by approaching the Feshbach resonance from the positive scattering length side of the resonance. Jin *et al.* observe condensation on the other side of the resonance ($a < 0$). On this side the formation of dimers is not supported and therefore condensation occurs due to many-body effects. The observation of a condensate of fermionic atom pairs occurred at the beginning of 2004, paving the way for studies of superfluidity (the crossover between conventional superfluidity and the superfluidity of molecules), and created another novel system for the testing of theories. 2004 promises to be another year of exciting and valuable physics.

This is the current situation, however what was the situation when this work began? The next section is a review of the work to condense caesium since the early days of BEC experiments.

1.2 Caesium: State of Play – October 2000

Caesium, a heavy alkali metal atom, is well suited to laser cooling experiments because of its small photon recoil (see Table 1.1 for the atomic parameters of ^{133}Cs). The low temperatures that had been attained in laser cooling experiments made caesium an obvious choice, not only for BEC experiments but for cold atom studies.

Electronic Configuration	$[\text{Xe}]6s^1$
Atomic Number	55
Atomic Weight	132.905
Nuclear Spin, I	$7/2$

Table 1.1: Atomic parameters of caesium-133

The benefits of using slow atoms for precision spectroscopy have been recognized for many years. By using laser cooled Cs atoms at μK temperatures, the accuracy and stability of the caesium frequency standards were improved by two to three orders of magnitude [21]. However, the nature of Cs collisions at low temperatures is unusual. In the ultra-cold regime, the deBroglie wavelength is larger than

the scale of the interatomic potential. The scattering is therefore quantum mechanical in nature and is usually dominated by the lowest allowed partial angular momentum wave (*s*-waves) [22]. It is important to understand these ultra-cold collisions as sizeable frequency shifts between the two hyperfine states of the ground state of Cs (the so-called “clock transition”) can occur and affect frequency standards. The telecommunications industry relies heavily on timing and therefore frequency shifts in the “clock transition” cause inaccuracy. Also, most other units, including the metre, are defined in terms of the second.⁶

The study of ultra-cold collisions is not only useful for metrologists, but also for BEC experimentalists. Understanding inter-atomic collisions is important for the optimization of the evaporation of an atom cloud.

Caesium was the early leader in the race to BEC due to the low temperatures that had been achieved by laser cooling alone, and was also predicted to have favourable scattering properties for Bose condensation in the (3, −3) state [23]. However, it was soon overtaken by most of the other alkali metals. Why was caesium so difficult to condense?

1.2.1 $F = 4, m_F = +4$

The early experimental attempts to Bose-condense caesium focussed on the magnetically trappable $F = 4, m_F = +4$ state where the destructive spin relaxation process is forbidden (see Section 3.1, Chapter 3). Instead, the dominant loss mechanism was expected to be the much weaker dipole relaxation occurring through the magnetic dipole-dipole interaction.

However, attempts at evaporative cooling of atoms in this state failed completely. The highest PSD attained was 10^{-5} for a cloud at a temperature of $4 \mu\text{K}$ [24]. The failure could not be attributed to background gas collisions or heating due to experimental noise e.g. stray light, noise on magnetic fields etc. It therefore became clear that the collisional behaviour was far from what had been anticipated. Attention then turned to measuring the elastic and inelastic

⁶The second is defined as the duration of 9,192,631,770 periods of the radiation corresponding to the transition between two hyperfine levels of the ground state of the caesium-133 atom.

collision rate coefficients for ^{133}Cs in the $F = 4$, $m_F = +4$ state [25, 26]. Two-body inelastic collision rate coefficients for other cold alkali metals such as lithium, sodium and rubidium in their doubly-polarized state ranged from 6 to $20 \times 10^{-15} \text{ cm}^3 \text{ s}^{-1}$ [27, 28, 29]. It was predicted that the value for doubly-polarized Cs would be in the same range [30, 23].

Foot *et al.* (Oxford) studied the two-body inelastic collisions at a magnetic field of 7 G [31]. At a temperature of $30 \mu\text{K}$ they obtained a value for K_2 of $1.2 \times 10^{-11} \text{ cm}^3 \text{ s}^{-1}$ [26]. In a supplementary experiment they allowed the cloud to evolve in the magnetic trap and periodically probed the cloud with σ^+ light on the $F = 4 \rightarrow F' = 5$ transition. They observed an increase in the atom number compared to when the cloud was allowed to evolve in the dark in the magnetic trap. Graphs of number plotted against time for both cases gave a non-exponential decay for the non-probing case and a purely exponential decay for the probed case. Non-exponential behaviour is a signature of a multi-body decay process. This implied that the two-body inelastic loss rate had been completely suppressed. The conclusion was that at fields of $\approx 7 \text{ G}$, decay to other m_F states was occurring. This seemed to agree with the observation of a zero-energy resonance [25].

Dalibard and co-workers (ENS, Paris) measured a value for the two-body inelastic collision rate coefficient, K_2 [24]. After allowing a cloud of atoms in the $(4, +4)$ state to relax in the magnetic trap they imaged the cloud and plotted atom number against evolution time. The evolution of the atom number exhibited non-exponential behaviour. The value obtained for the two-body inelastic collision rate coefficient at a magnetic field of 1.5 G and at temperatures ranging from 8 to $70 \mu\text{K}$ was:

$$(1.5 \pm 0.3 \pm 0.3) \times 10^{-11} T^{-0.63} \text{ cm}^3 \text{ s}^{-1}$$

Therefore at a temperature of $8 \mu\text{K}$, the two-body inelastic collision rate coefficient is $4 \times 10^{-12} \text{ cm}^3 \text{ s}^{-1}$. This value is three orders of magnitude higher than the predicted value [23, 30]. The experimental value obtained was also the same order of magnitude as the two-body inelastic collision rate coefficient for unpolarized

$F = 4$ atoms. However, that rate could be accounted for by spin relaxation. Dalibard and co-workers then postulated that the atoms were decaying via hyperfine changing collisions. To validate the postulate they performed another experiment. Before imaging the atoms they reduced the field gradient of the magnetic trap to a value that still trapped the $m_F = 4$ state but not the other m_F states. If other substates were present in the trap they would be seen at a different position on the CCD array as they fell under the influence of gravity. However, no extra clouds were observed. To check their results they performed the same experiment again but this time with a cloud of $F = 4$ depolarized atoms. Images taken this time showed small clouds of atoms falling under the influence of gravity. These clouds corresponded to the $m_F = 3, 2, 1$ states. This confirmed that nearly all the atoms were lost via hyperfine-changing collisions. They explained this observation in two complementary fashions. Firstly, the presence of a zero-energy resonance [25] increases the two-body inelastic collision rate. Secondly, for heavy alkali metals, dipole relaxation can occur due to the second-order spin-orbit interaction (Section 3.1, Chapter 3). The second-order spin-orbit interaction was neglected from early predictions [23, 30] but recent calculations that take this effect into account reproduced the results of References [24, 25]. This behaviour completely explained why evaporative cooling does not work in the $F = 4, m_F = 4$ state.

1.2.2 $F = 3, m_F = -3$

Following the realization that the two-body inelastic loss rates were too high to achieve BEC in the $F = 4, m_F = +4$ state, attention turned to the lower hyperfine state and the magnetically trappable $F = 3, m_F = -3$ state. It had been shown that this state had favourable scattering properties for BEC and it was also predicted that it would show pronounced resonance structure [23]. This meant that by varying the magnetic field it would be possible to vary the magnitude and sign of the atom-atom interactions.

Monroe *et al.* had measured the elastic collision cross-section and the two-body inelastic collision rate coefficient for spin polarized atomic caesium in 1993 [32].

A value of $1.5(4) \times 10^{-12} \text{ cm}^2$ for the zero-energy s -wave elastic cross-section was obtained and it was stated that the cross-section was independent of temperature between 30 and 250 μK . An upper limit of $5 \times 10^{-14} \text{ cm}^3 \text{ s}^{-1}$ was put on the two-body inelastic collision rate coefficient. Tiesinga *et al.* calculated the two-body inelastic collision rate coefficient, and obtained a value of $1 \times 10^{-15} \text{ cm}^3 \text{ s}^{-1}$ [23], which was consistent with, although much smaller than the upper limit obtained previously. It was suggested that the limiting loss process was not dipole relaxation or molecular formation but collisions with background gas [32].

Initial attempts to condense Cs in the $F = 3$, $m_F = -3$ state failed because the inelastic loss rates were still unusually high. However, the suppression of the dipole relaxation collisions as the magnetic field tends to zero (Section 3.1.3, Chapter 3) meant there was some experimental success, most notably in Paris [33] and Oxford [26]. Although the experiments used different trapping geometries,⁷ both worked at low magnetic fields around 1 G to take advantage of the suppression of the two-body inelastic collisions. The group in Paris simulated their evaporation [34] and predicted that they would obtain BEC with over 5 000 atoms. Unfortunately, they only achieved a PSD of 3×10^{-2} , two orders of magnitude below the condensation threshold. Both groups concluded that the efficiency of evaporation was insufficient for obtaining BEC because the rate of two-body inelastic collisions was still too high. Subsequent analysis by ourselves illustrated that the atom cloud was entering the hydrodynamic regime in the last evaporation stages of their experiments (Section 4.2.1, Chapter 4).

Study of the two-body inelastic losses showed that the dipole relaxation rate increased rapidly with increasing magnetic field between 1 and 7 G [35]. It was suggested that this increase could be due to the existence of a Feshbach resonance close to $B = 0 \text{ G}$ [36].

The magnitude and sign of the scattering length for the $(3, -3)$ state was determined in 2000 [37, 38] and confirmed the earlier prediction of the existence of

⁷The Oxford experiment used a time-averaged orbiting potential (TOP) trap with $\omega_{\text{trap}} = 23 \text{ Hz}$ and $B < 1 \text{ G}$. The Paris experiment operated a Ioffe-Pritchard (I-P) type trap with $\omega_{\text{trap}} = 38 \text{ Hz}$ and $B = 1.2 \text{ G}$.

a Feshbach resonance close to $B = 0$ G.⁸ The scattering length of Cs in the $(3, -3)$ around 1 G is large and negative which explained the failure to condense Cs in the experiments operating at approximately 1 G.

1.2.3 $F = 3, m_F = +3$

Following the failure to condense caesium in any of the weak-field seeking states, recent attempts, including Salomon – ENS Paris [39], Vuletic and Chu – Stanford [40], Weiss – formerly at Berkeley [41] and Grimm – formerly at Heidelberg [42], turned towards dipole force trapping of the $F = 3, m_F = +3$ state. As this is the lowest energy magnetic sublevel, inelastic two-body collisions are energetically forbidden.

Salomon *et al.* used a Raman cooling scheme in a red-detuned crossed dipole trap to simultaneously cool and polarize ^{133}Cs atoms. They achieved a temperature of $2.4\ \mu\text{K}$ with 2.5×10^4 atoms in the $(3,+3)$ state. This corresponds to a PSD of 10^{-3} [39]. They believed that the highest PSD they achieved was limited by multiple photon scattering in the atomic cloud.

Vuletic/Chu *et al.* achieved temperatures close to the photon recoil limit in a 3D far-detuned optical lattice. They succeeded in transferring 95 % of the atoms from the MOT into the lattice while simultaneously spin-polarizing and cooling the atoms. The cooling is achieved with 3D degenerate Raman sideband cooling. They attained temperatures of 290 nK with 3×10^8 atoms (80 % of these atoms are in the lowest vibrational bands of the lattice) at a density of $1.1 \times 10^{11}\ \text{cm}^{-3}$. This corresponds to a PSD of $1/500$ [40]. This experiment succeeded in laser-cooling a large number of caesium atoms to a high phase-space density.

Weiss *et al.* laser-cooled 5×10^7 Cs atoms to a PSD of $1/30$. This was achieved in a 3D far-off-resonant lattice (FORL). They compressed the cloud and performed polarization gradient cooling followed by 3D Raman sideband cooling. In a FORL the heating due to rescattered photons is suppressed when the vibrational frequency exceeds the light scattering rate [43]. The highest PSD that could be

⁸The actual position of the resonance is -17 G.

obtained was limited by photon rescattering. However, they predicted that with consideration of the depth of the FORL and careful application of laser cooling they could achieve BEC with laser cooling alone.

Grimm *et al.* implemented two different experiments in order to pursue the quest of condensing caesium.⁹ The first experiment is a gravito-optical surface trap (GOST) [44], where atoms are cooled above an evanescent-wave atom mirror. They start with approximately 10^7 atoms at a temperature of $10\ \mu\text{K}$. Following an evaporation stage they reach a temperature of $300\ \text{nK}$ with 3×10^4 atoms remaining. This corresponds to a PSD of 3×10^{-4} . This PSD could be increased by a factor of 7 if the atoms were polarized into the $F = 3$, $m_F = +3$ state. The main advantages of a GOST is that it has a large trapping volume and therefore many atoms can be captured. Following this experiment they implemented a double evanescent-wave (DEW) trap [45] and achieved a temperature of $100\ \text{nK}$ with 20 000 atoms at a PSD close to 0.1. The experiment was limited mainly by two factors. Firstly, the atoms were not polarized and therefore two-body inelastic collisions were causing heating and trap loss. Secondly, when the dimensionality of the atom cloud was approaching two, atoms were not being evaporated out of the trap vertically. To overcome these difficulties involved two modifications. Polarizing the atoms into the $F = 3$, $m_F = +3$ state would not only eliminate two-body inelastic collision loss but would allow for the tuning of the scattering length using magnetic fields. Also, magnetic field gradients could compensate for gravity allowing for evaporation vertically from the trap.

Their second experiment is evaporation of caesium in a quasi electrostatic dipole trap (QUEST). Cs atoms are trapped in the focus of a CO_2 laser beam. A CO_2 laser has a wavelength of $10.6\ \mu\text{m}$ which is far from any optical transitions from the ground state of Cs. This has two main advantages: the optical potential becomes quasi electrostatic which means that different atomic species and even molecules can be confined in the trap and, because of the large detuning from resonance, the photon scattering rate is negligibly small and therefore heating

⁹Both schemes have now succeeded in condensing Cs (Appendix A).

associated with photon momentum recoil which normally occurs in dipole traps is suppressed. In the year 2000, Grimm *et al.* observed a reduction in temperature of approximately a factor of two over approximately 150 s. This was due to plain evaporation i.e. evaporation from a trap at constant trap depth. There were three fundamental problems prohibiting further progress towards condensing Cs. The first was that the cross-section is temperature dependent which increases the thermalization time [25]. The second problem was gravity. The presence of gravity can make evaporation one-dimensional leading to a reduction in the efficiency of the evaporation [46](see Chapter 4). The third problem was the high rate of inelastic loss due to three-body collisions.

In 2002, Grimm and co-workers at Innsbruck overcame the difficulties and successfully condensed caesium into the absolute ground state [12]. Crucial to their success is the implementation of an efficient final stage of evaporative cooling to combat the three-body problems.¹⁰

1.2.4 Recent Collisional Studies

The early experiments took place during a period when the collisional properties of caesium were poorly understood, because of a combination of a lack of experimental data and difficulty in calculating the properties for such a large atom. The van der Waals coefficient C_6 [47] and the magnitude of the indirect spin-spin coupling [48] were not known and therefore it was impossible to even determine whether the atom-atom interactions were repulsive or attractive. However, in the year 2000, two papers were published which stated accurately for the first time the cold-collision properties of ^{133}Cs .

Vuletic/Chu *et al.* observed over 25 resonances in the magnetic field range 0 to 230 G and accurately measured the positions of these resonances to within 30 mG [38]. Feshbach spectroscopy has a high resolution because it only involves electronic ground states and is therefore limited solely by the temperature of the sample. They have the ability to prepare atoms in various hyperfine and magnetic

¹⁰Appendix A contains a description of the experiment at Innsbruck, and a comparison of the problems and results in Innsbruck and Oxford.

sublevels and they can probe different parts of the molecular potential. They observed that the $(4, +4)$ state has no resonance and that at a temperature of $5\ \mu\text{K}$ the two-body inelastic collision rate coefficient is $2 \times 10^{-12}\ \text{cm}^3\ \text{s}^{-1}$ which is in agreement with the value given in Reference [24].

The subsequent theoretical analysis at NIST, Gaithersburg provided for the first time an accurate characterization of the collisional properties of caesium [37]. They extracted values for the singlet and triplet scattering lengths and a value for the van der Waals coefficient. These values are given in Table 1.2.

Name	Symbol	Value
Singlet scattering length	$X^1\Sigma_g^+$	$280 \pm 10\ a_0$
Triplet scattering length	$a^3\Sigma_u$	$2400 \pm 100\ a_0$
van der Waals coefficient	C_6	$6890 \pm 35\ \text{a.u.}$

Table 1.2: Values for the collisional properties of caesium [37].

The value obtained for the $F = 4$, $m_F = 4$ scattering length was $2400 \pm 100\ a_0$ which was not only different in magnitude but also in sign to what had been predicted previously [23, 30, 36].

To model the resonances Leo *et al.* [37] used a coupled channel theoretical model similar to the model described in References [48, 49]. Their analysis reproduced all of the $(3, -3) \times (3, -3)$ inelastic resonances between 0 and 250 G. Figure 1.1 is a plot of the scattering length, two-body inelastic losses, and the elastic collision rate coefficient against magnetic field for the $(3, -3)$ state. The magnitude of the two-body inelastic collision rate coefficient for ^{85}Rb at 162.5 G is also included on the plot.¹¹ This clearly illustrates the difficulties facing experimentalists attempting to condense Cs as the two-body inelastic collision rate coefficient in the $(3, -3)$ state is an order of magnitude greater than for ^{85}Rb which is considered to be a challenging isotope to condense.

The theoretical analysis predicted two-body collisional properties with a high degree of confidence and suggested that ^{133}Cs $F = 3$, $m_F = |3|$ possessed suitable

¹¹The ^{85}Rb experiment at JILA evaporate at a magnetic field of 162.5 G.

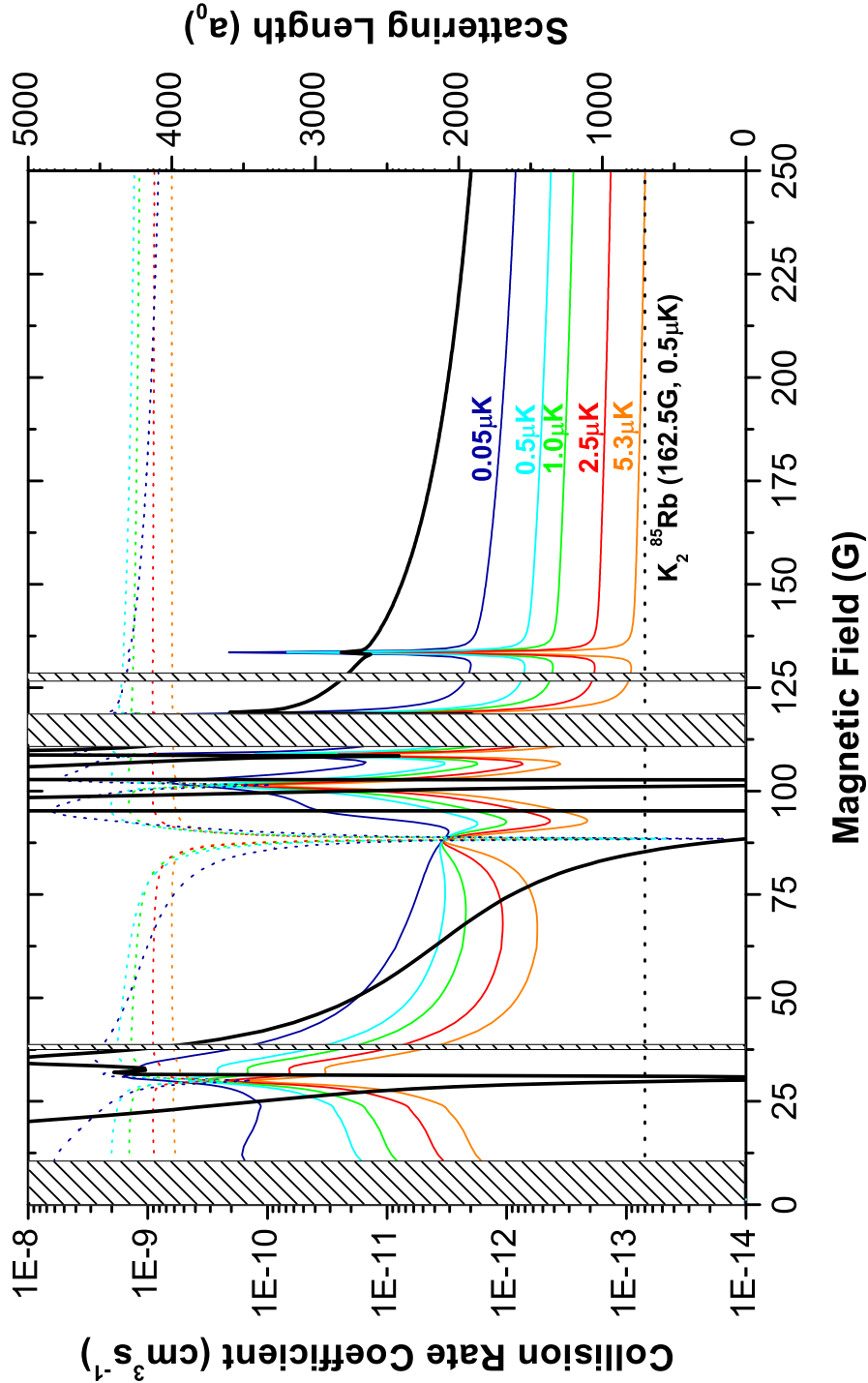


Figure 1.1: The solid and dotted coloured lines denote the two-body inelastic collision rate coefficient (K_2) and the elastic collision rate coefficient respectively at the given temperatures. The thick black line denotes the scattering length. The shaded sections illustrate where the scattering length is negative. For comparison, the dotted line at a value of $K_2 = 7 \times 10^{-14} \text{ cm}^3 \text{ s}^{-1}$ is the two-body inelastic collision rate coefficient for ^{85}Rb at 162.5 G and at a temperature of $0.5 \mu\text{K}$. Data for the figure obtained from [50].

scattering properties for BEC [37].

1.3 Overview of Thesis

The aim of the work carried out in this thesis was to condense caesium in a magnetic trap. A new experiment was built in order to pursue this quest – the general discussion of the techniques is given in Chapter 2 while the experimental details are given in Chapter 5.

To decide on the evaporation strategy it is crucial to understand the nature of the inter-atomic collisions. Chapter 3 describes the origin of some of the scattering properties of caesium. It includes a description of the inter-atomic potential, the origin of elastic and inelastic collisions and the occurrence of resonances, both potential and Feshbach resonances. Three Feshbach resonances were observed and characterized during this work. The temperature dependence of one of these resonances was also studied. These results are given in Chapter 6.

In many alkali metal BEC experiments, there is a great tolerance in the choice of magnetic trap and magnetic trapping parameters.¹² For caesium however, because of the high inelastic losses, the choice of magnetic trap and especially the magnetic trapping parameters has a large effect on the evaporation performance. Chapter 4 is a discussion of the theoretical principles of evaporative cooling. It includes a summary of the elastic and inelastic losses in a trapped atom cloud, the effect that trap frequencies and the scattering length has on these losses, and the methods used to simulate the evaporation. The experimental results of our attempt to condense caesium are included in Chapter 7.

1.3.1 Notation

Some of the less obvious notations used in the thesis are given below:

- When the phase-space density (PSD) is stated, the value is normalized so that the BEC transition in a confining potential occurs at a PSD of unity.
- When the rf power is quoted, it is value of the output power of the rf synthe-

¹²To achieve BEC there must be no $B=0$ G in the magnetic potential. It is also beneficial to have a tight trap to increase the efficiency of the evaporation.

sizer before the amplifier unless stated otherwise. The amplifier has a gain of 40 dB.

- When discussing electrons, unless otherwise stated, the comment refers to the valence electron.
- The magnetic field is always expressed as B with units of Gauss ($\equiv 10^{-4}$ T).
- The current is always quoted in Amperes (A).
- Vector quantities are represented by bold characters.
- An atom cloud, cloud of atoms etc. refers to a collection of atoms trapped in or released from a magnetic trapping potential.

1.3.2 Abbreviations Used in Thesis

Many abbreviations are used throughout the thesis. The first mention of an abbreviation is always accompanied with the full name, however for completeness Table 1.3 contains all of the abbreviations used in this work.

1.3.3 Constants and Conversion Factors

Table 1.4 contains all the common constants and conversion factors used in the thesis. Table C.1, Appendix C contains all the values for the relevant atomic properties of caesium.

1.3.4 Prior Publication of Work in this Thesis

Several of the results described in this thesis have been published in journals. Section 6.2.2, Chapter 6 and Section 7.1, Chapter 7 appears in Reference [51]. The work in Section 7.3, Chapter 7 appear in Reference [52].

AOM	-	Acousto-optic modulator
PZT	-	Piezoelectric transducer
FET	-	Field effect transistor
swg	-	Standard wire gauge
TTL	-	Transistor-transistor logic
PSD	-	Phase-space density
rf	-	Radio-frequency
JILA	-	Joint Institute of Laboratory Astrophysics
NIST	-	National Institute of Standards and Technology
MIT	-	Massachusetts Institute of Technology
BEC	-	Bose-Einstein condensation
GPIB	-	General purpose interface bus
PCI	-	Peripheral component interconnect
CCD	-	Charge-coupled device
FWHM	-	Full width at half maximum
TOP	-	Time-averaged orbiting potential
NEG	-	Non-evaporable getter
MOT	-	Magneto-optical trap
CMOT	-	Compressed magneto-optical trap
OP	-	Optical pumping
DSPOT	-	Dark spontaneous-force optical trap
3D	-	Three-dimensional
DEW	-	Double evanescent-wave
FORL	-	Far-off-resonant lattice
GOST	-	Gravito-optical surface trap
I-P	-	Ioffe-Pritchard
QUEST	-	Quasi electrostatic dipole trap
MOPA	-	Master oscillator power amplifier
ECDL	-	External cavity diode lasers
rms	-	Root mean square
DAVLL	-	Dichroic atomic vapour laser lock
TOF	-	Time-of-flight
OD	-	Optical depth

Table 1.3: Abbreviations used in thesis

1 Tesla	\equiv	10^4 Gauss
Bohr radius, a_0	$=$	$0.5291772108 \times 10^{-10}$ m
Planck constant, h	$=$	$6.6260693 \times 10^{-34}$ J s
Bohr magneton, μ_B	$=$	$927.400949 \times 10^{-26}$ J T $^{-1}$
	$=$	1.4 MHz G $^{-1}$
Speed of light, c	$=$	299 792 458 m s $^{-1}$
Boltzmann constant, k_B	$=$	$1.3806505 \times 10^{-23}$ J K $^{-1}$
Permeability of free space, μ_0	$=$	$4\pi \times 10^{-7}$ m kg s $^{-2}$ A $^{-2}$
Gravitational acceleration, g	$=$	9.81 m s $^{-2}$

Table 1.4: Conversion factors and common constants used in thesis.

BEC: An Experimentalist's Guide

Bose-Einstein condensation was predicted in 1925 [14], but it took until 1995 for it to be experimentally realised in dilute gases [1, 2, 3]. It was necessary to develop many experimental techniques over the 70 years between the prediction and the experimental realisation of BEC. This section gives a brief review of these techniques. The discussion of theoretical principles is limited as they have been covered extensively in the literature and numerous theses.

2.1 The Recipe for Creating a BEC

There is no single definitive way of producing a Bose-Einstein condensate – each group have their own favourite ingredients. The different ingredients, however must be added in the correct order. Figure 2.1 illustrates the most common routes to BEC.

All experiments involve a collection stage where large numbers of cold atoms are loaded into the experimental magneto-optical trap (MOT) in the ultra-high vacuum region. The atom collection generally occurs in a magneto-optical trap (extracted from a vapour) or is generated by use of a Zeeman slower.

The workhorse of most BEC experiments is the experimental MOT (see Section 2.3) where most of the cooling in absolute terms is carried out. Following laser cooling in the MOT it is necessary to cool the atoms further by including

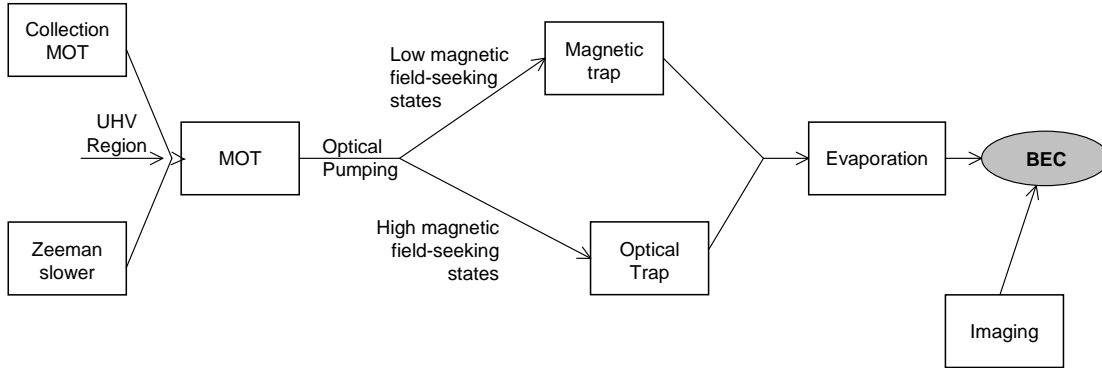


Figure 2.1: The path to Bose-Einstein condensation. (MOT – denotes magneto-optical trap.)

an optical molasses stage when the magnetic field is turned off and the cloud is allowed to expand and cool.

It is important to load a large number of atoms at a high density into the magnetic or optical trap as the evaporative cooling rate depends on the collision rate¹ on loading the trap. Many groups therefore implement variations in the MOT scheme or add additional stages to reduce the temperature or increase the density in the MOT.²

Atoms in a MOT are distributed across all magnetic sublevels, therefore prior to loading the magnetic trap, atoms must be polarized into weak field-seeking states (Section 2.4). This is accomplished with an optical pumping (OP) pulse. This not only polarizes the atoms it also pumps the atoms into fully polarized states³ which reduces the likelihood of inelastic collisions (see Chapter 3).

In 1986, Chu *et al.* [54] experimentally realised another form of an atom trap – an optical trap. The neutral atoms are trapped by the interaction of the electric dipole with far-detuned laser radiation. An excellent review article of optical dipole traps is Reference [55].

¹The elastic collision rate depends linearly on the density, therefore evaporation proceeds faster the higher the density (see Chapter 4).

²A dark spontaneous-force optical trap (DSPOT) [53] is an example of a method to increase the density in the MOT. A DSPOT confines atoms in a ‘dark’ state which reduces the force due to reradiation of atoms at the centre of the cloud (radiation pressure).

³For low field-seeking states ($m_F g_F < 0$), and high field-seeking states ($m_F g_F > 0$), fully polarized denotes states where $F = |m_F|$.

Following the confinement of the atoms, they must be cooled further in order to achieve the temperatures required for condensation (Section 2.5). If atoms with energy greater than the average energy are removed from the trap, the remaining atoms rethermalize to a lower temperature through elastic collisions. By selectively removing the hot atoms from the trap the gas is evaporatively cooled [56].

With careful optimization of all experimental parameters, a sharp peak in the density profile of the atom cloud is seen upon imaging which is the signature of the formation of a Bose-Einstein condensate.

Following the difficulty in condensing caesium, the BEC recipe had to be tailored especially for the purpose of condensing caesium in the $F = 3$, $m_F = -3$ state. Each ingredient had to be understood individually to combine these techniques effectively in order to optimize the experiment. Some of the ingredients are discussed below (Sections 2.2, 2.3, 2.4, and 2.5) whereas a discussion of the evaporative cooling considerations is given in Chapter 4.

2.2 Laser Cooling

Laser cooling of atoms was first proposed in 1975 [57], but not experimentally realised until 1985 [58]. The first neutral atom element to be cooled and trapped using laser radiation was sodium, but the other alkali metal atoms soon followed. In 1997, Steven Chu, Claude Cohen-Tannoudji, and William D. Phillips were awarded ‘The Nobel Prize in Physics’ “for development of methods to cool and trap atoms with laser light”. Laser cooling was a major discovery in the 20th century and was the last piece in the jigsaw of the quest to create a Bose-Einstein condensate.

2.2.1 Alkali Metals

There are many reasons for the popularity of alkali metals in laser cooling experiments. The main reason is that each element contains a closed cycling transition. It is also very easy to generate the required laser radiation as the ground to excited state transition frequency is in, or close to, the visible region of the electromagnetic spectrum. Another reason is that because of their low vapour pressure it is

experimentally simple to produce a vapour or atomic beam.

The alkali metals have very simple electronic configurations: closed shells and one valence electron e.g. ^{23}Na is $1s^2 2s^2 2p^6 3s^1$. Since there is only a single valence electron, the total orbital angular momentum and total spin angular momentum depend solely on this valence electron. The total angular momentum quantum number of the atom J , is given by:

$$|L - S| \leq J \leq L + S \quad (2.1)$$

For caesium, the first excited level (P) is split into two: $6P_{3/2}$ and $6P_{1/2}$. The difference in energy between the two levels is given by the spin-orbit interaction, $V_{\text{SO}} = \xi \mathbf{L} \cdot \mathbf{S}$. This interaction is the origin of the fine structure of the atom.

When the interaction of the nuclear magnetic moment, proportional to the nuclear spin \mathbf{I} , with the magnetic field, proportional to the total angular momentum of the electron \mathbf{J} , is considered, then the structure of the alkali metals becomes slightly more complicated. The total angular momentum of the atom \mathbf{F} , is given by:

$$\mathbf{F} = \mathbf{I} + \mathbf{J} \quad (2.2)$$

The magnetic-dipole hyperfine interaction $\mathbf{A} \mathbf{I} \cdot \mathbf{J}$ leads to a splitting of the different \mathbf{F} levels. This is the origin of the hyperfine structure of the atom. Each F state is split into substates labelled by m_F . In the ground state of caesium, the $F = 3$ and $F = 4$ levels are split into 7 and 9 substates respectively.⁴

In the absence of external perturbations most of these Zeeman sublevels are degenerate. The degeneracy can be lifted by applying an external field (e.g. light, magnetic). Figure 2.2 illustrates the fine structure and hyperfine structure of the caesium atom.

Many photons must be scattered in order to cool an atom, therefore it is beneficial to choose an atom that contains a closed cycling transition. The ground state hyperfine structure of the alkali metals complicates matters slightly. Off-resonant excitations occur from the excited state to the lower hyperfine state, and cause

⁴ F levels are split into $(2F + 1)$ Zeeman sublevels.

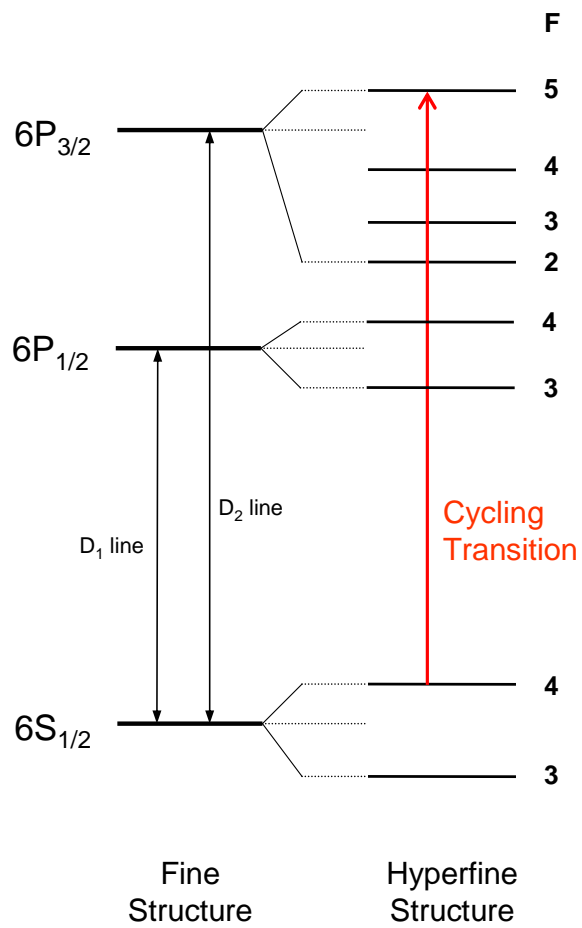


Figure 2.2: The ground configuration S and lowest lying P states of atomic Cs, showing the fine structure and the hyperfine structure (not to scale).

atoms to be lost from the cooling cycle. To return these atoms to the cooling cycle an extra laser beam at a different frequency is used.⁵

2.2.2 Doppler Cooling

Photons possess energy, $E = \hbar\omega$ and momentum, $p = \hbar k$. When an atom absorbs a photon, the atom is excited and recoils from the light source with momentum $\hbar k$. The scattering force involves a sequential process: absorption followed by spontaneous emission. As absorption is directional there is a finite mean momentum transfer, whereas the mean momentum transfer due to spontaneous emission is zero. The scattering force depends on the rate of scattering of photons and the photon momentum: $F = R\hbar k$. R is the rate of scattering of photons and is given by the following equation

$$R = \frac{\Gamma}{2} \frac{\frac{I}{I_s}}{1 + \frac{I}{I_s} + \left(\frac{2(\Delta + \omega_D)}{\Gamma}\right)^2} \quad (2.3)$$

Γ is the linewidth of the excited state, and Δ is the detuning of the laser radiation from resonance ($\Delta = \omega_L - \omega_0$). ω_D is the Doppler shift seen by the moving atoms and is given by $\omega_D = -\mathbf{k} \cdot \mathbf{v}$. I/I_s is the ratio of the light intensity (I) to the saturation intensity (I_s) given by:

$$\frac{I}{I_s} = \frac{2 \Omega^2}{\Gamma^2}$$

where Ω is the Rabi frequency.

If the atoms are illuminated with two counter-propagating low intensity laser beams of the same frequency, intensity and polarization, atoms moving along the light beams will experience a net force proportional to their velocity. If the laser radiation is detuned below atomic resonance (red-detuned) $\Delta < 0$, the frequency of the light of the beam opposing the atom's motion is Doppler shifted towards the blue in the atomic rest frame and is therefore closer to resonance. The atoms

⁵The cycling transition in caesium is $F = 4 \rightarrow F' = 5$. However, approximately 1 in 2000 excitations is an off-resonant transition to $F' = 4$, from which decay to $F = 3$ can occur. An additional laser (repumping laser) tuned to $F = 3 \rightarrow F' = 4$ transition (from which decay to $F = 4$ can occur) is required to return the atoms to the cooling cycle.

therefore absorb photons preferentially from the beam that opposes their motion. Hence the atoms experience a viscous force opposing their motion. This principle can be extended to three dimensions using three pairs of counter-propagating light beams in orthogonal directions (optical molasses).

As the atoms are cooled their Doppler frequency changes, and once the velocity change is large enough the laser radiation is no longer in resonance with the atoms, and so the cooling stops. Two methods of compensating for the changing Doppler shift as the atoms decelerate are: changing the laser frequency ω_L [59, 60, 61], or spatially varying the atomic resonance frequency using a magnetic field [62, 63].⁶

However, there is a limit to the temperatures that can be reached using Doppler cooling because of the associated heating. Even though the average momentum from spontaneous emission is zero, the root-mean-square (rms) value of the momentum is non-zero. This leads to Brownian motion-like behaviour by the atoms. The Doppler limit [64] is given by $T_D = \frac{h\Gamma}{2k_B}$. For caesium the Doppler temperature is $125 \mu\text{K}$.

2.2.3 Sub-Doppler Cooling

When considering Doppler cooling the internal structure of the atoms is ignored. However, due to the hyperfine structure and the Zeeman sublevels, alkali metals can be cooled to temperatures much lower than the Doppler limit. Sub-Doppler cooling depends on multiple (normally degenerate) ground states, “light shifts” of ground states, optical pumping among ground states and polarization gradients in the light field. The sub-Doppler viscous force is much greater than the Doppler viscous force. However, the sub-Doppler capture range is small and therefore atoms must be initially Doppler cooled before the effects of sub-Doppler cooling are observed.

When a laser beam is incident on an atom, the energy levels are perturbed by the light. Light shifts cause a splitting in energy of the ground state. For $J = 1/2$, the ground state is split into two levels $m_J = +1/2$ and $m_J = -1/2$.

⁶This technique is employed effectively in Zeeman slowers.

However, because of the standing wave formed by two counter-propagating beams the energy levels periodically vary across the wavelength of the standing wave (see Figure 2.3).

In Doppler cooling the polarization of the laser radiation is ignored. However the orientation of the dipole moment of the atoms with respect to the polarization of the light is important. Different states in multilevel atoms are coupled differently to the light field depending on the polarization. σ^+ polarization drives $\Delta m_F = +1$ transitions and σ^- polarization drives $\Delta m_F = -1$ transitions.

Two important polarization cases in laser cooling are the linear \perp linear configuration and the $\sigma^+ - \sigma^-$ configuration. Both lead to temperatures below the Doppler limit, however the mechanisms for reaching these temperatures are different. A full discussion of sub-Doppler cooling is given in Reference [65].

Linear \perp Linear Polarization Gradient Cooling

Two linearly polarized counter-propagating laser beams of the same frequency interfere and create a strong polarization gradient. The polarization changes from linear to σ^+ in $\lambda/4$ (see Figure 2.3). If an atom absorbs a photon and is excited then two outcomes are possible: the atom decays to the original level, or it decays to a different magnetic sublevel. For the former case the atom receives a random momentum kick but its energy does not change. For the latter case however, the spontaneously emitted photon is of a higher frequency than the one that was absorbed (Figure 2.3). This means that the atom loses energy, leading to a reduction in its velocity. By careful selection of the laser radiation detuning it is possible to make it more probable for an atom to absorb a photon at the top of the ‘hill’ than at the ‘bottom’. This leads to a reduction in the energy of the atoms i.e. cooling. Figure 2.3 illustrates the principles of linear \perp linear polarization gradient cooling.⁷

⁷Linear \perp linear polarization gradient cooling is also called Sisyphus cooling after the Greek mythological character, Sisyphus. He was doomed by the Greek gods to forever roll a large boulder to the top of a hill.

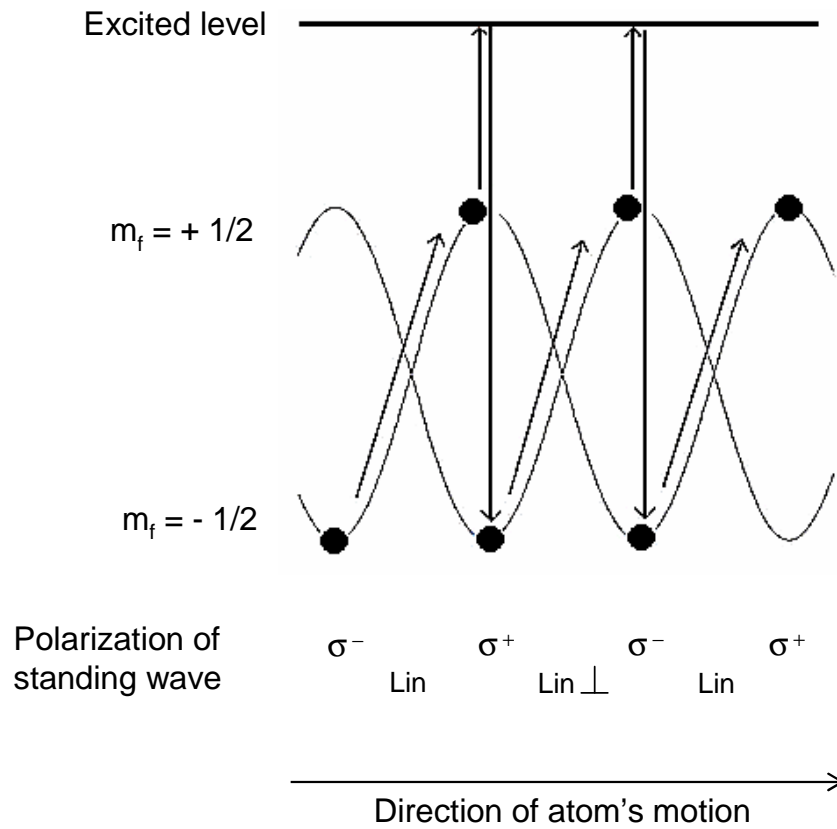


Figure 2.3: A diagram (not to scale) illustrating the principles of Sisyphus cooling. As the atoms climb the potential hill their kinetic energy is reduced. When they reach the node they are optically pumped to the antinode. The atoms are continually losing kinetic energy and therefore their velocity will gradually be reduced.

$\sigma^+ - \sigma^-$ **Polarization Gradient Cooling**

Two counter-propagating oppositely circularly polarized light beams create a light field where the polarization is linear but rotates in direction about the beam's axis. When the atoms travel along the axis of the beams the light shifts of the ground state sublevels remain constant and therefore Sisyphus cooling does not occur in this case.

For a stationary atom the population distribution is symmetric across the magnetic sublevels and therefore the atom absorbs photons from both beams equally, giving no net force on the atom. However, when the atoms are moving through a polarization gradient, there is a difference in the scattering rate between the two counter-propagating beams.⁸ Because the transition rate between different pairs of magnetic sublevels of excited and ground states (Clebsch-Gordon coefficients) depends on the orientation of the electron spin and the polarization of the laser radiation driving the transition, an atom will preferentially absorb photons from the laser beam which is opposing its motion if the laser radiation is red-detuned. The distribution across the magnetic substates is no longer symmetric and therefore there is an imbalance in the absorption rate of photons from the two beams, giving a force that opposes the atom's motion.

Even though the sub-Doppler viscous force is much larger than the Doppler viscous force, the temperature is still limited by heating caused by spontaneous emission and fluctuations in the number of absorbed photons. Temperatures that are a few times the recoil limit can be attained. The recoil temperature is given by $T_r = \frac{(\hbar k)^2}{mk_B}$. For caesium the recoil temperature is $T_r = 197$ nK.

Neither Doppler or sub-Doppler cooling contain a dependence on position, therefore the atoms are not localized in space. The internal structure of atoms can be used not only to cool them effectively, but also to confine them. In order to trap atoms, magneto-optical traps were developed.

⁸Motion-induced orientation leads to an imbalance in the scattering from the two counter-propagating beams.

2.3 Magneto-Optical Traps

Most of the cooling in BEC experiments (in absolute terms) is performed in magneto-optical traps (MOTs). Using light and magnetic fields it is possible to confine a large number of atoms and cool them to temperatures less than $1 \mu\text{K}$. The first experimental demonstration of a MOT was in 1987 [66] and since then there has been extensive treatment of MOTs in the literature [67, 68, 69, 70]. There are many possible MOT orientations including the 4-beam MOT [71], the pyramidal MOT [72], and the surface MOT [73].

A magnetic field is required in order to localize the atoms in space and it is normally generated by a pair of anti-Helmholtz coils. The ground state and the excited magnetic states are shifted in energy by the Zeeman effect. The excited state has three Zeeman components (for a $F = 1$ state) and the transition frequency of these states tune with magnetic field and therefore position. The atoms are illuminated by two red-detuned ($\Delta < 0$) counter-propagating beams of opposite circular polarization. The imbalance in the forces of the two beams leads to a resultant force on the atoms. A schematic of the principles of a MOT is given in Figure 2.4.

2.3.1 Six-Beam MOT

Figure 2.4 illustrated the principles of a MOT in one dimension. To extend the principle to three dimensions two further pairs of counter-propagating beams of opposite circular polarization are added in orthogonal directions to the original beams as illustrated in Figure 2.5.

The polarization configuration in a MOT implies that only $\sigma^+ - \sigma^-$ polarization gradient cooling occurs. This would be true if the atoms only moved along the axis of the beams. However, atoms move in random directions and therefore at intermediate points between the axes the polarization is not well defined and therefore both types of sub-Doppler cooling occur.

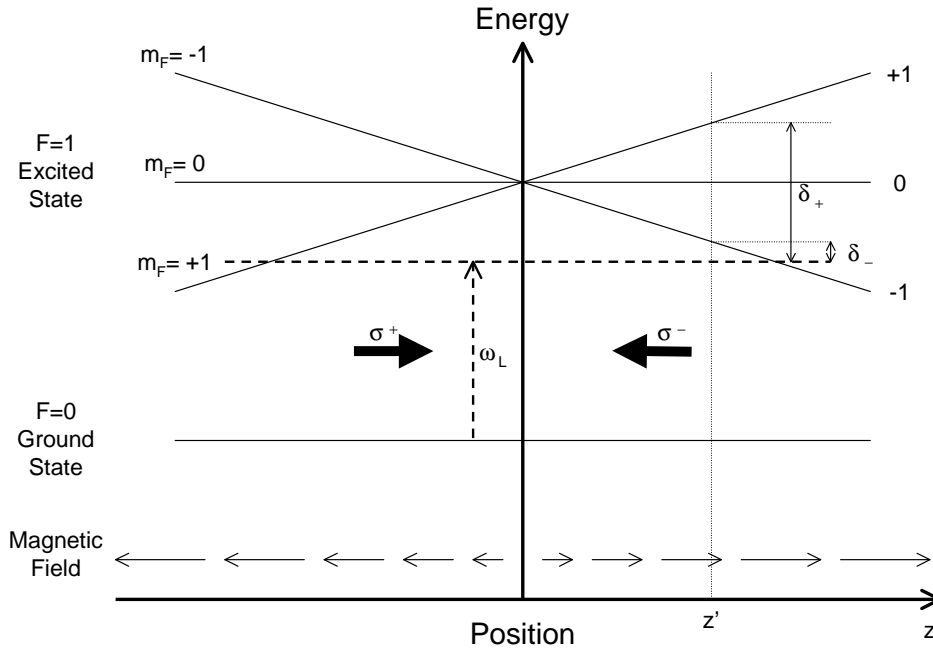


Figure 2.4: Arrangement for a MOT in one-dimension (1D). At point $z = z'$ the atoms are closer to resonance with the σ^- beam. Therefore the atom is driven towards the centre of the trap. Even though the scheme is described for $F = 0 \rightarrow F' = 1$ transition, it works well for any $F \rightarrow F' = F + 1$ transition. (σ^+ and σ^- denote transitions and should be defined with respect to the direction of the magnetic field. However, in this case they are used to denote beams and are defined with respect to the z -axis.)

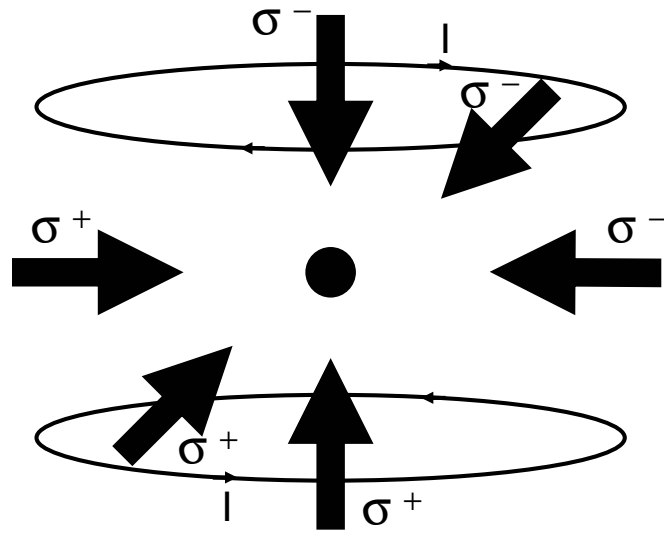


Figure 2.5: Direction and polarization configuration of a six beam MOT.

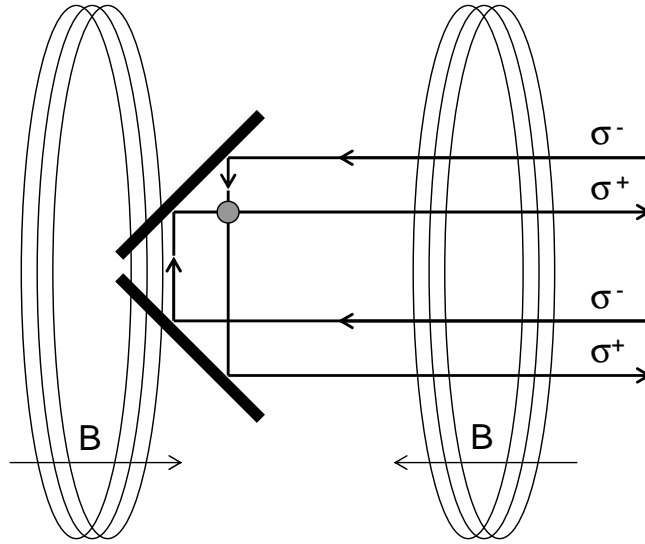


Figure 2.6: Cross-section of the pyramidal MOT and the resulting polarization configuration.

2.3.2 Pyramidal MOT

The pyramidal MOT is a way of generating the same radiation field as in a six-beam MOT. A pyramidal MOT only requires one input beam to produce the same configuration of light polarizations as a standard six-beam MOT. The original pyramidal MOT consisted of a large beam of σ^- polarized light incident on a conical hollow mirror [72]. This was then modified to include a small hole at the vertex in order to not only confine atoms but enable transfer of atoms into the experimental MOT [74]. The first reflection on the mirror produces a pair of counter-propagating beams with opposite polarization. The second reflection then produces a σ^+ retro-reflected beam. This occurs in all three dimensions creating the required polarization configuration. Figure 2.6 illustrates the setup of a pyramidal MOT.

2.4 Magnetic Trapping

Ions were first trapped and cooled in 1959 [75], but it took until 1985 to trap neutral atoms [76]. Ions, which are trapped by the strong Coulomb interaction, can be trapped from a background gas with no prior cooling. However, atoms need to be cooled before loading them into a magnetic trap because of the shallow depth of magnetic traps. Therefore the magnetic trapping of neutral atoms had to wait until laser-cooling had been developed.

Neutral atoms are confined by the interaction of an inhomogeneous electromagnetic field with the atomic dipole moment. The interaction between the magnetic moment and the magnetic field produces a force given by the following equation:

$$\mathbf{F} = \nabla(\boldsymbol{\mu} \cdot \mathbf{B}) \quad (2.4)$$

The potential energy of an atom with a magnetic moment is given by (in the limit of a weak field):

$$U = -\boldsymbol{\mu} \cdot \mathbf{B} = m_F g_F \mu_B B \quad (2.5)$$

Earnshaw's theorem states that local field maxima are not allowed.⁹ Therefore in order to be able to trap neutral atoms, as the magnetic field increases the energy of the atom must also increase. Atoms must therefore be in a low-field seeking state i.e. $m_F g_F > 0$.

2.4.1 Zeeman Effect on the Hyperfine Ground States

The Zeeman energy of the two ground hyperfine states in the presence of a magnetic field can be expressed by the Breit-Rabi equation [78]. The equation is given below (Equation 2.6) and plotted for caesium in Figure 2.7.

$$\text{Energy (J)} = -\frac{h\nu_{\text{HFS}}}{2(2I+1)} - g_I \mu_B m_F \pm \frac{1}{2} h\nu_{\text{HFS}} \times \left\{ 1 + \frac{4m_F}{2I+1} x + x^2 \right\}^{1/2} \quad (2.6)$$

⁹Earnshaw's theorem states: *In a region devoid of charges and currents, the strength of a quasistatic electric or magnetic field can have local minima but not local maxima* [77].

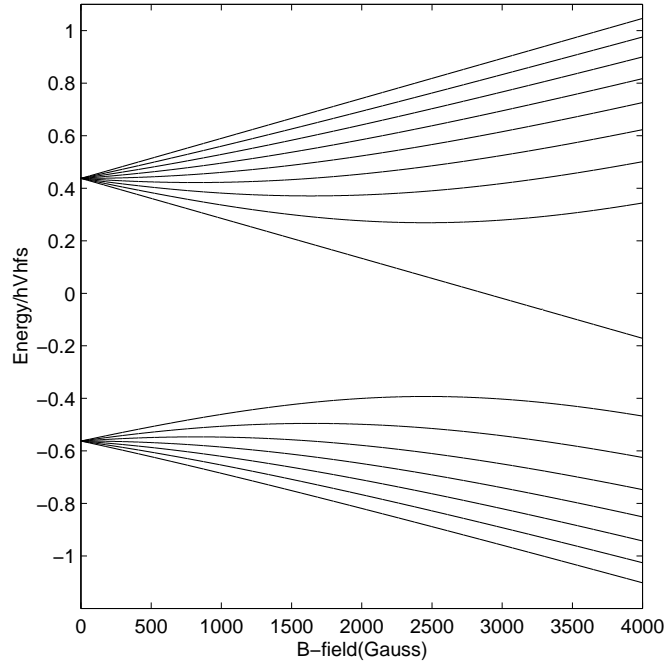


Figure 2.7: Zeeman effect of the hyperfine ground state for ^{133}Cs .

where

$$x = \frac{(g_J + g_I)\mu_B B}{h\nu_{\text{HFS}}}$$

The values for caesium of the gyromagnetic factors (g_J and g_I), the hyperfine splitting (ν_{HFS}) and the nuclear spin (I) are given in Table 2.1.

Name	Symbol	Value
Ground State Hyperfine Splitting	ν_{HFS}	9.192631770×10^9 GHz
Nuclear Spin	I	$7/2$
Nuclear Gyromagnetic Ratio	g_I	0.00039885395
Electron Gyromagnetic Ratio	g_J	2.0023193043737
Planck's Constant	h	6.626069×10^{-34} J s
Bohr magneton	μ_B	9.274009×10^{-28} J G $^{-1}$

Table 2.1: Caesium-133 atomic structure constants required for the calculation of the Breit-Rabi equation.

2.4.2 Simple Magnetic Trap

The simplest magnetic trap was originally proposed by W. Paul and was experimentally realized in 1985 [76]. It consists of two coils in an anti-Helmholtz ar-

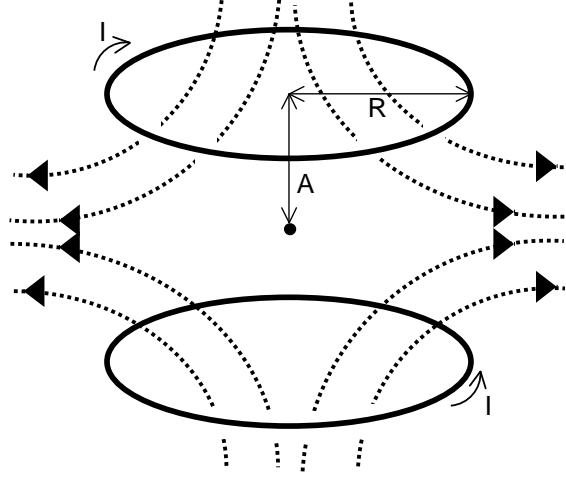


Figure 2.8: Diagram of a simple magnetic trap. The dotted lines (\cdots) are the magnetic field lines. The distance $2A$ is the separation between the two coils. The black circle illustrates the position of the minimum of the magnetic field which is zero in this case as the current in the coils is equal and opposite.

rangement. The magnetic field due to a circular coil at a point on its axis is given by Equation 2.7.

$$B_z = \frac{\mu_0}{2} \frac{nIR^2}{((A-z)^2 + R^2)^{\frac{3}{2}}} \quad (2.7)$$

where n is the number of turns, I is the magnitude of the current flowing through the coil, R is the radius of coil and A is the distance along the axis of the coil from the centre (see Figure 2.8). The field gradient for a pair of coils in anti-Helmholtz arrangement with radius R and separation $2A$ is:

$$\left. \frac{\partial B}{\partial z} \right|_{z=0} = \frac{3nIR^2 A \mu_0}{(A^2 + R^2)^{\frac{5}{2}}} \quad (2.8)$$

An inherent problem in this trap is the occurrence of a zero in the magnetic field at the trap centre. This causes Majorana transitions (colloquially called “spin flips”) when the atoms change their m_F state leading to loss from the trap.

2.4.3 Majorana Transitions

In the presence of a magnetic field the atoms’ magnetic moment precess about the field at the Larmor frequency: $\omega_{\text{Larmor}} = m_F g_F \mu_B B$.¹⁰ In order to remain

¹⁰In the current experiment the magnetic field is rarely below 130 G and therefore the Larmor frequency is always greater than 136 MHz.

trapped the atoms' magnetic moment must follow the field adiabatically otherwise the atoms undergo Majorana transitions [79] into un-trapped or anti-trapped states ($m_F g_F < 0$). The rate of change of the field direction θ must be slower than the precession of the magnetic moment:

$$\frac{d\theta}{dt} < \frac{\mu_B |\mathbf{B}|}{\hbar} = \omega_{\text{Larmor}}$$

As long as $d\theta/dt$ is smaller than the trapping frequencies then there is negligible probability of an atom undergoing a Majorana transition.

This problem prevented the early experiments from reaching BEC. This led to the development of a new generation of magnetic traps which avoided this problem e.g. the TOP (time-averaged orbiting potential) trap [80] and the PLUG trap [2]. Another solution, is to use a Ioffe-Pritchard trap.

2.4.4 Ioffe-Pritchard Trap

A Ioffe-Pritchard (I-P) trap is formed by a linear quadrupole field and an axial field. The linear quadrupole field is produced by 4 straight wires (Ioffe bars) parallel to the z -axis (Figure 2.9 (a)), each carrying equal magnitude of current but the direction of the current in each wire is opposite to its nearest neighbour (Figure 2.9 (b)). The magnetic field along the z -axis is therefore zero. The axial field is provided by two end coils ("pinch" coils) with current flowing in the same direction and with equal magnitude in both coils. This is illustrated in Figure 2.9 (a). The "pinch" coils therefore add an axial magnetic field to the magnetic field produced by the Ioffe bars. This means that the field along the z -axis is no longer zero and therefore there is negligible probability of an atom undergoing Majorana transitions.

To calculate the magnetic field near the centre of the trap, consider four straight wires, infinitely long and narrow, positioned perpendicular to the x - y plane and in the positions and with current I_r flowing as indicated in Figure 2.9 (b). The field produced by these wires provides radial confinement but has no component in the z direction. The axial coils are n turn coils of radius R with current I_a flowing.

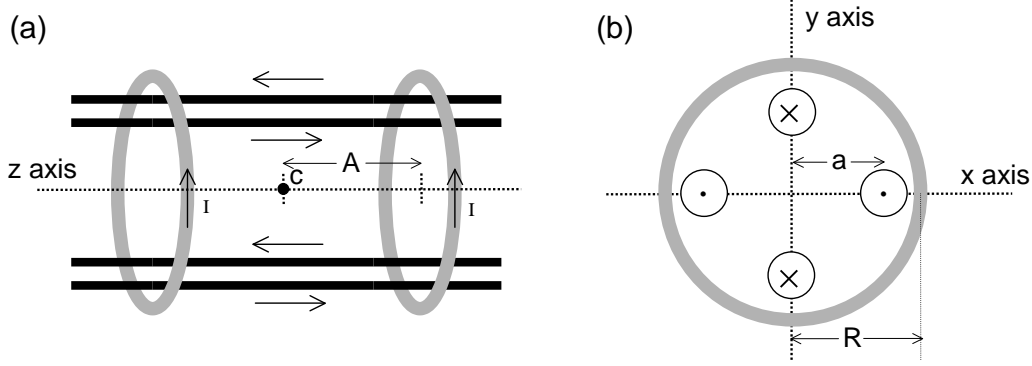


Figure 2.9: A schematic of a Ioffe-Pritchard trap: (a) illustrates the physical arrangement of the bars and coils and the directions of the currents. Point c is the centre of the magnetic trap where $x = y = z = 0$, (b) illustrates the current direction in the Ioffe bars.

The magnetic field produced by these two coils has no x or y component and as long as the coils are separated by a distance greater than their radius they provide axial confinement.

Combining the expressions for both the Ioffe bars and the “pinch” coils yields the following expression:

$$\mathbf{B} = \begin{pmatrix} \frac{\mu_0 I_r}{2\pi} \left\{ \frac{-y}{(x-a)^2+y^2} + \frac{y-a}{(y-a)^2+x^2} + \frac{-y}{(x+a)^2+y^2} + \frac{y+a}{(y+a)^2+x^2} \right\} \hat{x} \\ \frac{\mu_0 I_r}{2\pi} \left\{ \frac{x-a}{(x-a)^2+y^2} + \frac{-x}{(y-a)^2+x^2} + \frac{x+a}{(x+a)^2+y^2} + \frac{-x}{(y+a)^2+x^2} \right\} \hat{y} \\ \frac{\mu_0 n R^2 I_a}{2} \left\{ \frac{1}{((A+z)^2+R^2)^{\frac{3}{2}}} + \frac{1}{((A-z)^2+R^2)^{\frac{3}{2}}} \right\} \hat{z} \end{pmatrix} \quad (2.9)$$

The magnitude of the magnetic field can be determined by expanding Equation 2.9 around the origin ($x = y = z = 0$), keeping only the leading terms in the expansion[81, 82].

$$B \cong B_0 + \frac{4\mu_0 I_r^2}{\pi^2 a^4 B_0} r^2 + \frac{3B_0(4A^2 - R^2)}{2(A^2 + R^2)^2} z^2, \quad B_0 = \frac{\mu_0 n R^2 I_a}{(A^2 + R^2)^{\frac{3}{2}}} \quad (2.10)$$

where $r^2 = x^2 + y^2$.

If μ is the magnetic moment of the atom then the energy of the atom in the magnetic field can be written:

$$E = \mu B \quad (2.11)$$

Substituting Equation 2.10 into the Equation 2.11 yields the following equation:

$$\begin{aligned} E = \mu B &= \mu B_0 + \frac{4\mu_0 I_r^2 \mu}{\pi^2 a^4 B_0} r^2 + \frac{3B_0(4A^2 - R^2)\mu}{2(A^2 + R^2)^2} z^2 \\ &= E_0 + \frac{m}{2}(\omega_r^2 r^2 + \omega_z^2 z^2) \end{aligned} \quad (2.12)$$

Equating corresponding terms yields expressions for the trap frequencies of a Ioffe-Pritchard trap as stated in Equation 2.13:

$$\omega_r = \left(\frac{\mu_0 8\mu_0}{m\pi^2}\right)^{\frac{1}{2}} \frac{I_r}{a^2 \sqrt{B_0}} \quad \text{and} \quad \omega_z = \left(\frac{3\mu_0 R^2 \mu_0 (4A^2 - R^2)}{m(A^2 + R^2)^{\frac{7}{2}}}\right)^{\frac{1}{2}} \sqrt{I_a} \quad (2.13)$$

The radial trap frequency is proportional to the current in the Ioffe bars and inversely proportional to the square root of the bias magnetic field at the centre of the trap. The axial frequency is directly proportional to the square root of the current running through the coils.

There are many adaptations of the I-P trap, the most notable being the cloverleaf trap developed at MIT [83] and the baseball trap developed at JILA [81].

2.4.5 Baseball Trap

A very convenient way to make an I-P trap is to bend the ends of the parallel wires (Figure 2.9) into one coil. This creates a coil shaped like the seams on a baseball (Figure 2.10). The ease of use of this trap arises from the fact that the four parallel wires and ‘‘pinch’’ coils are now one ‘coil’. Therefore, applying a current to this single coil effectively produces the same effect as equal current flowing through the four parallel wires and the ‘‘pinch’’ coils. For the baseball coil, only one current needs to be regulated, and therefore the need for complicated electronics is reduced.

The expression for the magnetic field for the Ioffe-Pritchard trap derived previously (Equation 2.9), is no longer accurate for the baseball trap. The expression was calculated for four infinitely long and narrow wires and a pair of Helmholtz coils, whereas the baseball coil is a single coil that provides both radial and axial confinement. However, the magnetic field produced by the baseball coil is qualitatively similar to that in Equation 2.9.

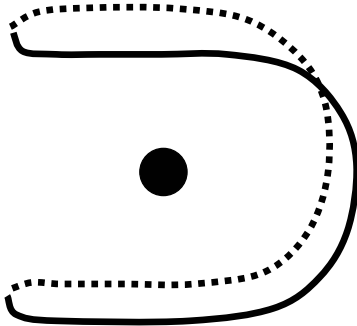


Figure 2.10: Schematic of a baseball coil. The black circle illustrates the position of the minimum of the magnetic field.

Equation 2.9 becomes more inaccurate when gravity pulls the atoms down from the centre of the trap. The expansion about the trap centre is no longer valid as the atoms no longer sit at the centre of the coils. For a purely harmonic potential, the amount of sag can be calculated by equating the force due to the potential to the force due to gravity:

$$m\omega_z^2 z = mg \quad (2.14)$$

$$\Rightarrow z = \frac{g}{\omega_z^2} \quad (2.15)$$

For caesium atoms in a 12 Hz trap the magnitude of the sag is 1.7 mm.

For atoms in a baseball trap, a minimum in the energy of the atoms (magnetic and gravitational) still exists. Therefore, expanding the potential about the new sagged trap centre yields leading terms that are quadratic. The smaller the spatial size of the cloud the less important the anharmonic terms in the expansion are, therefore the potentials can still be approximated as harmonic.

2.4.6 Experimental Considerations

Atoms cannot be loaded directly into a magnetic trap from room temperature because of the small depth of the trap. This puts a constraint on the temperature of the atoms to be loaded. Atoms are normally loaded into a magnetic trap from a MOT or from optical molasses (temperatures in the μK range).

The shallow depth of neutral atom traps also puts constraints on the vacuum re-

quirements. A collision between a trapped atom and a thermal energy background gas atom leads to the loss of the trapped atom from the magnetic trap. Therefore, in order to produce condensates, low pressures must be attained and sustained in the experimental cell. At low pressure, the trapping time is $\approx 10^{-8}/P$ s where P is the pressure in Torr [84].

2.5 Evaporative Cooling

Evaporative cooling was originally proposed by Hess in 1986 [85]. Experimental demonstration soon followed in 1988 [86]. These evaporation experiments were carried out on atomic hydrogen which had already been pre-cooled by cryogenic methods. It was not until 1994 that the technique of evaporative cooling was extended to alkali metals by combining laser cooling and radio-frequency (rf) evaporative cooling [87, 88]. These experiments increased the PSD by six orders of magnitude while only losing approximately a factor of a thousand atoms [1, 3]. Evaporative cooling is a highly efficient process as long as the rethermalization time is significantly shorter than the lifetime of the atom cloud (see Chapter 4).

There are a number of ways of selectively removing hot atoms from the trap: passing over a potential energy barrier [89], adsorption onto a pumping surface [90] or by optical [91] or rf [92] pumping the atoms to non-trapped states. The most common method in alkali metal experiments is radio-frequency (rf) evaporation.

2.5.1 Radio-Frequency Evaporation

Hot atoms have large orbits in the magnetic trap and therefore they span a large range of magnetic field values. To address only the hot atoms a narrow magnetic field or energy-sensitive transition is required, for example rf transitions between adjacent Zeeman sublevels. By selecting the rf frequency carefully (and other experimental parameters) the atoms can be induced to undergo an adiabatic transition from the trapped state directly to the anti-trapped state. The atoms are thus expelled from the trap.

Rf evaporation has many advantages over other methods of evaporation. The

magnetic trap potential depth does not need to be lowered, and the evaporation can be three-dimensional in velocity space as the atoms are evaporated from any surface where the resonance condition is fulfilled. The rf surface removes all the atoms whose energy is greater than the energy of the cloud by a fixed ratio η and therefore the rf surface removes all atoms whose energy is greater than the truncation energy given by $\epsilon_t = \eta k_B T$. The larger the truncation energy the more efficient the evaporation.¹¹ The evaporation is however slower and therefore the chosen experimental value of η is a balance between more efficient cooling and the speed at which the cooling occurs.

At low-fields, the Breit-Rabi equation (Equation 2.6) simplifies to $E = g_F m_F \mu_B B$. The rf transitions between adjacent Zeeman sublevels ($|\Delta m_F|=1$) are therefore degenerate leading to multiphoton transition from a magnetically trapped state to an un-trapped or anti-trapped state. However at high magnetic fields the degeneracy is lifted. This is an important fact to consider for any experiment evaporating at high magnetic fields. For ^{133}Cs ($3, -3$) state at 500 G, the difference in the frequency of the rf transitions between $m_F = -3 \leftrightarrow -2$ and $m_F = -2 \leftrightarrow -1$ transitions is of the order of 8 MHz and this can lead to a decrease in the efficiency of evaporation [93].

2.5.2 Effects of Gravity on Evaporation

To support the atoms against gravity a magnetic field gradient is required. The force in the z -direction due to the trap is equated to the force on the atoms due to gravity.

$$F_z = g_F m_F \mu_B \frac{\partial B}{\partial z} = mg \quad (2.16)$$

The minimum gradient for the ^{133}Cs $F = 3$, m_F states 3, 2, and 1 is 31.3, 47.0 and 94.0 G cm⁻¹ respectively. Under normal conditions all three magnetically trappable states are supported in the magnetic trap. However, the presence of many states in the magnetic trap increases the probability of inelastic collisions leading to losses from the trap. To reduce the presence in the magnetic trap of all states except

¹¹This is only true in the absence of any loss or heating in the atom cloud.

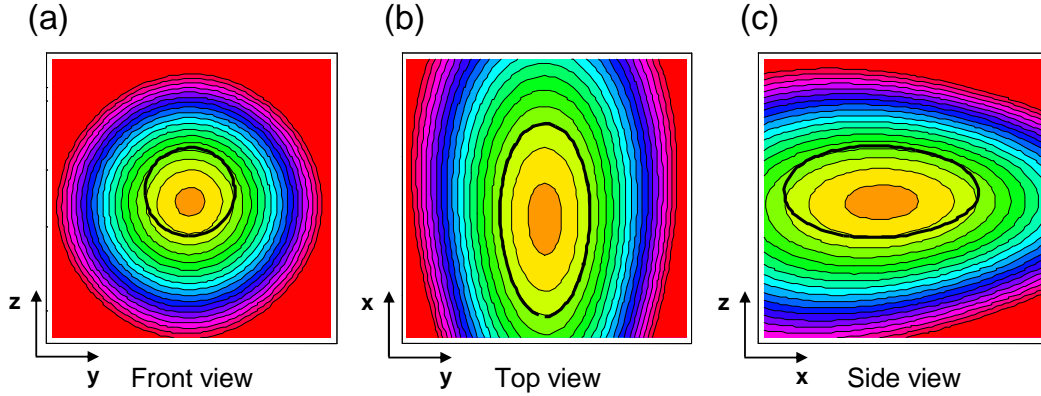


Figure 2.11: The effect of gravity on the magnetic potential. The coloured contour lines are the potential that the atoms experience (including gravity). The black ellipse is the rf evaporation surface. This clearly shows that gravity does indeed make the evaporation one-dimensional.

$F = 3$, $m_F = -3$, the atoms can either be optically pumped into the $(3, -3)$ state or the magnetic trap gradient reduced so that other m_F states are no longer supported against gravity. Also, after loading it is possible to expel the $(3, -2)$ and $(3, -1)$ atoms from trap using a radio-frequency cutting surface.

How does gravity affect the simple picture?

In a zero gravity environment, the cloud of atoms sits perfectly centred on the B-field contours. The evaporation surface determined by the rf frequency then touches the extremity of the cloud in all directions, resulting in efficient 3D evaporation. In reality, gravity pulls the cloud downwards leading to an offset in the centre of the cloud from the centre of the magnetic trap. As calculated previously, for weak traps with vertical trapping frequencies of the order of 10 Hz, the sag is over 2 mm (Equation 2.15). The bottom of the cloud experiences a higher magnetic field than the top. Consequently the evaporation surface is only in contact with one side of the cloud, leading to one dimensional evaporation. This is illustrated in Figure 2.11.

There is one benefit of 1D evaporation. Gravity puts the atoms into a region where the rf contours vary much more quickly across the cloud. This enables precise cutting – a cutting surface which is shallower and less susceptible to stray

magnetic fields.

2.5.3 Dimensionality of Evaporation

When evaporation is three-dimensional all the atoms with energy greater than $\eta k_B T$ are removed from the trap. Evaporation is one-dimensional when $E_z > \eta k_B T$ and two-dimensional when $E_x + E_y > \eta k_B T$. These criterion only apply when the magnetic trapping potential is separable. If the rate of mixing between potentials is faster than the rate of elastic collisions then the evaporation is always three-dimensional.

Evaporation in lower dimensions leads to a reduction in the efficiency [94] because atoms with an energy higher than the truncation energy may undergo many collisions before leaving the magnetic trapping potential. In the absence of inelastic collisions, the dimensionality of the evaporation surface does not affect the efficiency of the evaporation, it only leads to longer evaporation times. However, in the presence of inelastic collisions a time limit is set on the evaporation process and therefore dimensionality of the evaporation process has a dramatic effect on the efficiency.

In a magnetic trapping potential the frequency of the rf is given by:

$$\hbar\omega_{rf} = \Delta m_F g_F \mu_B B \quad (2.17)$$

$$= g_F \mu_B B \quad (\text{as } \Delta m_F = 1) \quad (2.18)$$

If the atom cloud sits perfectly centred on the magnetic trapping contours then $|B|=\text{constant}$ contours are equipotential surfaces and therefore the rf surface drives transitions into un-trapped and anti-trapped states at positions of equal $\eta k_B T$ in all three dimensions.

When the truncation energy is set as $\eta k_B T$ the average energy of the atoms removed is not necessarily ϵ_t . To account for the slight difference an extra factor κ is introduced. Therefore, the average energy of atoms removed from the trapping potential is:

$$\epsilon = (\eta + \kappa) k_B T \quad (2.19)$$

The value of κ is normally between 0 and 2 and can be neglected for large values of η . Evaporated atoms have an average excess energy of $\kappa k_B T$. If the gravitational energy across the equipotential surface $U = \eta k_B T$ varies by $\pm k_B T$ then evaporation only occurs at the bottom of the cloud.

For harmonic confinement along the z -axis:

$$U = \frac{U'' z^2}{2} \quad (2.20)$$

The equipotential surface therefore exists at:

$$z \approx \sqrt{\frac{2\eta k_B T}{U''}} \quad (2.21)$$

Evaporative cooling becomes one-dimensional when:

$$k_B T < \frac{2\eta(mg)^2}{U''} \quad (2.22)$$

$$< \frac{2\eta m g^2}{\omega_z^2} \quad (2.23)$$

For caesium atoms in a 10 Hz trap the evaporation becomes one-dimensional (for $\eta = 6$) when the temperature falls below approximately 5 mK. The temperature achieved in optical molasses is of the order of tens of μK and therefore in weak magnetic traps the evaporation is always one-dimensional. The dimensionality of the evaporation can be increased by operating in tighter magnetic traps.¹²

¹²Gravitational sag still exists in tighter traps but the difference in energy across the cloud is less than $k_B T$.

Scattering Theory and Feshbach Resonances

Inter-atomic collisions are crucial for evaporative cooling: atom clouds rethermalize through elastic collisions; trap heating and loss occur due to inelastic collisions. Evaporation performance depends on the ratio between elastic and inelastic collisions (Chapter 4) and therefore understanding inter-atomic collisions and their dependence on external parameters can mean the difference between succeeding and failing to create a BEC.

3.1 Atomic Interactions

The interactions between the two colliding atoms can have significant effect even when the atoms are far apart (compared to the radii of the electronic charge clouds). We can write the Hamiltonian for two interacting atoms as:

$$H(r, s) = H_0(r) + H_{12}(r, s) \quad (3.1)$$

where $H_0(r)$ and $H_{12}(r, s)$ are the unperturbed and interaction Hamiltonian respectively. The inter-atomic separation between the two colliding atoms is denoted by \mathbf{r} ($= \mathbf{R}_1 - \mathbf{R}_2$) and their spin by \mathbf{s} .

The unperturbed Hamiltonian describes non-interacting atoms in a magnetic trapping potential. Equation 3.1 is valid when the atoms can be treated individually and the interactions as a perturbation. The interaction Hamiltonian is given

by:

$$H_{12}(r, s) = H_v(r) + H_{ex}(r, s) + H_d(r, s) \quad (3.2)$$

where $H_v(r)$, $H_{ex}(r, s)$ and $H_d(r, s)$ are the Hamiltonians representing the van der Waals, exchange term and dipolar interactions respectively.

For the previous equations (Equations 3.1 and 3.2) the terms in brackets following each individual Hamiltonian give the dependence of the corresponding interaction on r and s . If the interaction depends on r , then changes in the external degrees of freedom can occur. Equivalently, if the interaction depends on the spin, then changes in the internal state of the colliding atoms can occur.¹

3.1.1 Unperturbed Hamiltonian

The unperturbed Hamiltonian H_0 , of two colliding atoms is the Hamiltonian of two separate non-interacting atoms in a magnetic field. Equation 3.3 states the terms that are included in the unperturbed Hamiltonian.

$$H_0(r) = -\frac{\hbar^2}{2\mu}\nabla^2 + H_h + H_Z \quad (3.3)$$

The first term is associated with the kinetic energy ($\mu = m/2$ where m is the reduced mass), and H_h and H_Z are the Hamiltonians for the hyperfine interaction and the Zeeman interaction respectively.

3.1.2 van der Waals Interaction and Exchange Terms

The two main interactions for two colliding neutral atoms are the van der Waals interaction and exchange interaction.

The van der Waals interaction $H_v(r)$, arises from the induced electric dipoles and quadrupoles of the neutral atoms² and can be written in the form:

$$H_v(r) = -C_6r^{-6} - C_8r^{-8} - C_{10}r^{-10} + \dots \quad (3.4)$$

¹A change in the internal states of the colliding atoms is synonymous to a change of channel occurring during a collision. Prior to colliding the atoms are in the entrance channel, following the collision they are in the exit channel. If the entrance and exit channels are the same/different then an elastic/inelastic collision has occurred.

²All permanent electric dipoles and multipoles are absent in a ground state neutral atom.

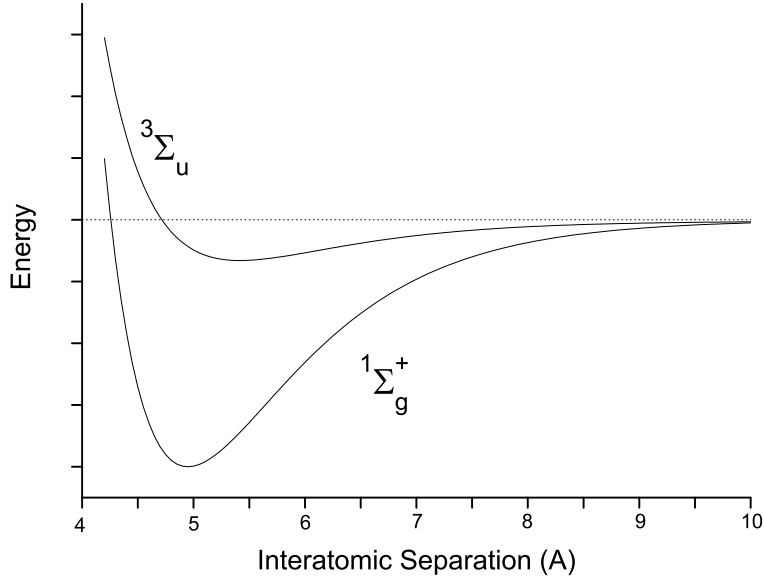


Figure 3.1: Schematic of the interaction potentials as functions of the inter-atomic separation for two ground state caesium atoms with electrons in singlet $X^1\Sigma_g^+$ and triplet $a^3\Sigma_u$ states. The exchange interaction causes a splitting in energy depending on whether the spins of the colliding atoms are parallel ($S = 1$ or triplet) or anti-parallel ($S = 0$ or singlet).

At large inter-atomic separation the van der Waals interaction is due to the induced dipole-dipole interaction between the atoms which is caused by their individual electron charge distributions creating small instantaneous dipoles. The Hamiltonian can be approximated by:

$$H_v(r) \approx -C_6 r^{-6} \quad (3.5)$$

As the van der Waals interaction is spin independent no transitions between internal states can occur. However, the exchange interaction is spin dependent and can couple the singlet and triplet parts of the wavefunction leading to changes in the internal state of the colliding atoms.

The exchange interaction occurs when the electron clouds of two colliding atoms overlap. The individual spins of the electrons (\mathbf{S}_1 and \mathbf{S}_2) decouple from the nuclear spins and recombine to form molecular electronic spin states:

$$\mathbf{S} = \mathbf{S}_1 + \mathbf{S}_2$$

Similarly the nuclear spins combine to form molecular nuclear spin states:

$$\mathbf{I} = \mathbf{I}_1 + \mathbf{I}_2$$

Therefore the total \mathbf{F} and m_F are conserved:

$$\mathbf{F} = \mathbf{S} + \mathbf{I}$$

and

$$m_F = m_{F1} + m_{F2}$$

The exchange interaction arises from the anti-symmetry of the electronic wavefunction of the two colliding atoms. At small inter-atomic separation the wavefunctions of the electrons overlap and there is a contribution to the energy of the resulting potential depending on the orientation of the valence electron spins. If the spins are anti-parallel ($S = S_1 + S_2 = 0$) then the two electrons can occupy the same orbital³ giving rise to a singlet potential. When the two electron spins are parallel ($S = S_1 + S_2 = 1$) their spin wavefunction is identical and therefore they cannot have the same spatial wavefunction. Therefore, due to the electron repulsion there is no reduction in the energy of the potential at short range. The potential therefore splits into two – singlet and triplet. They have corresponding scattering lengths denoted by a_T (triplet) and a_S (singlet). Figure 3.1 illustrates the splitting in the potential at short inter-atomic separation, that arises due to the exchange interaction. For most collisions the interaction potential is a mixture of the triplet and singlet potential. The exception to this rule is collisions between two atoms in the (4, 4) state and the collisions between atoms in the (4, +4) and (4, +3) state. For these collisions the interaction potential is purely triplet in nature.

For the exchange interaction, the inelastic loss rate coefficient for laser-cooled alkali metals is of the order $10^{-10} \text{ cm}^3 \text{ s}^{-1}$ [48]. Therefore to avoid these losses, atoms are polarized into the $|F = I \pm S, m_F = \pm F\rangle$ states.⁴

³The overlap of the electronic wavefunctions of two atoms with anti-parallel valence electron spins leads to a formation of a covalent bond between the atoms.

⁴For caesium, these states are $|F = 4, m_F = \pm 4\rangle$ and $|F = 3, m_F = \pm 3\rangle$.

The potential energy curves (Figure 3.1) can be broken into three distinct regions. At small inter-atomic separation ($r \leq 5a_0$) the interactions are dominated by the strong repulsive core due to the overlapping of electron clouds. At intermediate r , the exchange interaction is dominant and splitting of the potential into singlet and triplet parts occur. At large r ($r \geq 20a_0$) the magnitude of the splitting between the triplet and singlet potentials is reduced and the van der Waals interaction dominates. These effects are shown clearly in Figure 3.1.

The van der Waals energy and the exchange energy can be viewed as the mean energy or half the energy difference between the singlet and triplet potential, respectively:

$$V_v(r) = \frac{1}{2} (V_{S=0}(r) + V_{S=1}(r)) \quad (3.6)$$

$$V_{ex}(r) = \frac{1}{2} (V_{S=0}(r) - V_{S=1}(r)) \quad (3.7)$$

3.1.3 Dipolar Interaction

Losses from a magnetic trap due to the exchange interaction can be prevented by polarizing the trapped atoms into stretched states. Other weaker interactions can couple the stretched states to other internal states thus causing heating and loss from the trap. The most dominant interactions of this type are due to the dipolar interaction, H_d . This interaction occurs between the spin of the two colliding atoms and can be split into two main types: the direct magnetic dipole interaction (spin-spin dipole interaction) and the second-order spin-orbit interaction (or indirect spin-spin coupling). The complete Hamiltonian for dipolar relaxation is a sum of the spin-spin dipole interaction Hamiltonian and the second-order spin-orbit interaction Hamiltonian:

$$H_d = H_d^1 + H_d^2 \quad (3.8)$$

where H_d^1 and H_d^2 are given by the following expressions:

$$H_d^1 = V_1(r)V_S(S_1, S_2) \quad (3.9)$$

$$H_d^2 = V_2(r)V_S(S_1, S_2) \quad (3.10)$$

The spins of the atoms are coupled individually to the inter-atomic axis, therefore V_S commutes with the individual spins (S_1, S_2) and not the total spin (S). The orbital angular momentum quantum number (l), can therefore change by +2, 0, or -2. It is possible for two incoming atoms in an s -wave state ($l = 0$) to scatter into a d -wave state ($l = 2$). The extra angular momentum required is taken from the electronic spins. If the Zeeman energy released from the collision is small compared to the energy required to impart the angular momentum to the colliding atoms, then these inelastic collisions are suppressed.⁵ This suppression takes the form of a centrifugal term in the interaction Hamiltonian.

The spin-spin dipole interaction is due to the coupling between the magnetic dipole associated with the spin of one atom, with the magnetic field produced by the magnetic dipole of the colliding atom. The interaction lifts the degeneracy of the different electronic spin projections of the triplet state.

The second-order spin-orbit interaction creates the same effect as the spin-spin dipole interaction in that the degeneracy of the triplet state is lifted. When the electron clouds of the interacting atoms overlap, off-resonant coupling of the electronic wavefunctions to higher-lying electronic states can occur.

The observed effects from spin-spin dipole interaction and the second-order spin-orbit interaction are indistinguishable. The dipolar relaxation rate coefficient for most alkali metals is of the order $10^{-15} \text{ cm}^3 \text{ s}^{-1}$ [48]. The spin-spin dipole interaction occurs in all collisions involving alkali metal atoms and is primarily responsible for dipolar relaxation observed in hydrogen and the lighter alkali metals. However, the dipolar relaxation rate coefficient for Cs is of the order $10^{-12} \text{ cm}^3 \text{ s}^{-1}$ [24]. This large rate is attributed to the second-order spin-orbit interaction that occurs in collisions involving heavy alkali metals with large relativistic spin-orbit effects e.g. Cs and Rb. For ^{87}Rb , the effect of the spin-spin dipole and the second-order spin-orbit interactions are approximately equal and opposite, giving an anomalously small dipolar relaxation rate [48].

⁵To take advantage of the suppression of these collisions, experimentalists use very low magnetic fields (see Section 1.2.2, Chapter 2).

3.2 Scattering

Different quantum mechanical approaches are appropriate for studying scattering problems in different energy regimes: the Born approximation – high energy, and partial wave analysis – low energy.

In the Born approximation the energy eigenfunctions of the system are expressed as a linear combination of the incident and scattered waves. The effect of the interaction is treated as a weak perturbation and therefore the Born approximation method is only valid when the average energy of the interaction between the incident particle and the scatterer is much smaller than the incident particle's kinetic energy.

In partial wave analysis the incident plane wave is expressed as a linear combination of the eigenfunctions of the scattering potential. This method is useful in describing the scattering of plane waves from spherical objects. No limitations are placed on the strength of the interactions. This is the method most commonly used to describe inter-atomic scattering.

3.2.1 Partial Wave Analysis

The interaction Hamiltonian of two colliding structureless particles is:

$$H = -\frac{\hbar^2}{2\mu r^2} \frac{d}{dr} \left(r^2 \frac{d}{dr} \right) + \frac{\hbar^2 l(l+1)}{2\mu r^2} + V(r) \quad (3.11)$$

where μ and r are the reduced mass and the inter-atomic separation of the two interacting particles, respectively.

At small inter-atomic separation (r) the interaction potential $V(r)$, is of the order of the total energy and therefore the solutions are complicated. At large r , the magnitude of $V(r)$ is small and the wavefunctions tend towards the solutions of the general Schrödinger equation in the absence of the interaction potential term. In the asymptotic region (large r) the interaction Hamiltonian has solution of the form:

$$\psi_l(r) \sim \frac{\sin [kr + \delta_l(k)]}{r} \quad (3.12)$$

where k is the deBroglie wave vector and is given by:

$$k = \left(\frac{16mk_{\text{B}}T}{\pi\hbar^2} \right)^{\frac{1}{2}} \quad (3.13)$$

δ_l is called the phase shift and is known to reflect the effect of the potential on the scattered wave (see Reference [95]). The phase shifts cannot be directly measured, however they are related to the collision cross-section (which is experimentally measurable) by the following equation:

$$\sigma = \frac{4\pi}{k^2} \sum_{l=0}^{\infty} (2l+1) \sin^2 \delta_l \quad (3.14)$$

where $k = \sqrt{2\mu E}/\hbar$ and the sum is over all possible partial waves with angular momentum l .

Symmetry requirements affect the partial waves allowed in collisions involving identical particles. For fermions, s -wave collisions are forbidden because of the Pauli exclusion principle which states that atoms cannot have the same spatial and spin wavefunctions. Therefore only odd l -wave collisions occur (p -wave, f -wave, etc). For bosons, only partial waves of even l (s -wave, d -wave, etc) are allowed because of the symmetry of the wavefunction.

Hard Sphere Scattering

Consider a potential of the form:

$$V(r) = \begin{cases} 0 & r > a \\ \infty & r \leq a \end{cases} \quad (3.15)$$

Figure 3.2 illustrates the form of the potential and the incident and scattered waves.⁶ The incident wavefunction is continuous at the origin ($r = 0$) and the scattered wavefunction is continuous at $r = a$. The phase shift is therefore proportional to a . This illustrates why scattering from a potential can be compared to hard sphere scattering.

For s -wave scattering ($ka \ll 1$), the phase shift between the incident and scattered wavefunction is ka . The total cross-section is obtained by substituting

⁶This is an over simplification of scattering, but it is useful for understanding the physical origin of the phase shift.

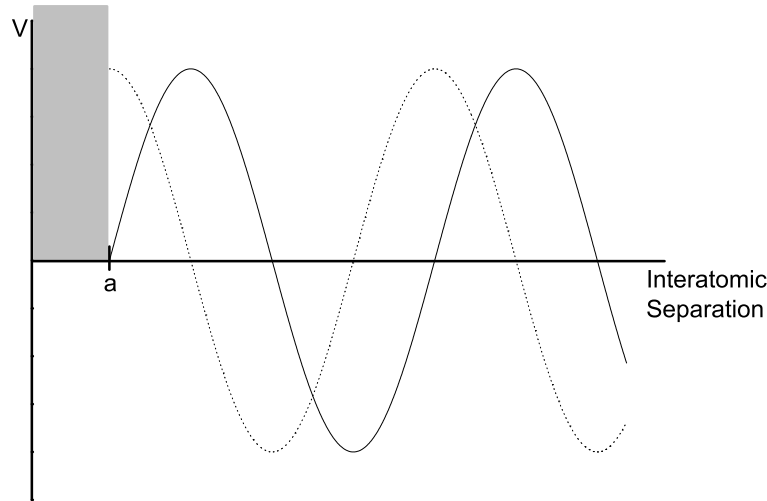


Figure 3.2: Scattering from a hard sphere potential. The dotted line (\cdots) is the incident wave and the solid line ($-$) is the scattered wave.

this value into Equation 3.14 to give:

$$\sigma = \frac{4\pi}{k^2} \sin^2(-ka) \approx 4\pi a^2 \quad (3.16)$$

The geometrical cross-section is πa^2 , therefore the scattering cross-section is a factor of 4 larger.

3.2.2 Scattering Length

Ground state collisions can be described by one parameter, the scattering length a . The scattering length can be thought of as the radius of a hard sphere that would produce the same scattered wavefunction as scattering from an inter-atomic potential.⁷

The Wigner threshold laws state that for low enough energies, the phase shift δ_0 is inversely proportional to the wavevector k of the atom motion. The expression for the scattering length is given by:

$$a = -\lim_{k \rightarrow 0} \frac{\delta_0}{k} \quad (3.17)$$

The scattering length characterizes the strength of the interactions and therefore can be negative, zero, or positive. Figure 3.3 illustrates schematically how

⁷In Figure 3.2 the scattering length is a .

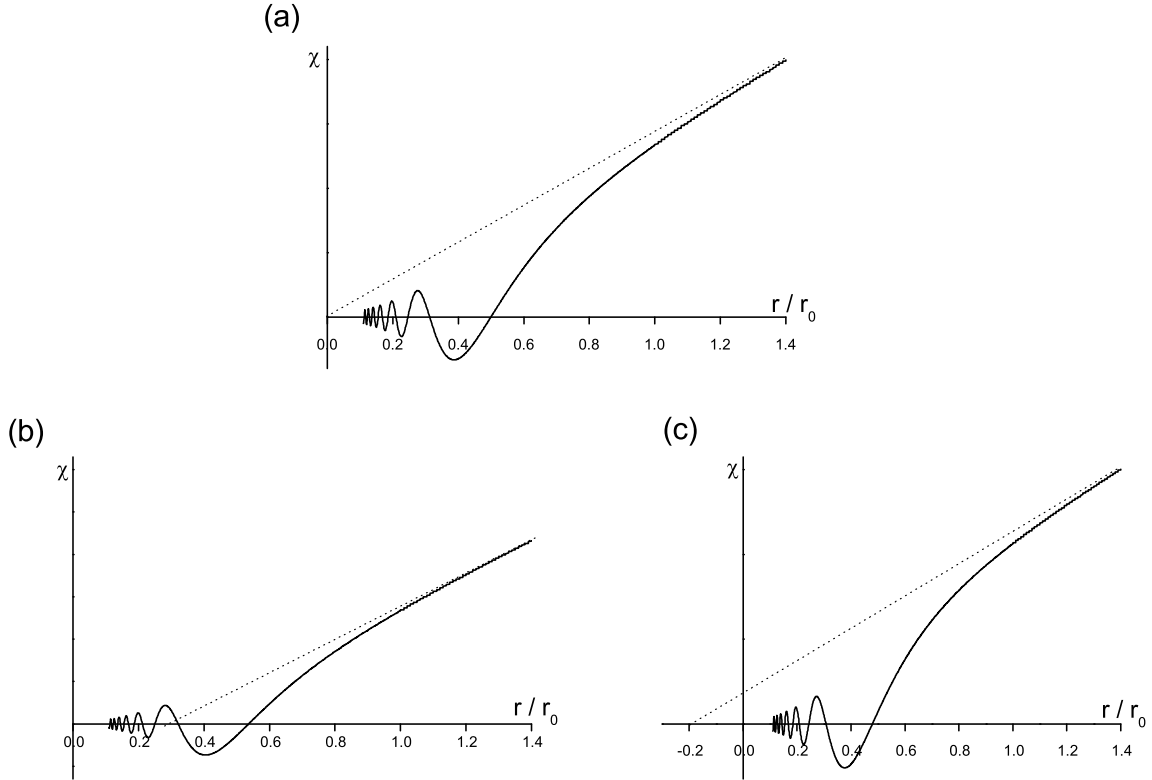


Figure 3.3: Schematic behaviour of the wavefunctions of the colliding atoms. The curves in (a), (b) and (c) correspond to zero, positive and negative scattering lengths respectively. χ is the radial wavefunction multiplied by r . (The wavefunction equation used to generate the plots was obtained from Reference [96].)

these changes in the scattering length arise.

3.2.3 Scattering at Low Temperatures

The number of partial waves involved in a collision depends on the energy of the colliding particles. The only partial waves that contribute to the cross-section are those which satisfy the following condition:

$$ka > \sqrt{l(l+1)} \quad (3.18)$$

where a is the scattering length.

For low temperatures $ka \ll 1$, and therefore only the $l = 0$ partial waves (s -waves) contribute to the scattering cross-section. Equation 3.14 simplifies to:

$$\sigma = \frac{4\pi}{k^2} \sin^2 \delta_0 \quad (3.19)$$

For bosons, the probability of occupation of a quantum state is enhanced by a factor $(N+1)$ where N is the number of bosons in the state [97], therefore a factor of 2 must be included in the scattering cross-section expression (Equation 3.19):

$$\sigma = \frac{8\pi}{k^2} \sin^2 \delta_0 \quad (3.20)$$

To determine the energy thresholds at which other partial waves start to contribute to the cross-section, Equation 3.21 (obtained from Reference [84]) must be evaluated:

$$l(l+1) = \left(\frac{n\mu C_n}{\hbar^2} \right) \left(\frac{3k_B T}{(n-2)C_n} \right)^{(n-2)/n} \quad (3.21)$$

where n is the order of the interaction, C_n is the corresponding coefficient and μ is the reduced mass.

For caesium, the approximate temperature thresholds at which other partial waves start to contribute are 200 μK for p -waves ($l = 1$), 1 mK for d -waves ($l = 2$) and 3 mK for f -waves ($l = 5$). Odd number partial waves are forbidden for bosons and therefore when the temperature is less than 1 mK (d -wave threshold), only s -waves are considered.

3.3 Resonances

Resonances occur when the elastic or inelastic cross-section is enhanced due to the presence of a bound state at an energy close to the energy of the colliding atoms. Two different types of resonances are generally observed in cold-atom collisions:

- Potential resonance – these occur when there is a coincidence of a bound state of the potential with zero energy.
- Feshbach resonance – these are a coincidence of a quasi-bound molecular state with the energy of the colliding atoms.

These two types of resonances are observed in the $F = 3$, $m_F = -3$ state in caesium and are discussed in greater detail in the following sections.

3.3.1 Potential Resonances

An inter-atomic potential can support many bound states, particularly if the potential is deep. During scattering, the energy of the entrance channel is greater than the dissociation energy (zero-energy) of the molecular state and therefore the existence of bound states has no effect on the scattering.⁸ However, when the last bound state⁹ of the molecular potential is close to the energy of the scattering channel potential and the energy of incidence of the two scattering particles is small ($ka \ll 1$), resonances in the scattering cross-section occur.

If the depth of the potential is increased then more bound states can be supported. As each extra bound state that is added to the potential passes through the zero of energy, a resonance occurs. The phase shift of the wavefunction increases by π across the resonance and the width of the resonance becomes narrower as the depth of the the potential increases. The scattering length also becomes very large and goes through infinity on passing through each resonance.

Immediately prior to each resonance the total phase shift¹⁰ is an integer multiple of π and therefore the cross-section is zero.¹¹ The scattered wave is in phase with the incident wave and therefore the particles do not collide, they pass through one another.

On resonance, the phase-shift is equal to $\pi/2$ and Equation 3.20 and therefore the cross-section takes it maximum value:

$$\sigma = \frac{8\pi}{k^2} \quad (3.22)$$

This is known as the unitarity limit, and in this limit the cross-section is orders of magnitude greater than the off-resonance value. This increases the probability of collisions in an atom cloud.

⁸Strictly speaking, in quantum mechanical treatment of scattering, all bound states must be included in the complete Hamiltonian.

⁹When $l \neq 0$ the potential can support quasibound states above the dissociation threshold. These give rise to what is known as shape resonances which behave like Feshbach resonances.

¹⁰Levinson's theorem [98] states that the total phase shift is directly related to the number of bound states in the potential.

¹¹This is known as the Ramsauer-Townsend effect and was first observed in 1921 [99, 100].

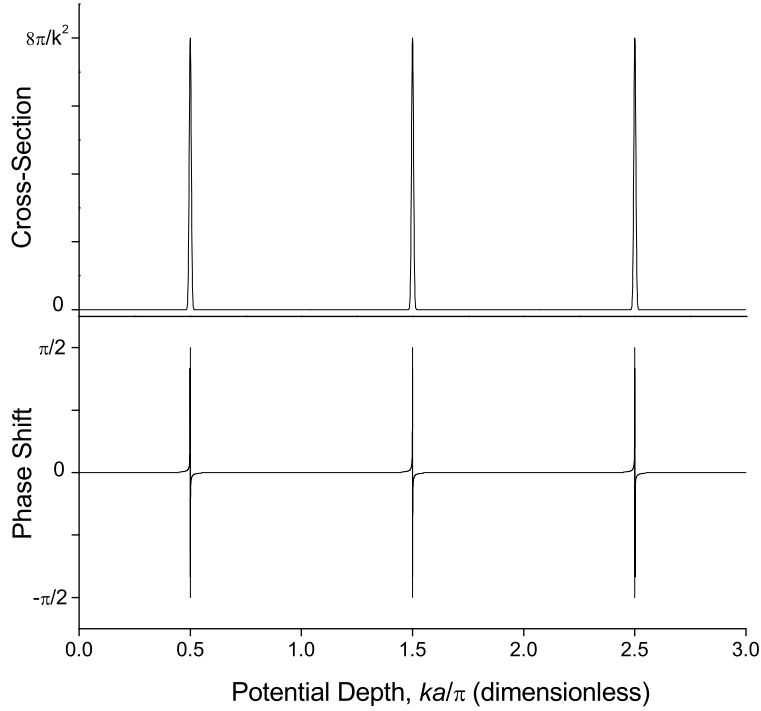


Figure 3.4: The effect of the depth of the potential on the collisional cross-section and the phase-shift.

When the last bound state is very close to the dissociation limit (i.e. the scattering length is large but not equal to infinity) the first order approximation of the cross-section is:

$$\sigma = \frac{8\pi a^2}{1 + k^2 a^2} \quad (3.23)$$

which reduces to Equation 3.22 when $ka \gg 1$. At low temperatures ($ka \ll 1$):

$$\sigma = 8\pi a^2$$

The extra factor of 2 compared to the hard sphere scattering cross-section result (Equation 3.16) arises from the indistinguishability of bosons.

These potential resonances have been observed in Cs in both singlet and triplet potentials. The existence of these resonances can partially explain why Cs exhibits dramatically different behaviour to other lighter alkalis. It also explains the energy dependence of the low-temperature elastic cross-section [25].

3.3.2 Feshbach Resonances

Feshbach resonances occur when the total energy of the entrance channel matches the energy of a bound state in a closed channel. The incident particles “virtually” occupy the bound state for a brief period of time and therefore spend an increased amount of time at short range than they would normally. This causes a resonant change in the elastic and inelastic cross-sections (or equivalently the scattering length). The smaller the difference between the energy of the atoms in the exit and entrance channels the larger the changes in the collisional cross-section. The sign of the scattering length also depends on the position of the bound state relative to the energy of the entrance channel. If the energy of the bound state is greater than the energy of the entrance channel then the scattering length is negative i.e. the interaction is attractive.

The energies of the bound states in the potential depend on external parameters including magnetic field. The magnetic field dependence of the energy of the bound state is in general different to the dependence of the energy of the binary scattering state on magnetic field. Therefore both the magnitude and the sign of the effective atom-atom interactions can be tuned.

Figure 3.5 illustrates schematically the principles of a Feshbach resonance. In elastic scattering, the colliding atoms enter and exit the potential in the same channel. In an elastic Feshbach resonance this is still true except this time there is a delay introduced in the outgoing wave which is equivalent to a change in the phase shift. As seen previously (Equation 3.14) this leads to a change in the collisional cross-section. In inelastic scattering, the outgoing channel is lower in energy than the entrance channel and atoms change channel because of non-adiabatic transitions that occur at short-range curve crossings. In an inelastic Feshbach resonance the inelastic cross-section also changes due to the increased time the atoms spend at short range.

The width of a Feshbach resonance depends on the coupling between the entrance and exit channels. Therefore, unlike as in the case for potential resonances, there is no limit to the width of a resonance.

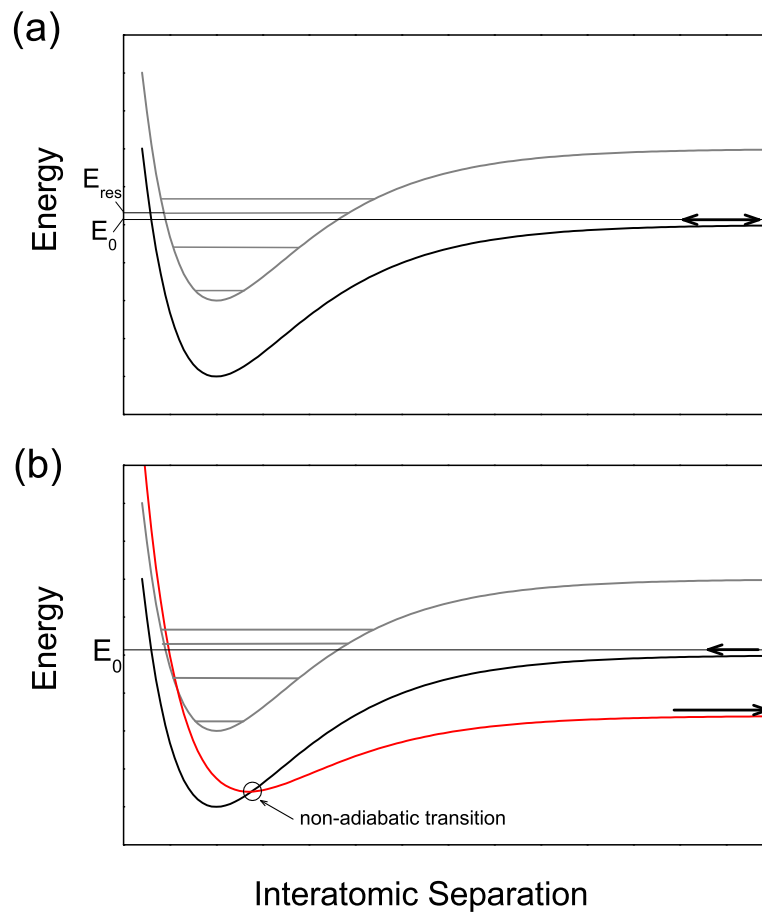


Figure 3.5: A plot of the potential energy curves for two different channels that illustrate the formation of Feshbach resonances. E_{res} is the energy of a state in a closed channel and E_0 is the threshold energy for the entrance channel. In (a), the phase shift of the outgoing wave with respect to the incident wave causes a resonant alteration of the elastic cross-section. In (b) inelastic collisions are strongly enhanced due to the existence of an avoided crossing between the entrance channel and a lower-lying outgoing channel. (Figure modified from Reference [101].)

Feshbach resonances have been observed in many alkali metal experiments – ^{23}Na [16], ^{85}Rb [102], ^{87}Rb [103], ^6Li [104, 105], ^{133}Cs [38] and ^{40}K [106].

Evaporative Cooling

The technique of forced evaporation has been very successful in many experiments involving trapped alkali metal atoms. This technique involves driving radio-frequency (rf) transitions that selectively remove the hottest atoms from the trap. Typically atoms with energies greater than $\eta k_B T$ ($\eta \approx 5$) are removed from a trap containing a cloud of atoms at temperature T and the cloud then rethermalizes through elastic collisions to a lower temperature. The Maxwell-Boltzmann distribution is therefore continuously truncated at a value of $\eta k_B T$ and the high energy tail of the distribution is continually replenished through elastic collisions. The rate of evaporative cooling is determined by how rapidly the sample rethermalizes through elastic collisions. Additionally, the rate of the inelastic loss processes impacts on the efficiency of the cooling process.

Evaporative cooling is crucial to attain BEC and has been studied in detail [107, 108, 109, 110]. An excellent review article on evaporative cooling is Reference [111].

Prior to constructing a BEC experiment it is important to consider the factors that affect the evaporation.¹ The choice of magnetic field and trapping frequencies strongly affect the evaporation performance and therefore these factors need to be considered not only when evaporating but also before construction of the magnetic trap. The choice of magnetic trap depends on the trapping frequencies required and

¹This is particularly true for elements that are difficult to condense e.g. ^{85}Rb and Cs .

the range of magnetic fields that need to be accessed. This chapter is a discussion of the factors that affect the evaporation performance.

4.1 Elastic and Inelastic Collisions

The efficiency of evaporative cooling depends on the elastic collision rate and the loss and heating rates due to inelastic collisions. To decide on an evaporation strategy the dependence of these rates on magnetic field and trap frequencies must be considered.

4.1.1 Elastic Collisions

Elastic collisions are required to rethermalize the cloud of atoms. The elastic collision rate is given by the following equation:

$$\Gamma_{\text{elastic}} = \langle n \rangle \sigma \langle v_{\text{rel}} \rangle \quad (4.1)$$

where $\langle n \rangle$ is the mean density and σ is the elastic collision cross-section:

$$\sigma = \frac{8\pi a^2}{1 + k^2 a^2} \quad (4.2)$$

k is the deBroglie wave vector and is defined in Equation 3.13, Chapter 3. v_{rel} is the average relative speed of the atoms in a trap given by the following equation:

$$\langle v_{\text{rel}} \rangle = \left(\frac{16k_{\text{B}}T}{m\pi} \right)^{\frac{1}{2}} \quad (4.3)$$

4.1.2 Inelastic Collisions

The efficiency of evaporation does not just depend on elastic collisions but also on loss processes. A low elastic collision rate by itself is not necessarily a problem. However, there is another timescale of importance, namely the lifetime of an atom in the magnetic trap. Three processes contribute to losses in the magnetic trap:

1. Background collisions (loss rate= $1/\tau_{\text{b}}$). Indiscriminate collisions between cold trapped atoms and room temperature atoms in the background gas give a loss rate per atom that is only dependent upon the vapour pressure of the

background gas. The loss rate from this process equals $1/\tau_b$ where τ_b is the lifetime in the trap at a density low enough that the density dependent losses can be ignored. The average mean energy of an atom lost from the trap due to background collisions is $3k_B T$.

2. Two-body collisions – dipole relaxation (rate constant, K_2). These inelastic collisions occur between two trapped atoms, in which the two atoms exchange angular momentum between their orbital motion and their intrinsic spin, thereby scattering into un-trapped spin states. These collisions result from both the direct magnetic dipole-dipole interaction and the indirect second-order spin-orbit interaction. As the loss rate is proportional to the density, the atoms lost from the trap have a lower than average energy, $E_2 = \frac{9}{4}k_B T$.
3. Three-body collisions – molecule formation (rate constant, K_3). Three atoms collide in such a way that two form a molecule, whilst the third atom is necessary to conserve energy and momentum. This process becomes significant at high densities. The mean energy of an atom lost from the trap due to three-body collisions is, $E_3 = 2k_B T$.

The last two processes are density dependent, therefore atoms are preferentially lost from the the cold dense centre of the trap, resulting in an additional heating of the sample (anti-evaporation). For a magnetically trapped gas containing N atoms, the total loss rate is:

$$\Gamma = \frac{dN}{dt} = -\frac{N}{\tau_b} - K_2 \langle n \rangle N - K_3 \langle n^2 \rangle N \quad (4.4)$$

where

$$\langle n \rangle = \frac{1}{N} \int n^2(\mathbf{r}) d^3\mathbf{r}$$

and for a Gaussian distribution,

$$\langle n^2 \rangle = \frac{1}{N} \int n^3(\mathbf{r}) d^3\mathbf{r} = \frac{8}{\sqrt{27}} \langle n \rangle^2$$

4.2 Efficiency of Evaporation

The efficiency of the evaporative cooling process is determined by the ratio R of elastic (good) to inelastic (bad) collisions. Any evaporation strategy must maximize this ratio. For efficient ‘runaway’ evaporation, R is typically greater than 100.² In many experiments the technique of adiabatic compression is employed to increase the initial elastic collision rate in the gas while maintaining the phase space density.

For a change in trap frequencies to be considered adiabatic [112] the following criteria must be satisfied:

$$\frac{d\omega}{dt} \ll \omega^2, \Gamma_{\text{elastic}}^2$$

During an adiabatic compression the entropy and thus the PSD is conserved.

The peak density n_{pk} is proportional to $\omega^3/T^{3/2}$ where $\omega^3 = \omega_r^2\omega_z$. The average velocity is proportional to $T^{1/2}$ and therefore, if we assume that the elastic cross-section is independent of the temperature, Equation 4.1 gives:

$$\Gamma_{\text{elastic}} \propto \frac{\omega^3}{T} \quad (4.5)$$

During adiabatic compression ω/T is fixed and therefore the elastic collision rate is:

$$\Gamma_{\text{elastic}} \propto \omega^2 \quad (4.6)$$

At finite temperatures, the collision cross-section is described by Equation 4.2. At high temperatures $ka \gg 1$, the elastic collision cross-section reduces to:

$$\sigma = \frac{8\pi}{k^2} \propto \frac{1}{T}$$

Therefore, the dependence of the elastic collision rate on the trap frequencies is reduced to:

$$\Gamma'_{\text{elastic}} \propto \omega \quad (4.7)$$

To determine the threshold for ‘high temperature’ behaviour, we can set ka equal to 1. This gives an equation for the threshold temperature in terms of the

²This factor is much higher if inelastic collisions in addition to background collisions are considered. This factor is also affected by the geometry of the magnetic trap.

mass m , \hbar , k_B , and the scattering length a .

$$T = \frac{\pi\hbar^2}{16mk_B a^2} \quad (4.8)$$

For a scattering length of $2525 a_0$, the temperature threshold at which low temperature behaviour is observed is 40 nK. Therefore in order to benefit from large scattering lengths the cloud must be cooled significantly.

At first glance, Equations 4.6 and 4.7 suggest that a tighter trap would be beneficial. Not only is there an increase in the elastic collision rate (Equation 4.6) but the problem of gravity which is inherent in weak traps is avoided (Section 2.5.2, Chapter 2) and the BEC transition temperature is higher

$$k_B T_c = 0.94\hbar\omega N^{\frac{1}{3}} \text{ where } \omega = (\omega_r^2\omega_z)^{\frac{1}{3}} \quad (4.9)$$

which means that the absolute heating rate is less important.

However, on analysis of the inelastic scattering rates, adiabatic compression does not appear to be advantageous. Consider three scenarios:

1. If the loss rates are dominated by background collisions. Background collisions are independent of trap frequencies therefore the optimum value of the ratio of elastic to inelastic collisions R , is also the optimum value of the elastic collision rate, Γ_{elastic} .
2. If the loss rates are dominated by three-body collisions:

$$R = \frac{\Gamma_{\text{elastic}}}{\Gamma_{\text{3-body}}} = \frac{6\sqrt{3}\pi\sigma k_B^2 T^2}{N\omega^3 m^2 K_3} \propto \frac{\sigma}{\omega} \quad (4.10)$$

If the elastic collisional cross-section is independent of temperature then

$$R \propto \frac{1}{\omega}$$

However, if the elastic cross-section is proportional to $1/T$ then

$$R' \propto \frac{1}{\omega^2}$$

Increasing the trap frequencies therefore makes the ratio of good to bad collisions worse.

3. If the loss rates are dominated by two-body collisions:

$$R = \frac{\Gamma_{\text{elastic}}}{\Gamma_{\text{2-body}}} = \frac{4\sigma}{K_2} \sqrt{\frac{k_B T}{\pi m}} \propto \omega^{\frac{1}{2}} \quad (4.11)$$

If the elastic collisional cross-section is independent of temperature then

$$R \propto \omega^{\frac{1}{2}}$$

As the temperature is decreased the value of R decreases, leading to a reduction in the efficiency of the evaporation. If the trap frequencies are increased then the ratio of elastic to inelastic collisions should improve. However, if the elastic cross-section is proportional to $1/T$ then

$$R' \propto \frac{1}{\omega^{\frac{1}{2}}}$$

Once again, increasing the trap frequencies makes the evaporation less efficient.

Any evaporation strategy maximizes the ratio of elastic to inelastic collisions and hence it must take into account which of the loss mechanisms is dominant. The technique of adiabatic compression is beneficial if background losses are dominant (the case for most alkali experiments), but not when the three-body loss mechanism is dominant. In the case of caesium in the $F = 3, m_F = -3$ state, two-body collisions have been observed to be the dominant loss mechanism. Table 4.1 states the ratio of elastic to inelastic loss rates for each individual loss mechanism.

As the caesium two-body loss rates are very high (more than a few orders of magnitude higher than for other alkalis), it is tempting to jump to a conclusion and state that, for a temperature independent cross-section, improved evaporation rates could be obtained by increasing the trap frequencies. However, another factor must be taken into account before finalizing the evaporation strategy.

4.2.1 Hydrodynamic (Collisionally thick) regime

Ordinarily in BEC experiments (e.g. ^{87}Rb), each atom in the sample undergoes many undisturbed harmonic oscillations between collisions. However, in caesium

Dominant Loss Mechanism	Ratio of Elastic and Inelastic Collisions	Adiabatic Compression	
		σ constant	$\sigma \propto \frac{1}{T}$
Background Loss:	$R = \frac{Nm\sigma\omega^3}{4\pi^2\tau_b k_B T}$	$\propto \omega^2$	$\propto \omega$
2-Body Loss:	$R = \frac{4\sigma}{K_2} \sqrt{\frac{k_B T}{\pi m}}$	$\propto \omega^{\frac{1}{2}}$	$\propto \omega^{-\frac{1}{2}}$
3-Body Loss:	$R = \frac{6\sqrt{3}\pi\sigma k_B^2 T^2}{N\omega^3 m^2 K_3}$	$\propto \omega^{-1}$	$\propto \omega^{-2}$

Table 4.1: Summary of the dependence of the ratio of elastic to inelastic collisions R , on the trap frequencies.

experiments each atom can undergo many collisions in a typical trap oscillation period as a consequence of the enormous collision cross-sections. This behaviour restricts the evaporative cooling process, since although the local thermalization rate is high, it takes a time on the order of the trap oscillation period for the sample as a whole to rethermalize. In this regime, the ratio of good to bad collisions, which is normally independent of the density when two-body losses are dominant, scales as:

$$\frac{\omega}{K_2 \langle n \rangle}$$

Consequently as the evaporation proceeds and the density rises, this ratio falls and the evaporation process becomes increasingly inefficient, eventually failing altogether. The atom cloud enters the hydrodynamic regime when the elastic collision rates reaches the value of the order of the radial trap frequency. When the elastic collision rate is limited by the radial trap frequency, increasing the trap frequencies does not increase the elastic collision rate. However, the inelastic loss rates continue to rise with increasing trap frequencies leading to a decrease in the evaporative cooling efficiency.

The early experiments in the $(3, -3)$ state [33, 26] both noticed a decrease in the efficiency of the evaporation during the latter stages of evaporation. This decrease can be attributed to the onset of the hydrodynamic regime. Table 4.2 states the trap frequencies and the final PSD attained by the experiments in Paris and Oxford. Our calculation of their collision rate at the end of their evaporation clearly shows that in both experiments the atom cloud had entered the hydrodynamic regime.

	ω_r (Hz)	ω_z (Hz)	ω (Hz)	PSD	Collision Rate (s^{-1})
Dalibard <i>et al.</i>	87	7	38	3×10^{-2}	190
Foot <i>et al.</i>	16	45	23	2.4×10^{-3}	60

Table 4.2: Summary of the results of the Paris and Oxford experiments.

If we accept that the hydrodynamic regime is unavoidable, then at the critical temperature the ratio of good to bad collisions scales as:

$$\frac{1}{\sqrt{\omega}}$$

This expression holds when two-body inelastic collisions are the dominant loss process and when the collisions are unitarity limited (Table 4.1). Hence, operating with low trap frequencies is advantageous. The hydrodynamic regime can, of course, be avoided by reducing the elastic collision cross-section using a Feshbach resonance. This is also an option in caesium, although the two-body inelastic collision rate is expected to increase in the vicinity of the Feshbach resonances in the $(3, -3)$ state [37].

4.3 Evaporative Cooling Models

The process of evaporative cooling has been the subject of several theoretical studies and the process can be modelled using several different methods. Some methods approximate the evaporation process as a series of truncation events followed by rethermalization of the atom cloud [92]. Other methods assume a quasi-equilibrium during evaporation, which is a valid assumption as confirmed by Luiten *et al.* [34].

A simple model of evaporative cooling was used to test the effect of various factors on the evaporation. In Section 7.1, Chapter 7 this method is used to demonstrate the effect of the hydrodynamic regime on the evaporation trajectory. The model is similar to the model described in [113]. Coupled differential equations are used to describe the cooling, heating and loss processes during evaporation.

Monte-Carlo simulations are a quantitative theoretical account of evaporation and can describe realistic experimental situations. There are many variations of the Monte-Carlo simulation. Two methods were developed in 1996 which solved the classical kinetic equation [108, 107]. The method described in Section 4.3.2 is a simulation of the motion of atoms in a harmonic magnetic trapping potential and it employs the direct Monte-Carlo method described in [114]. The method was used by Z.-Y. Ma to simulate the experimental evaporation results described in Section 7.3, Chapter 7.

4.3.1 Simple Model of Evaporative Cooling

The rate at which atoms with energy greater than η are produced as a function of time in a Ioffe quadrupole trap is approximately $\Gamma_{\text{elastic}}\eta \exp(-\eta)$ when η is greater than 3 .³ When the evaporation becomes one dimensional (Section 2.5.1, Chapter 2) the rate of atoms produced with an energy greater than η drops to $\approx \Gamma_{\text{elastic}} \exp(-\eta)$. This indicates that one-dimensional evaporation is less efficient than higher dimensionality evaporation. The evolution of the number and energy due to elastic collisions is given by the following equations:

$$\dot{N}_e = -N n_{\text{pk}} \sigma v \eta \exp(-\eta) \quad (4.12)$$

$$\dot{E}_e = (\eta + \kappa) k_B T(t) \dot{N}_e \quad (4.13)$$

n_{pk} is the peak density and is defined by the following equation:

$$n_{\text{pk}} = \frac{N(t)}{V_{\text{eff}}} \text{ where } V_{\text{eff}} = \frac{1}{\omega_r^2 \omega_z} \left(\frac{2\pi k_B T(t)}{m} \right)^{3/2} \quad (4.14)$$

³The rate at which atoms are produced with an energy greater than η depends on the form of the trapping potential. For an explanation, and calculations of the rate for other trapping potentials, see Reference [34].

The mean energy of atoms removed through background gas collisions is $k_{\text{B}}T(t)$, therefore the equations describing background gas collisions are:

$$\dot{N}_{\text{b}} = -K_{\text{b}}N \quad (4.15)$$

$$\dot{E}_{\text{b}} = 3k_{\text{B}}T(t)\dot{N}_{\text{b}} \quad (4.16)$$

where K_{b} is the background loss rate and is given by $1/\tau_{\text{b}}$.

The equations describing two-body collisions are:

$$\dot{N}_2 = -\left(\frac{1}{2}\right)^{\frac{3}{2}} K_2 N n_{\text{pk}} \quad (4.17)$$

$$\dot{E}_2 = \frac{9}{4} k_{\text{B}}T(t)\dot{N}_2 \quad (4.18)$$

Three-body collisions are described by the two following equations:

$$\dot{N}_3 = -\left(\frac{1}{\sqrt{27}}\right)^{\frac{3}{2}} K_3 N n_{\text{pk}}^2 \quad (4.19)$$

$$\dot{E}_3 = 2k_{\text{B}}T(t)\dot{N}_3 \quad (4.20)$$

Conservation of energy and number result in two coupled differential equations that govern the evolution of the cloud during evaporation:

$$3k_{\text{B}}(T\dot{N} + N\dot{T}) = \dot{E}_e + \dot{E}_{\text{b}} + \dot{E}_2 + \dot{E}_3 \quad (4.21)$$

$$\dot{N} = \dot{N}_e + \dot{N}_{\text{b}} + \dot{N}_2 + \dot{N}_3 \quad (4.22)$$

One important assumption of this simple model is that all decay products generated from inelastic collisions leave the trapping potential before colliding with other atoms.⁴

4.3.2 Monte-Carlo Simulation

The Monte-Carlo method described in this section provided us with a quantitative theoretical account of a cloud of ^{133}Cs atoms in a harmonic trapping potential. The results of the simulation allow for a greater understanding of evaporative cooling. In particular, various parameters such as the trap frequencies, are varied in order to observe the effect on the efficiency of the evaporation.

⁴For a dense sample and if the cloud of atoms enters the hydrodynamic regime this assumption is false.

Simulation Structure

A cloud of atoms is considered to be completely enclosed in a cube. The dimension of the cube is 14σ where σ is the full width at half maximum (FWHM) of the atom cloud (fitted with a Gaussian). The cube is split into $30 \times 30 \times 30$ cells, and therefore each cell is of dimension $\frac{14\sigma}{30}$. Collisions between atoms only occur between two atoms are in the same cell and the probability of an atom undergoing a collision depends on the local density.

The atom number varies by up to 5 orders of magnitude from the beginning to the end of the evaporation. To eliminate the inaccuracies that would arise from this change, a duplication technique is used [33] where a ‘macro-atom’ is used to represent many atoms. At the start of the evaporation 10 000 macro-atoms are used to represent 10^8 atoms. Therefore each macro-atom represents p real atoms, with $p = 2^{15} = 32768$ at the beginning of the simulation. Each macro-atom has the same mass and the same magnetic moment as a Cs atom, however the collisional cross-section is p times larger than for real atoms. When the number of macro-atoms falls to less than half the original value (5 000), either because of evaporation or collisional losses, each macro-atom is replaced by two new macro-atoms, each of which represents $p/2$ atoms. If the original macro-atom was at a position (x, y, z) with velocity (v_x, v_y, v_z) , one new macro-atom is placed at the same position with the same velocity. The other macro-atom is placed at $(x - v_x\delta t, y - v_y\delta t, z - v_z\delta t)$ with velocity $(-v_x, -v_y, -v_z)$.⁵ A small displacement between the two new macro-atoms is required to ensure that they will not undergo a collision because of the duplication process. During each duplication process the size of the cloud is calculated and the dimensions of the cells are reduced accordingly. The duplication process stops when $p = 1$ however it is important to maintain a sufficient number of atoms per cell to keep the collisional properties statically stable.

Initially, 10 000 macro-atoms are positioned in the box in a Gaussian distri-

⁵This expression for the new position is used instead of $(-x, -y, -z)$ which is the expression used in [33] as the geometry of the atomic cloud can be asymmetric after one-dimensional evaporative cooling, especially in the hydrodynamic regime.

bution in both space and velocity. Each atom is represented by 7 parameters: 3 spatial (x, y, z) , 3 velocity (v_x, v_y, v_z) , and the cell number. By using a classical model, the initial position and momentum of the atoms is sufficient information to determine their future movements completely.

Evaporation

When simulating the evaporation, the evaporation surface is chosen to be a plane cutting surface approaching from one side of the cloud. This reproduces the experimental situation as the atom cloud is sagged in the magnetic trap due to gravity. The cutting surface begins at a radius where the atomic potential radius is equal to $5k_B T$. The rate of cutting is controlled by varying the duration of the evaporation process.

The inter-atomic collisions are assumed to be binary and instantaneous and they are treated classically i.e. energy and momentum are conserved.⁶ The cross-section of the atoms is given by Equation 4.2. The choice of atom pairs that collide in a single cell and the probability of the collision occurring depends on the local density and the relative velocity of the atoms. The pre-collision velocities are replaced by the post-collision values as determined by a Monte-Carlo method. For each iteration the velocity of all the atoms must be recalculated as their velocity changes regardless of whether they collide or not as they are moving in a harmonic trapping potential.

Equation 4.4 describes the decay of a trapped atomic gas with density $\langle n \rangle$. We assume τ_b to be constant and equal to the experimental value (≈ 500 s).

The two-body loss coefficient K_2 exhibits a dependence on the energy of the colliding atoms [37] and at approximately 150 G scales as:

$$K_2 \approx \frac{K_2^0}{1.017 + \alpha T} \quad (4.23)$$

where $K_2^0 = 23.608 \times 10^{-19} \text{ m}^3 \text{ s}^{-1}$, $\alpha = 5.3 \times 10^6 \text{ K}^{-1}$ and T is the temperature of the cloud. Equation 4.23 is obtained from the theoretical calculation supplied by Julienne and co-workers at NIST.

⁶The internal degrees of freedom are ignored.

The form for the three-body loss coefficient is unknown, though it has been studied in detail in the (3, +3) state [115]. Our experimental observations indicate that it is negligible compared to two-body inelastic loss and therefore three-body collisions are ignored in the simulation.

The size of the cloud reduces as the cloud cools and therefore the cell sizes are scaled accordingly. The new FWHM is given by:

$$\sigma = \sigma_0 - \delta t n_{it}$$

where σ_0 is the original FWHM and n_{it} is the number of iterations.

Results

The Monte-Carlo simulation was extremely useful as we could test the effect of changing various experimental parameters on the evaporation. The results of the simulation are presented and discussed in more detail in Reference [52]. The simulation was used to study the following effects:

- the dependence of the end PSD on the initial PSD i.e. does an increase in the PSD on loading the magnetic trap become an increase in the PSD attained at the end of the evaporation. The simulation results showed that even if the initial PSD is increased by a factor of 10 there is no improvement in the end PSD.
- the optimum value of the duration of the evaporation. The theoretical results show that the evaporation performance is not very sensitive to the duration of the evaporation.⁷
- the evaporation efficiency in a spherical trap as a function of the trap frequency. The efficiency in and out of the hydrodynamic regime was also compared.
- the effect of the geometry of the cloud on the evaporation efficiency. The results of the simulation show that a pancake shaped cloud (in the horizontal

⁷For comparison with experimental results see Figure 7.11, Chapter 7.

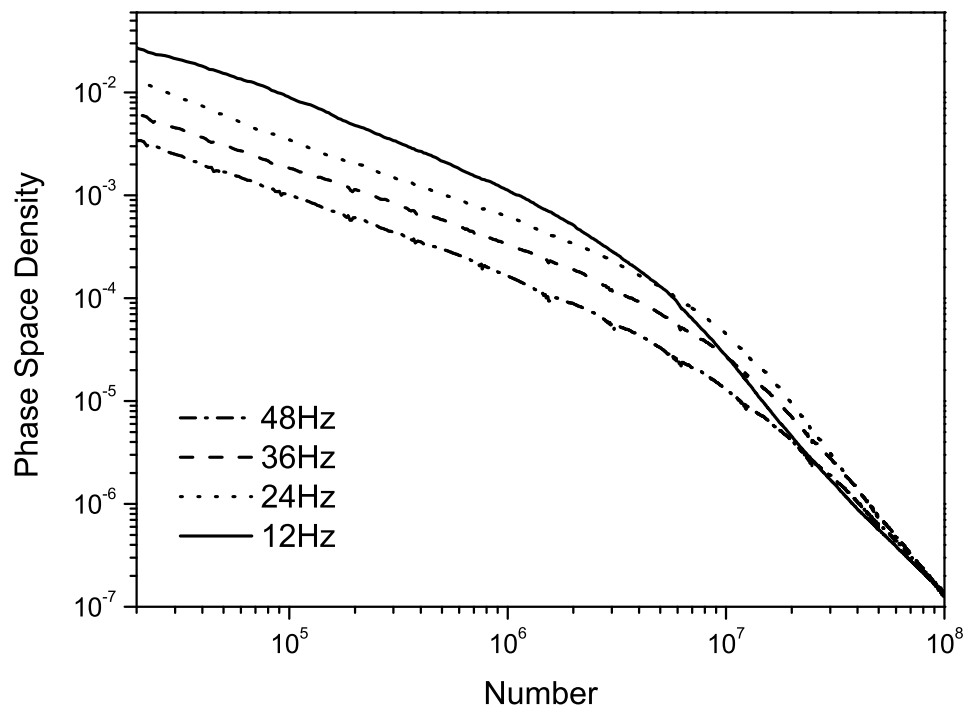


Figure 4.1: Evaporative cooling trajectories for different spherical trap frequencies. (The duration of the evaporation is optimized for each different trap frequency.)

direction) is beneficial when the evaporation is one-dimensional as the surface where atoms are removed by the rf is in contact with a larger area of the cloud.

- the rethermalization rate in and out of the hydrodynamic regime. The rethermalization rate tends asymptotically to a value which is approximately equal to the trap frequency.
- the effect of relaxing the trapping frequencies on the evaporation performance. The higher the trap frequencies the earlier in the evaporation the cloud enters the hydrodynamic regime and therefore the lower the PSD attained at the end of the evaporation. Figure 4.1 illustrates the effect of varying the trap frequencies on the evaporative cooling trajectory.

4.4 Evaporation Strategy

Consideration of the factors discussed in Section 4.2 led us to the conclusion that the optimum trap frequencies for efficient evaporation is less than 10 Hz. The high scattering lengths in caesium make it impossible for us to avoid the hydrodynamic regime, therefore operating in magnetic traps with low trap frequencies should improve the ratio of good to bad collisions (Section 4.2.1).

The magnetic bias field is more difficult to optimize, as the efficiency of the evaporation in the early stages is not always indicative of the evaporation performance in the later stages. The experimental data taken at Stanford [38] and the subsequent theoretical analysis at NIST [37] determined the cold-collision properties of caesium. By studying the ratio of elastic collisions to two-body inelastic collisions (Figure 1.1, Chapter 1) we were able to narrow down the range of magnetic fields at which to evaporate. The most promising magnetic field range was above all the Feshbach resonances at magnetic fields greater than 137 G.

A baseball trap and additional bias coils (see Section 2.4, Chapter 2) were built in order to operate at high magnetic fields and in weak magnetic trapping potentials. Chapter 7 contains the experimental results of our evaporation studies.

Experimental Apparatus

This chapter is devoted to the experimental apparatus developed as part of this work and used to take all the measurements that will be detailed in Chapters 6 and 7. The focus will be on the techniques and parts of the experimental apparatus that are, within the Oxford BEC group, unique.

5.1 Apparatus

5.1.1 Lasers

As explained in Chapter 2, many different light frequencies are required for trapping, cooling and imaging alkali metal atoms. The frequencies required for caesium are shown in Figure 5.1 and the detunings given in Table 5.1.

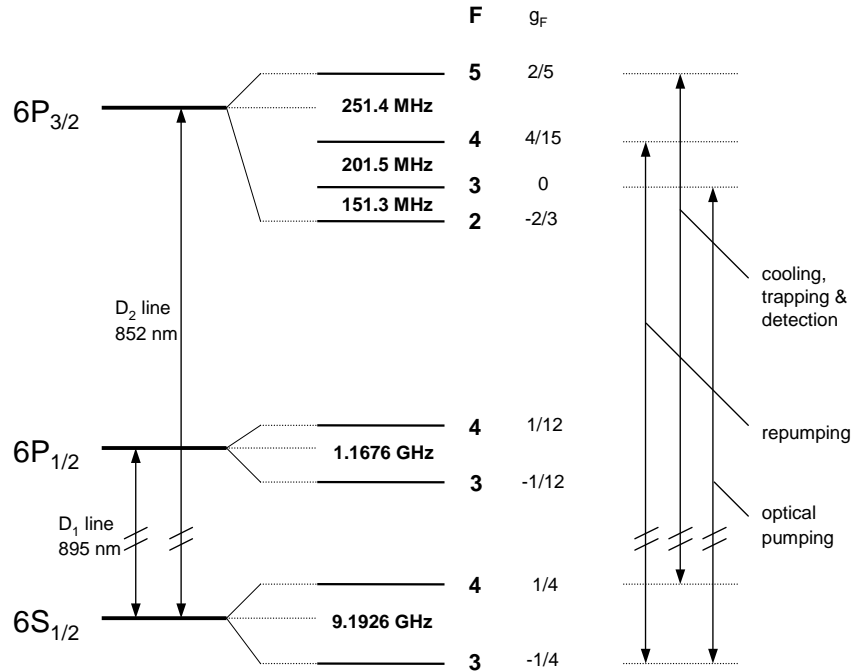


Figure 5.1: Hyperfine structure of ^{133}Cs in the ground state and first electronic excited states.

	Transition	Detuning (MHz)
MOT	$F = 4 \rightarrow F' = 5$	-7.2
CMOT	$F = 4 \rightarrow F' = 5$	-11.5
Molasses	$F = 4 \rightarrow F' = 5$	-64.2
Depumping	$F = 4 \rightarrow F' = 5$	-247.2
Probing	$F = 4 \rightarrow F' = 5$	0
Repumping	$F = 3 \rightarrow F' = 4$	0
Optical Pumping	$F = 3 \rightarrow F' = 3$	≈ 2

Table 5.1: The laser frequencies required for each stage of the experiment. The frequency of the depumping light is equivalent to a detuning of ≈ 4 MHz from the $F = 4 \rightarrow F' = 4$ transition. (It is quoted in the table as a detuning from the $F = 4 \rightarrow F' = 5$ transition as the light is derived from the MOT laser which is locked to this transition.)

To provide the light required for trapping, cooling and imaging, three semiconductor diode lasers and an amplifier chip at 852 nm were used:

1. MOT Laser: A SDL-5422-HI (150 mW) in an extended cavity with grating feedback. This laser was used to inject the tapered amplifier chip in a MOPA (master oscillator power amplifier) setup. The MOT laser provided the laser light not only for cooling and trapping, but also for depumping.
2. MOPA: A SDL-8630-E amplifier chip (500 mW). It provides light for the experimental MOT and the pyramidal MOT.
3. Repumping Laser: A SDL-5422-HI (150 mW) in an extended cavity with grating feedback. The optical setup of this laser is illustrated in Figure 5.2.
4. Probe Laser: A SDL-5412-HI (100 mW) in an extended cavity with grating feedback. This laser provides the light for probing and for optical pumping (see Section 5.1.2 for details).

The three grating-stabilized lasers mentioned above are in a Littrow configuration which produces laser light with a linewidth less than 1 MHz. However, the frequency of the laser light can drift in time due to temperature, current and mechanical drifts. We therefore servo-control the laser frequency to an external reference signal, usually either a Doppler-broadened lineshape or using a Doppler-free technique such as saturated absorption spectroscopy.

The most common method of stabilizing the diode laser frequency is by saturated absorption spectroscopy. In this method a few mW of the laser output light is used to generate two counter-propagating beams (pump and probe) passing through an atomic vapour cell. The laser light is frequency modulated by use of an acousto-optic modulator (AOM) or by modulating the laser current. The pump beam saturates the appropriate transition (when the frequency of the radiation is on resonance) and therefore the probe beam experiences less absorption. This leads to a peak in the absorption profile corresponding to a Lamb dip in the velocity distribution. The diode laser frequency is then locked to either the side

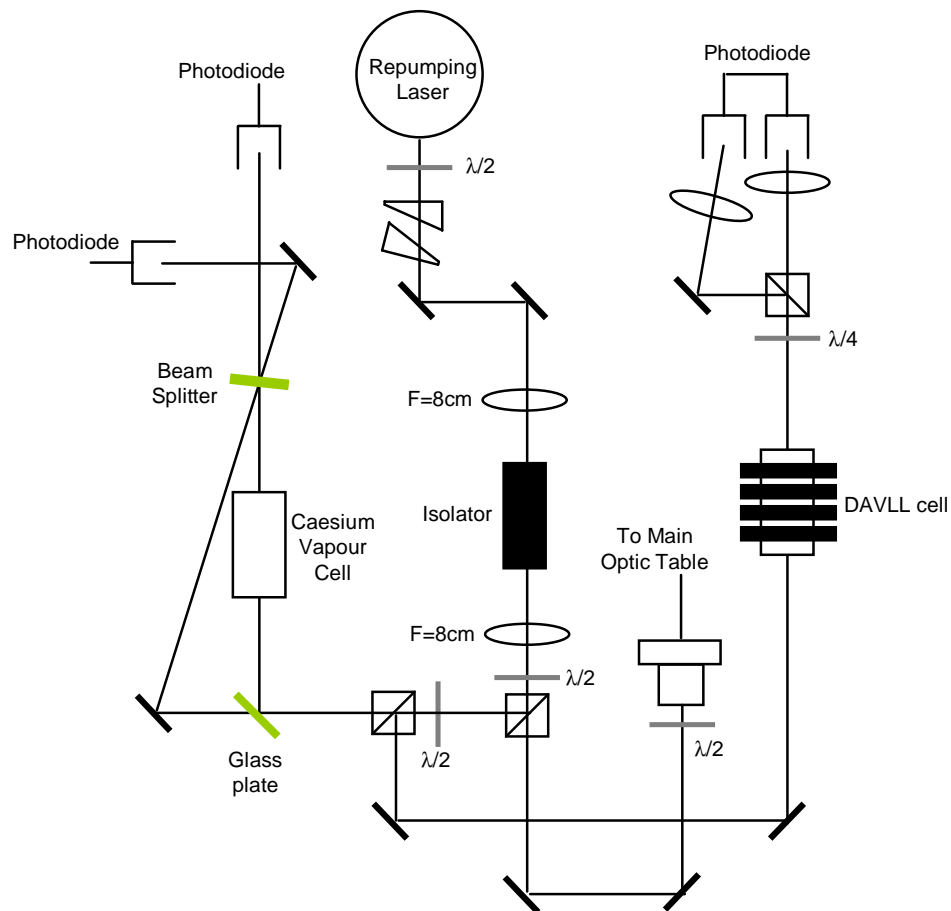


Figure 5.2: A schematic of the setup of the repumping laser. This diagram illustrates the optics required for both saturated absorption and DAVLL locking.

or the peak of the narrow saturated absorption feature [116, 117, 118]. However, there are some disadvantages in locking to a saturated absorption feature: the capture range is small (≈ 30 MHz); if the laser current is modulated, variations in the frequency and intensity occur; and the laser can only have a limited range of frequencies unless external frequency modulators (e.g. AOMs) are used. The majority of these disadvantages can be eliminated by using a different method of locking – the Dichroic Atomic Vapour Laser Lock (DAVLL) [119] which was developed at JILA.

5.1.2 Frequency Stabilization - DAVLL

An antisymmetric error signal is generated from the Doppler-broadened lineshape of an atomic transition using the Zeeman shift. The Doppler-broadened absorption feature is detected by passing a laser beam through an atomic vapour cell and observing the absorption while scanning the laser frequency across an electronic transition. The signal obtained is independent of the laser polarization (Figure 5.3 (a)). In the presence of a weak magnetic field the hyperfine levels are split into individual Zeeman components, and for circularly polarized light there is a difference in the absorption rates of the two Zeeman components. σ^+ polarized light drives $m_F = +1$ transitions, while σ^- polarized light drives $m_F = -1$ transitions. The top section of Figure 5.3 illustrates the origin of the difference in absorption rates. The antisymmetric DAVLL error signal (Figure 5.3 (d)) arises from the subtraction of the two different absorption profiles (Figure 5.3 (b) and (c)). The laser frequency can be locked to the zero crossing point of the DAVLL signal (Figure 5.3 (e)). At this point, in the absence of any offset voltage, the net photocurrent is zero.

In a saturated absorption locking setup it is only possible to lock to a saturated absorption feature (either the peak or side). However, the DAVLL locking point can be changed over several hundred MHz. The full width half maximum (FWHM) of the Doppler-broadened lineshape is given by the following equation:

$$\Delta\omega_D = \frac{2\omega_0}{c} \sqrt{\frac{2k_B T}{m}} \quad (5.1)$$

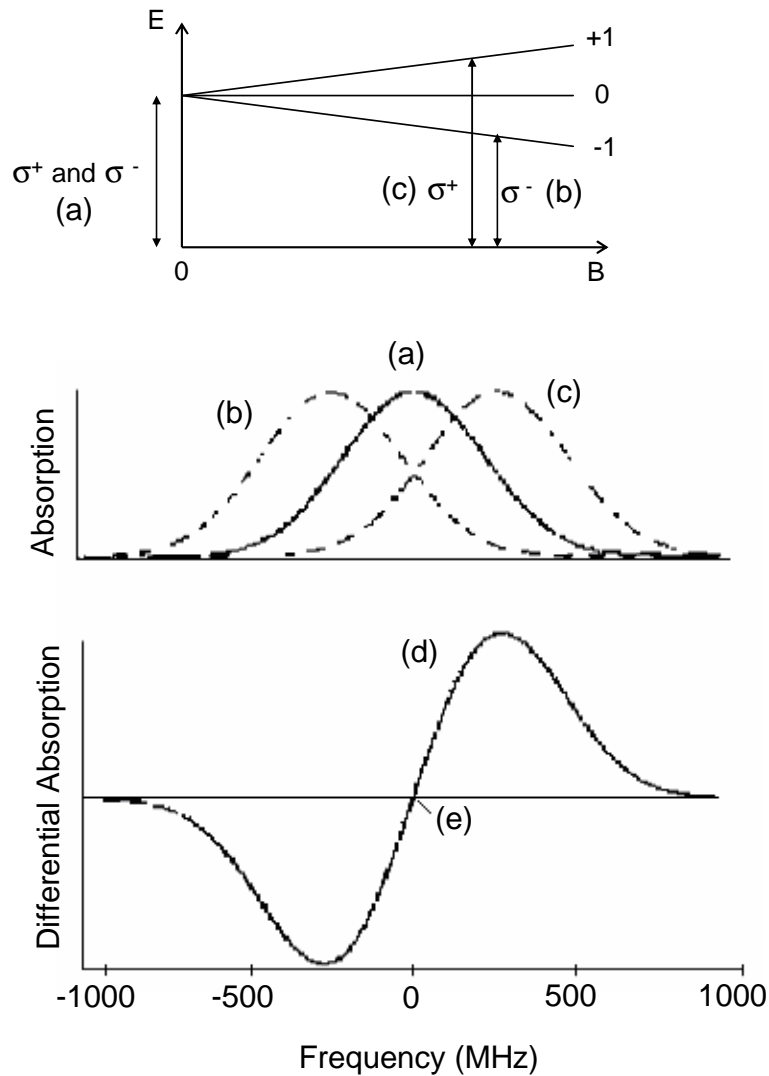


Figure 5.3: Origin of the DAVLL signal shape: (a) the signal obtained in the absence of a magnetic field, (b) and (c) the signal obtained in the presence of a magnetic field with σ^- and σ^+ polarized light respectively, (d) is the DAVLL signal obtained by subtraction of the two absorption profiles (b) and (c), (e) is the point at which the laser frequency is locked. (Figure modified from Reference [119].)

where ω_0 is the resonant frequency, T is the temperature of the atoms in the vapour cell, and m is the mass of a caesium atom.

For caesium at room temperature (300 K) the Doppler width is ≈ 450 MHz. This gives a broad locking signal which in turn makes the lock more robust. The locking point can be changed by two methods: electronically by summing in an external voltage to the bare DAVLL signal, or optically by rotating the quarter-wave plate (Figure 5.4). The latter method is preferable as then the lock point is always when the net photocurrent is zero. This means the laser frequency lock maintains its insensitivity to laser intensity fluctuations.

Experimental Setup

The magnetic field required is produced by positioning rings of permanently magnetic material concentrically around the glass cell containing the atomic vapour. The rings are separated with non-magnetic material and changing the spacing is used to adjust the magnitude of the magnetic field to the required value. The shape of the DAVLL signal is affected by the magnitude of the magnetic field. The larger the magnetic field the greater the separation between the two Zeeman-shifted absorption peaks (Figure 5.3 (b) and (c)) and the larger the capture range. The quality of the lock however, depends on the magnitude of the slope of the DAVLL signal at the locking point. A DAVLL signal with a steep slope makes the laser frequency lock less sensitive to noise that mimics laser frequency changes. Another factor relating to the magnetic field is that the Zeeman-shifted absorption peaks broaden with increasing magnetic field. Selecting the magnitude of the magnetic field is therefore a compromise between the size of the capture range, broadening of the Zeeman-shifted absorption profile peaks and the magnitude of the DAVLL signal slope. Corwin *et al.* [119] determined that the optimum magnetic field value is 100 G for $^{85}\text{Rb}/^{87}\text{Rb}$. For Cs the optimum value was found to be approximately 180 G. Changes in the magnetic field of up to a factor of two should not significantly alter the lock performance as the shape of the DAVLL signal does not depend strongly on the magnitude of the magnetic field.

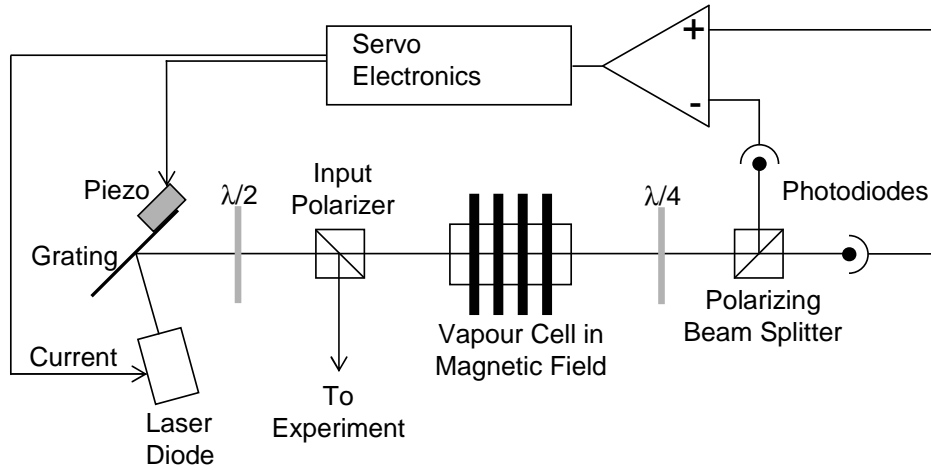


Figure 5.4: Schematic of a DAVLL scheme. (Figure modified from Figure 1 in Reference [119].)

The DAVLL signal can be obtained by subtracting the outputs from two separate photodiodes (as shown in Figure 5.4). It is better, however, to incorporate two photodiodes into a circuit that subtracts their two outputs. The circuit diagram for this arrangement is given in Figure 5.5.

Locking Electronics

There are two components to the locking electronics – the DAVLL input board and the integrator board (see Table B.1, Appendix B for details). The input board contains three inputs: the DAVLL signal (the bare DAVLL signal from the photodiode), an external voltage (allows external control of the detuning e.g. during molasses) and an internal reference voltage set by a potentiometer (to set the locking point accurately). Figure 5.6 illustrates the setup of the DAVLL input board. The output of the DAVLL input board forms the input to the integrator board. The integrator board produces the correcting signals to the piezo and current which enables the locking of the laser frequency. The piezo operates to vary the frequency over a much bigger range than the variation that can be obtained with current control, but the speed of operation of the piezo system is limited by mechanical time constants to the order of a kHz. The current control is much

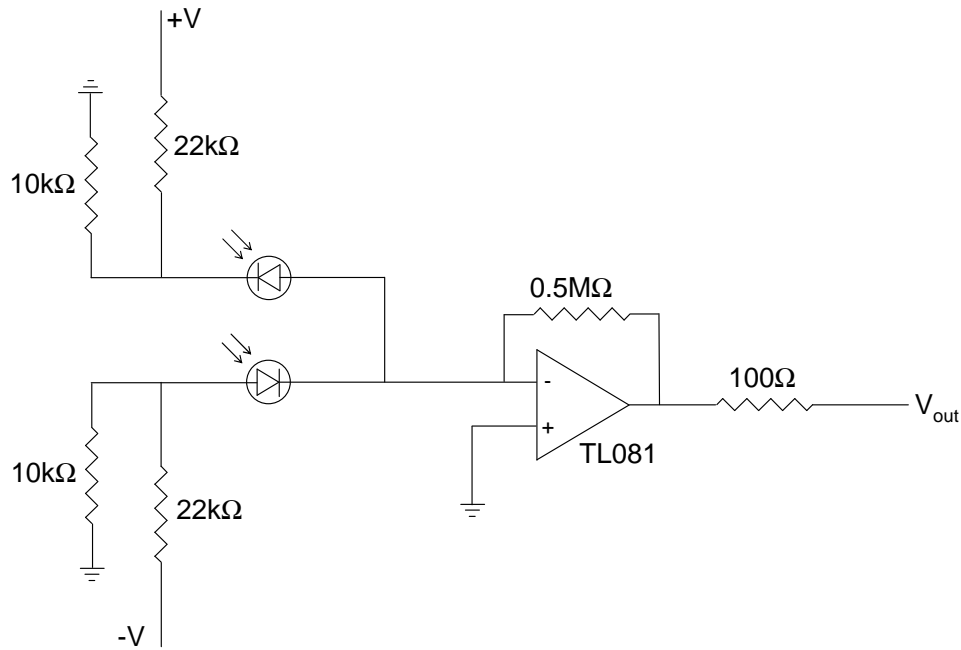


Figure 5.5: Diagram of the double photodiode (BPX65) circuit. The basic circuit is a current-to-voltage converter. The difference in the two photocurrents is converted into a voltage by the operational amplifier (TL081).

faster and therefore it can be used to reduce noise over a wider band than could be attained with only a piezo. The piezo operates to take out the effects of slower drifts and the effects of vibration, whereas the current lock is used to compensate for higher frequency noise. The changeover frequency between the current and piezo lock depends on the response time of the piezo.

There are many advantages in using the DAVLL system, rather than saturated absorption, to lock the laser frequency:

- It is compact and simple to set up – it requires very few optics and simpler electronics.
- It requires less laser power to lock.
- It has a large recapture range therefore the laser frequency stays locked for much longer periods of time.
- There is no need for modulation of the laser current.

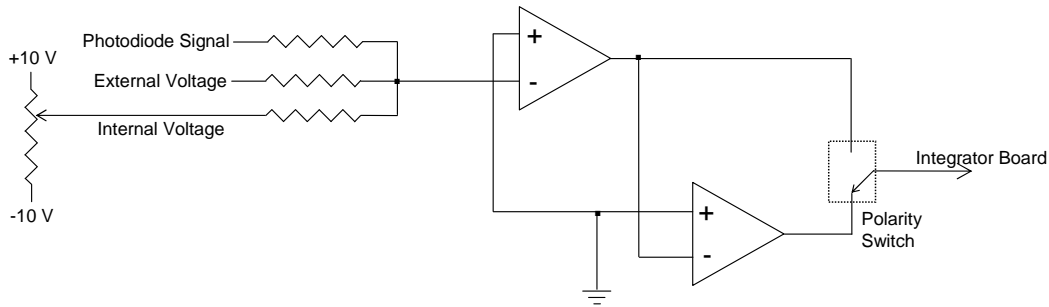


Figure 5.6: A schematic of the DAVLL input board illustrating the three inputs and the output, and the general flow of the circuit.

- Large frequency changes are possible by applying an external voltage (as explained previously). This is a significant advantage, not only in cost, but the use of an AOM in a double-pass configuration leads to at least a 50% reduction in laser power.¹

One disadvantage of the DAVLL scheme of locking the laser frequency is that it is impossible (without extra apparatus) to observe variations in the detuning frequency. One method of overcoming this disadvantage is to use a saturated absorption setup for comparison (see Figure 5.2 for an example of a laser setup incorporating both DAVLL and saturated absorption setups). The laser frequency is locked using the DAVLL signal and the point at which it is locked is set to be on the peak of a saturated absorption feature. The laser frequency is therefore locked using the DAVLL scheme, but with the ability to maintain close observation of the laser detuning. This is important as laser detuning has a large effect on experimental reproducibility. The DAVLL signal is also calibrated using the saturated absorption signal. By noting the position at which each Lamb dip in the saturated absorption signal occurs as a function of DAVLL detuning voltage, a curve is generated which gives the relationship between the DAVLL detuning voltage and the absolute detuning in MHz.²

¹For large frequency changes an AOM must be used in a double-pass configuration.

²When the DAVLL signal is linear across all of the saturated absorption peaks the detuning (in MHz) is directly proportional to the detuning voltage.

Experimental Setup

The DAVLL scheme has been used to lock the frequencies of all three external cavity diode lasers (ECDL) on the experiment for the last three years. One important point that should be noted is that the quality of the laser frequency lock seemed to depend largely on the quality of the laser mode.

During the experiment's day-to-day running the lasers rarely jumped out of lock. When they did, it could normally be attributed to the laser jumping to a different mode of the laser chip. Normal mechanical noise (e.g. tapping the optic table) and high frequency noise (e.g. pulsed copper vapour laser operation in the room directly above the laboratory) did not seem to have an effect on the lock.

Due to the effect a slight change in detuning can have on experimental reproducibility, the detuning of each laser was carefully monitored. The detuning of the MOT laser could drift significantly over the course of the day. This was attributed to the poor mode structure of the laser. The probe and the repumping laser detunings were checked approximately every 20 minutes.

Probe Laser

As mentioned previously the probe laser light is used not only for probing but also for optical pumping. The laser must therefore be jumped from the $F = 4 \rightarrow F'$ transition to the $F = 3 \rightarrow F'$ transition. Initially the laser frequency is locked to the $F = 4 \rightarrow F' = 5 : F = 4 \rightarrow F' = 4$ cross-over transition.³ The laser is unlocked by applying a low TTL signal to the gate input of the integrator board. The current and the PZT values are changed to the appropriate values for the $F = 3 \rightarrow F'$ transition by applying voltages to the current and PZT feed forward inputs on the integrator board. The detuning of the laser frequency is also changed by applying a voltage to the external voltage input on the DAVLL input board. The laser frequency is then locked to the new frequency by applying a high TTL signal to the gate input of the integrator board. This process is carried out before

³The AOM frequency is set to be 125.7MHz, bringing the frequency of the laser radiation incident on the atoms to the frequency of the cycling transition.

the optical pumping and then the reverse process (re-locking the laser frequency to the cooling transition) is carried out after loading the magnetic trap.

5.1.3 The Optical Table

The main optical table was divided into two sections: the laser section and the experimental section.

The laser section consisted of most of the equipment required to produce the frequencies required for cooling, trapping, and probing of the atoms. Figure 5.7 is a schematic of the laser section. The repumping laser and its optical setup (Figure 5.2) was situated on another smaller optical table. The light from this table was coupled down an optical fibre and the fibre end was situated on the main optical table to allow for coupling of the repumping and MOT light on a beam-splitter cube.

The probe laser is situated on the upper half of the optical table (Figure 5.7), and all the optics required for locking of the laser frequency is illustrated. An extra saturated absorption optical setup after the AOM permits the observation of the detuning of the laser light after the AOM and prior to coupling the light down the fibre.

The light from the MOPA is divided into two using a half-wave plate. This half-wave plate is used to set the powers on the pyramid and the experimental MOT. Each beam then passes through an AOM. Both AOMs are required to permit separate modification of the pyramidal MOT and experimental MOT light detuning as both beams are derived from the same laser (Master). Each beam is then coupled with the repumping light on a beam-splitter cube, and then coupled down an optical fibre. The optical fibres are then passed through a small hole into the experimental section of the optical table. The experimental section was enclosed in a light-tight box to prevent scattered light from reaching the atoms. The experimental setup is illustrated in Figure 5.8.

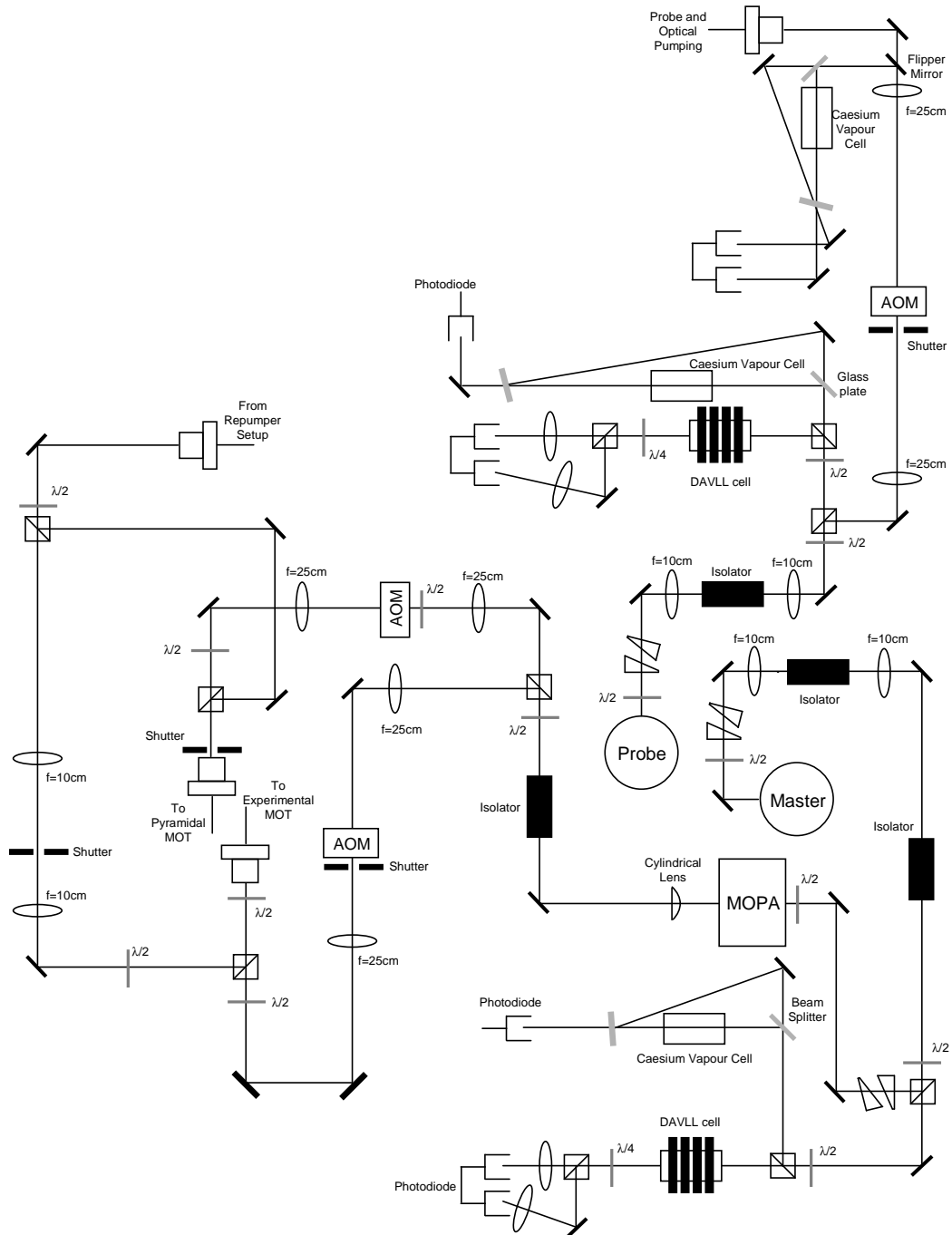


Figure 5.7: A schematic of the laser table.

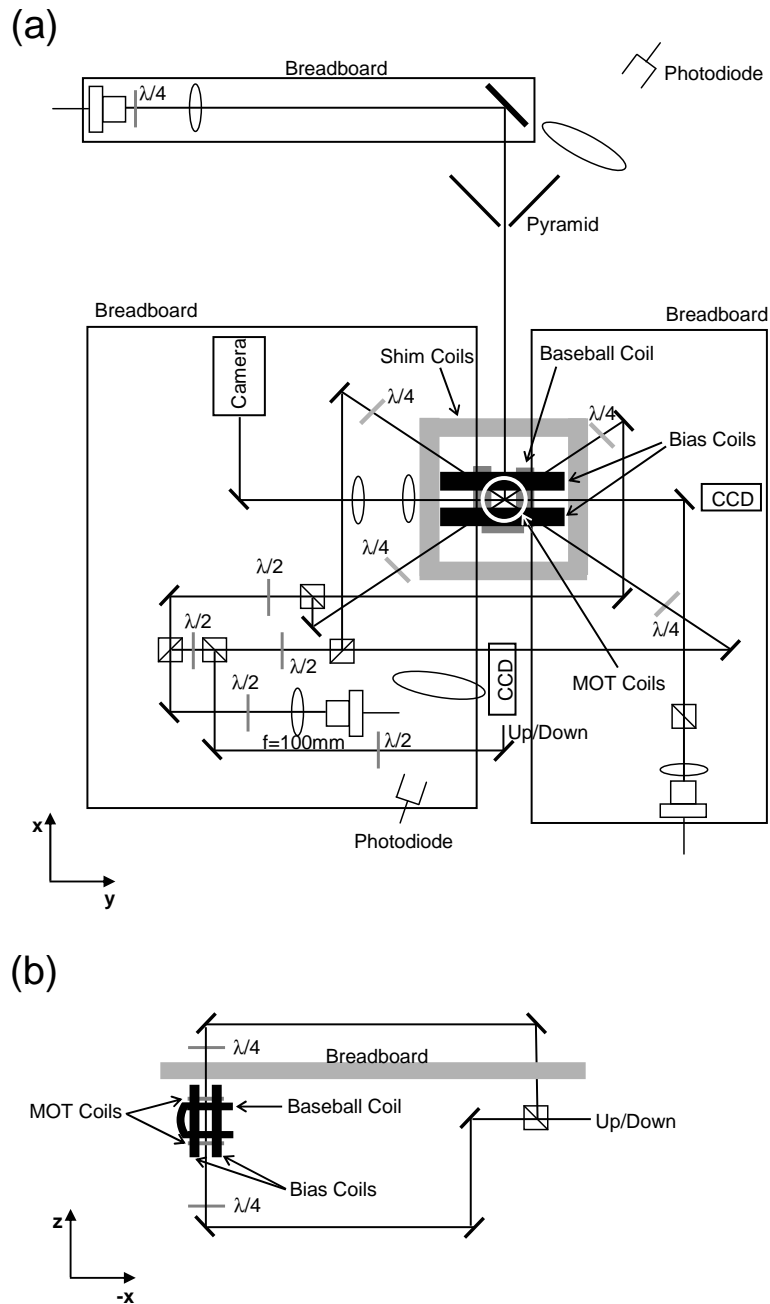


Figure 5.8: Schematic of the experimental optical table: (a) view from above, (b) view from the side to illustrate the path of the up/down beam.

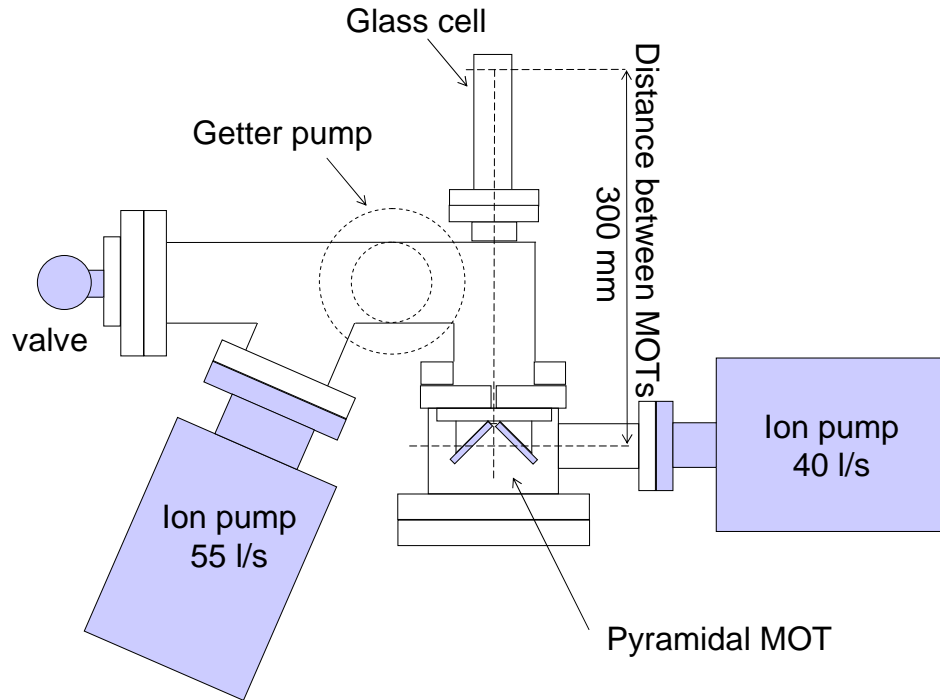


Figure 5.9: An illustration of the vacuum system.

5.1.4 Vacuum System

The vacuum system shown in Figure 5.9 can be discussed in two parts.

The first section of the vacuum system contains the pyramidal MOT. It has a pressure of approximately 10^{-9} mbar maintained by a 40 l/s ion pump (Varian VacIon Plus 40). The caesium source is several dispensers (SAES Getters) connected in series located just above the pyramid mirrors. A current is passed through the dispensers, generating heat and the resulting chemical reaction releases caesium atoms. The dispenser is continually operated at 3.2 A to provide ample Cs pressure in the pyramidal region.

Differential pumping is achieved by a hole (5 mm diameter, 17 mm long) in the back port of the first chamber. The distance between the pyramidal MOT and the experimental MOT is 30 cm. This distance is short in order to reduce atom loss due to divergence of the atomic beam from the pyramidal MOT to the experimental MOT.

The second section of the vacuum system contains a rectangular quartz cell of dimensions $28 \times 28 \times 80 \text{ mm}^3$ (2 mm wall thickness). Pressure in this region is maintained by a 551/s ion pump (Varian VacIon Plus 55) and a non-evaporable getter (NEG) pump (SAES CapaciTorr-CF35, Cartridge C-400-DSK-St172). The NEG pump should preserve a very low pressure in the experimental cell for long term operation.

5.1.5 Pyramidal MOT

The purpose of the pyramidal MOT [72] is to collect atoms from a vapour of caesium. The atoms are transferred continuously through the differential pumping hole into an ultra-high vacuum region, where the final experiments are performed. Our pyramid (Figure 5.10) is larger than the one described in Reference [74]. This is an improvement as an increase in the size of the pyramidal mirrors increases the volume of the collection region, which results in a higher flux atomic beam.

Experimental Setup

The pyramidal MOT experimental apparatus can be divided into two distinct parts: the optical arrangement and the generation of the magnetic fields required.

The optical setup is straightforward (see Figure 5.11). The large mirror (diameter = 100 mm) and the pyramidal mirrors (base length = 60 mm) are coated by C. Goodwin in the Oxford physics department. The mirror and pyramid optics are coated to achieve the same reflectivity for s- and p-polarization.⁴ The beam size required is approximately 60 mm therefore a single lens (f=250 mm) after the bare fibre end provides both the magnification and collimation. The initial reason for using a fibre was because of the poor beam quality of the MOPA. However, an added advantage was soon realised. When the pyramid was first set up, the pyramidal light was derived from a single laser (with no fibre). Because of the long path length from the laser to the pyramidal mirror, any slight changes in the angle of the grating of the ECDL caused a large deviation in the incident position

⁴Non-equal reflectivity between s- and p-polarization causes a phase shift between the two polarizations and therefore the light is no longer circularly polarized.

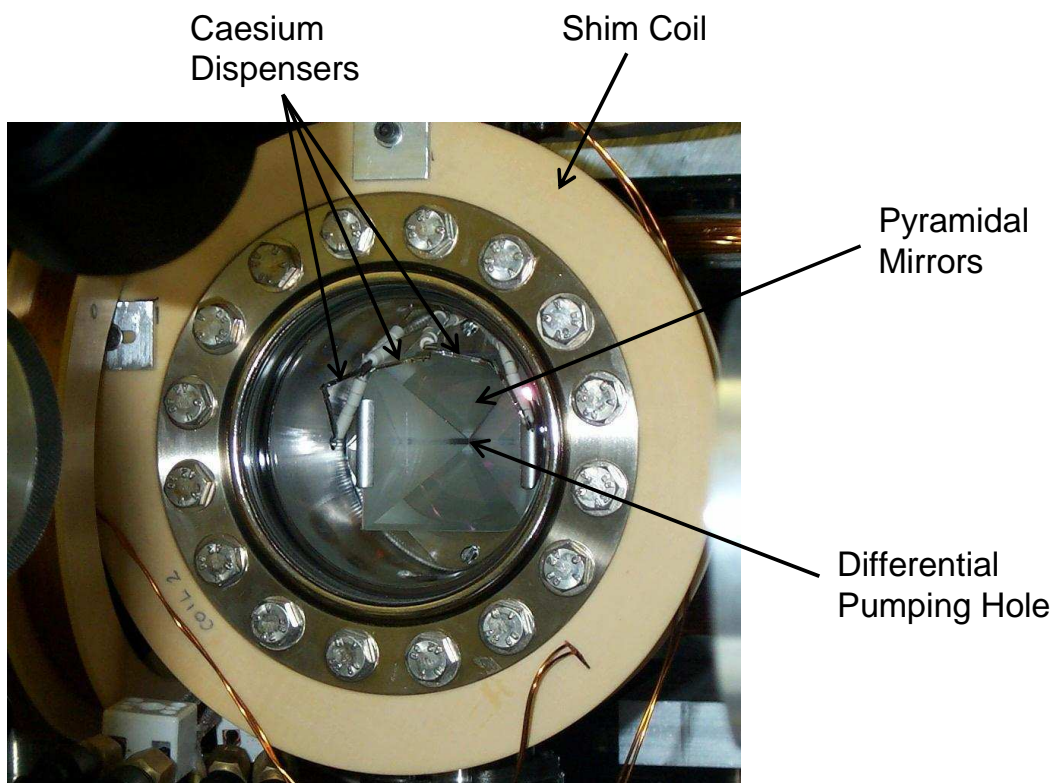


Figure 5.10: A photo of the pyramid.

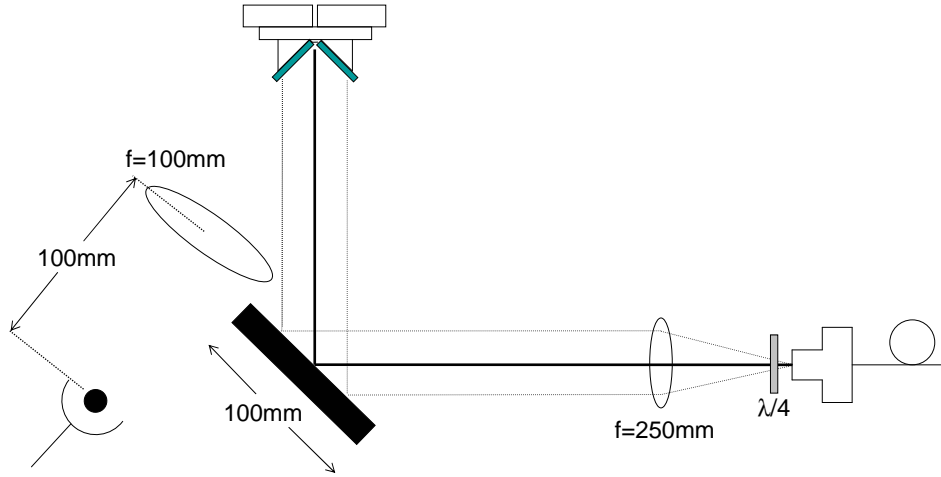


Figure 5.11: A diagram of the optical setup of the pyramidal MOT.

of the beam on the pyramidal mirrors. This caused a drastic change in the loading performance of the pyramid and meant that it was necessary to adjust the large pyramid mirror every day. Once the MOPA was set up and the fibre implemented, the beam angle was carefully set up and the shim coil settings optimized. Over the course of the last two years the pyramidal experimental parameters (e.g. beam angle, quad-coil current, shim coil settings) have not been changed. Every morning the only optimizations that were carried out on the pyramid were: optimizing the transmission of the pyramid light through the fibre, and a slight adjustment of the quarter-wave plate to compensate for drifts in the output polarization of the optical fibre. The optimum position of the wave plate was decided by optimizing the load of atoms into the experimental MOT or by looking at the quality of the pyramidal or experimental MOT using an infrared camera.

Two sets of coils are required for generation of the magnetic fields required: a pair of anti-Helmholtz coils (pyramid quad-coils), and three shim coils (pyramid shim coils) positioned in orthogonal directions.

The anti-Helmholtz coils provide the field gradient required for confinement of the atoms. They are made out of 15 turns of 3mm outer diameter 22 swg (corresponding to an inner diameter of approximately 1.5 mm) annealed copper tubing. Water is passed through the copper tubing to provide cooling. The radius

of the coils is 56 mm and their separation is 50 mm. To load the atoms 18 A is run through the coils producing a field gradient of 9.22 G cm^{-1} (Equation 2.8). The total resistance of the pyramid quad-coils (in series) and the connecting cables is approximately 0.08Ω .

The shim coils are circular coils, inner diameter of approximately 150 mm, wound out of 1 mm (100 turns) enamelled copper wire. There are two purposes for the 3 shim coils: firstly any ambient magnetic fields (e.g. earth's magnetic field) need to be nulled out, and secondly they are required to move the centre of the magnetic field produced by the quad coils for diagnostic purposes. In order to determine the number of atoms in the pyramid accurately, it is necessary to move the centre of the MOT to a position where the fluorescence can be measured. Normally the centre of the MOT is over the pyramid hole and therefore no fluorescence is observed. The voltage level circuit (Section 5.2.2) provides the voltages for the two settings required – one for loading the experimental MOT and the reference setting for determining the atom number in the pyramid.

5.1.6 2nd MOT – Experimental MOT

For this experiment the 2nd MOT is a conventional six-beam MOT [58].

The MOT quad coils are circular coils of diameter 50 mm separated by a distance of 70 mm. Each coil is made out of 80 turns of 1 mm enamelled copper wire. The wire is wound onto a water-cooled former as in the absence of water-cooling the temperature of the coils reaches 100°C within 5 minutes. The coils are positioned as close as possible to the trapping region as the amount of current required to produce a given gradient is proportional to the separation of the coils to the fourth power ($I \propto s^4$). Figure 5.12 illustrates the position of the MOT quad coils. To load the experimental MOT 2.26 A is run through the quad coils. This generates a field gradient of 10.2 G cm^{-1} (Equation 2.8). The current through the coils is controlled by a FET and the gate voltage for the FET is provided by the multiplexer circuit (see Section 5.2.2).

Shim coils are required to null out any ambient fields, which is especially im-

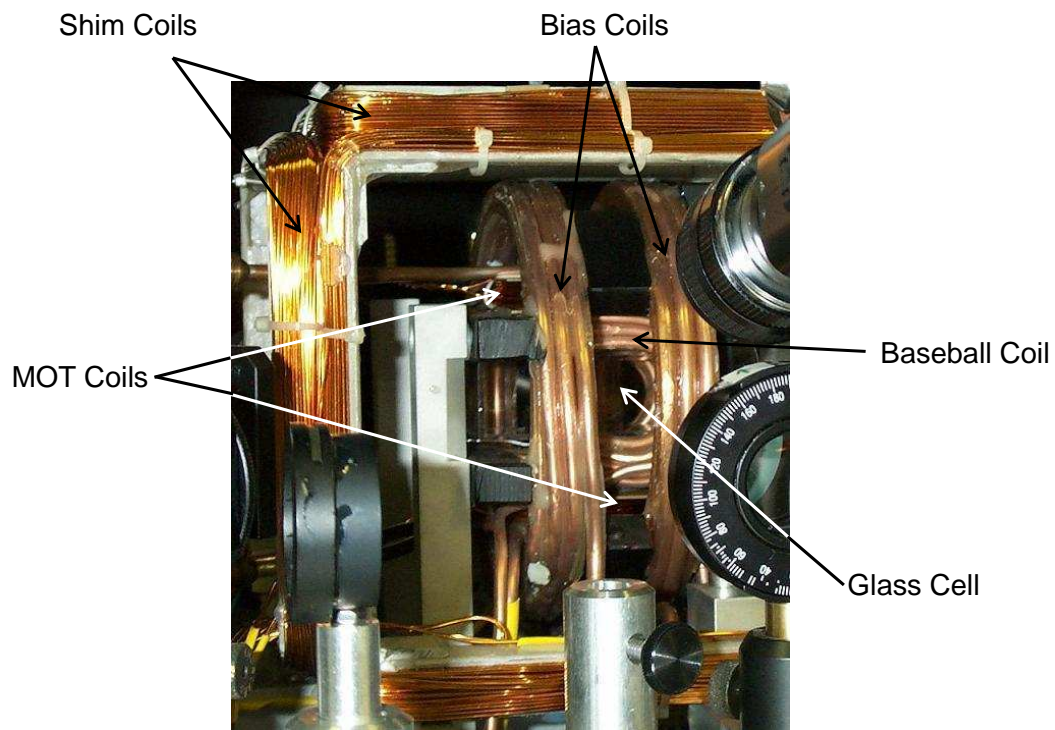


Figure 5.12: A photo of the experimental MOT. The baseball coil surrounds the glass cell. The MOT coils are positioned between the baseball coil and the bias coils.

portant in the optical molasses stage of the experiment, and to move the centre of the MOT for loading into the magnetic trap. The shim coils are six rectangular coils mounted in a cuboid arrangement. The lengths of the side are approximately 164 mm and the separation between the coils is approximately 90 mm (taking into account the thickness of the windings). Each coil consists of 50 turns of 1 mm enamelled copper wire. The y - z direction shim coil is also used to produce the quantization field for probing and optical pumping. The magnitude of the quantization field is approximately 3 G.

The optics for the experimental MOT is illustrated in Figure 5.8. It is possible to generate the three pairs of orthogonal counter-propagating beams required by retro-reflecting three individual beams. However, because of the optical absorption of the cloud, this method introduces a power imbalance between each counter-propagating beam. This problem is avoided by using six separate beams.

5.1.7 Magnetic Trap

The magnetic trap used in the experiment is a baseball trap (Section 2.4.5, Chapter 2). This type of trap was chosen because it is possible to attain high magnetic fields and weak trapping potentials simultaneously. The baseball coil is capable of generating axial and radial confinement. However, a pair of Helmholtz coils (called bias coils) were added in order to permit modification of the trapping geometry. The bias coils can either be set up to add to or oppose the axial magnetic field generated by the baseball coil. When they are set up to oppose they produce tight radial confinement at low fields, whereas for addition they provide the ability of operating at high magnetic fields (over 500 G). Figure 5.13 is a photo of the baseball and bias coils.

The baseball coil is constructed using 1/8" outside diameter 22 swg (corresponding to an inner diameter of approximately 1.5 mm) annealed copper refrigeration tubing. The bias coils are constructed out of 3/16" 20 swg (corresponding to an inner diameter of approximately 3 mm) annealed copper refrigeration tubing. The baseball and bias coils both consist of 9 turns. Before winding the coils, the



Figure 5.13: A photo of the baseball and bias coils.

copper tubing is encased in heatshrink to insulate the turns. During the winding, all the voids between the layers of copper tubing are filled with epoxy to improve mechanical stability.

The hollow tubing allows for water cooling of the coils, which is necessary as high currents (up to 500 A) generate a significant amount of heat. Thermistors are glued to the baseball and bias coils and are connected to the temperature interlock facility of the high current power supply. If the temperature exceeds the preset temperature (set by a potentiometer), the circuit trips, turning off the current.

Control Electronics

The magnetic trap current is controlled by two pairs of electronic circuits – a ‘Reference Voltage Board’ and ‘Main Feedback Board’ (see Figure 5.14). The ‘Reference Voltage Board’ controls the trap turn on/off (and fast input control etc) and generates the input voltage for the ‘Main Feedback Board’. The ‘Main Feedback Board’ provides the gate voltage for the FET’s and the integrator part of the circuit regulates the current through the baseball and bias coils.

The ‘Trap on/off TTL’⁵ is controlled by a TTL signal. When the TTL signal

⁵In the following section, all signal names in inverted commas refer to the corresponding

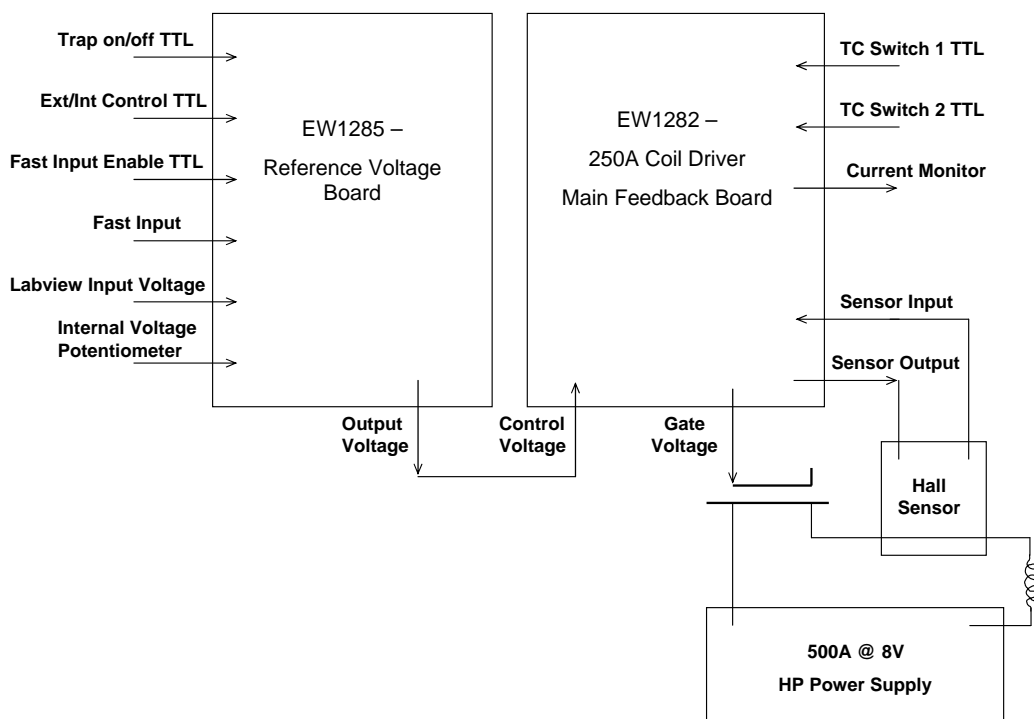


Figure 5.14: A schematic illustrating the setup of the magnetic trap current control electronics. (To control the current in both the bias and baseball coils two pairs of the above boards are required.)

is set to high, the trap turns on to a level set by the analogue ‘Labview Input Voltage’. For a rapid turn on the trap is turned on with the servo capacitors switched out of the circuit. The capacitors are then switched back into the circuit to improve DC stability.

For fast current control the fast input facility can be used. The ‘Fast Input Enable TTL’ requires a TTL signal in order to switch an extra reference voltage into the circuit. The extra reference voltage is an analogue voltage applied to the ‘Fast Input’, and is then summed into the circuit. This facility is required as the analogue input from Labview is filtered (the ‘fast input’ is summed into the circuit after the filter) and therefore fast current changes cannot be implemented.

The magnetic field stability depends partly on the stability of the analogue outputs of the computer board. The ‘Labview Input Voltage’ can be switched down by a factor of a 100 using the ‘Ext/Int Control TTL’. Simultaneously the stable reference source can be switched in. This stable reference source is produced on the ‘Reference Voltage Board’ by a series of resistors and a potentiometer for small adjustments. During the life of the experiment this feature has been used sparingly. There has not been a reason to believe that any possible noise from the computer board was having a detrimental effect on the experimental results.

The ‘Main Feedback Board’ generates the gate voltage for the FETs. The FETs that are used on the experiment are capable of running 200 A each. There are 10 FETs in total – 5 for the bias coils and 5 for the baseball coil. The current source is a Agilent power supply (Agilent 6681A) capable of running 500 A at 8 V. Welding cable is used to carry the current from the power supply to the coils.

For current stabilization the welding cable is passed through two closed loop current sensors (one for each coil). The ‘Main Feedback Board’ generates and controls the current in the Hall sensor. It produces a magnetic field that cancels the magnetic field due to the current flowing through the welding cable. Any changes in the current are observed by converting the current flowing through the Hall sensor into a voltage. The voltage is measured using a 6 d.p. precision DVM

input/output in Figure 5.14

(Agilent 34401A – 6 1/2 Digit Multimeter). Therefore field fluctuations of the order of a few mG can be observed. This voltage is also used as an error signal to regulate the current through the coils.

For normal running of the experiment the current in the baseball coil, ≈ 230 Amps, is turned on in under $400 \mu\text{s}$ to give a magnetic field value of ≈ 139 Gauss at the centre of the trapping potential. This results in trap frequencies of 12 Hz radially and 5 Hz axially.

Classical Motion of Atoms in a Magnetic Trap

In a purely parabolic potential, with no collisions between atoms, atoms undergo simple harmonic motion in each orthogonal direction. However, it is experimentally impossible to construct a magnetic trap where the potential is purely parabolic. There exist cross-terms in the potential equation which break the separability of the three spatial dimensions, and in turn cause the orbits of the atoms to slowly precess. This leads to a mixing of energy between spatial directions.

There are two main problems which can result upon loading of the magnetic trap: sloshing and breathing.

Sloshing is the motion of the centre of mass of the cloud that occurs when the atoms are not loaded into the centre of the trapping potential, or if the cloud is loaded into the magnetic trap with some velocity. Atoms at different points in the cloud will therefore have different amplitudes of oscillations, and in a harmonic trap, the cloud will undergo simple harmonic motion about the minimum of the magnetic trapping potential. Anharmonic terms in the trapping potential will cause the cloud to spread out over the region in which it was sloshing. As the width of the cloud is greater, it appears that the temperature of the cloud has increased. The magnitude of the sloshing can be reduced by better matching of the MOT and magnetic trap centres by use of the shim coils during the CMOT stage. Figure 5.15 illustrates the sloshing in the axial and radial directions. Sloshing can be used to determine the trapping frequencies, as described in Section 5.4.6.

After loading the magnetic trap, if the shape of the MOT does not match the

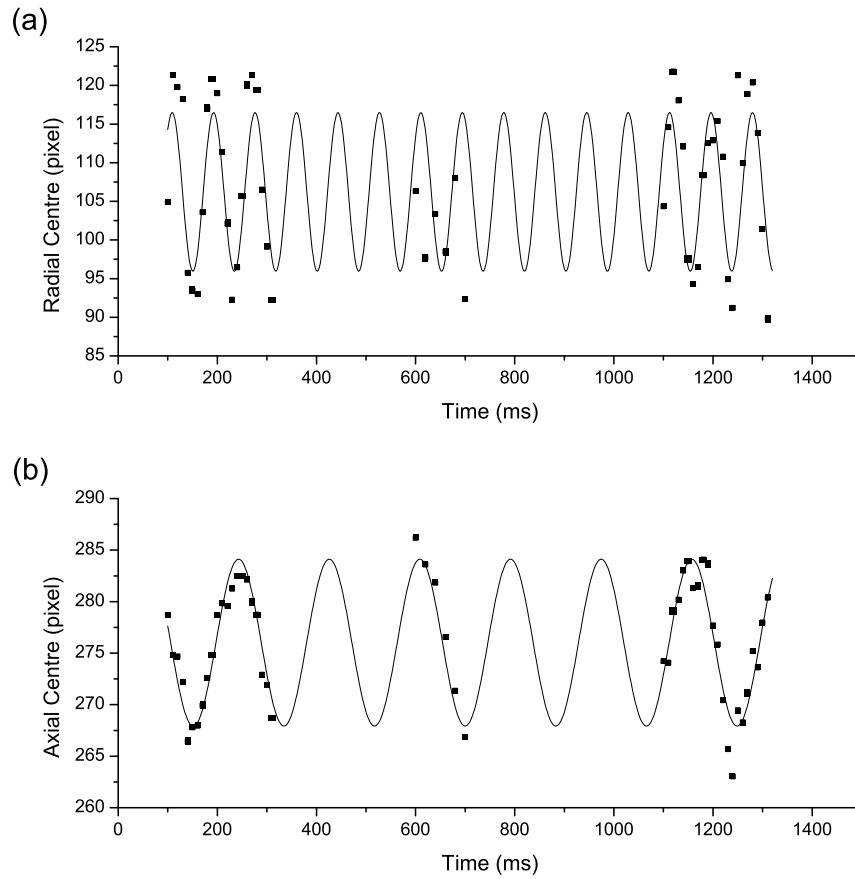


Figure 5.15: Observation of the sloshing in the axial and radial directions. Each point represents a single measurement (both radial and axial position) of the centre of mass of the cloud, while it sloshes in the trap.

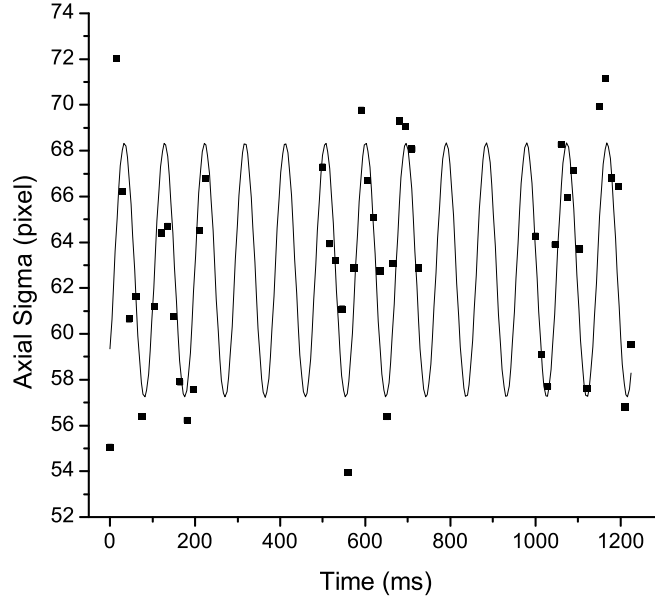


Figure 5.16: Observation of the axial breathing mode in the magnetic trap. The frequency of the breathing motion is approximately 10.6 Hz, which corresponds to an axial trap frequency of 5.3 Hz.

shape of the MT contours then the initial potential and kinetic energy will not be in equilibrium. This leads to an excitation of the breathing mode. The width of the cloud will oscillate, leading again to an increase in the temperature of the cloud. The breathing mode frequency is twice the trap frequency (due to the symmetry of the trapping potential). To reduce the likelihood of exciting the breathing modes, the parameters of the molasses stage are adjusted in order to match the shape of the cloud to the magnetic potentials. Figure 5.16 is a graph illustrating the breathing mode of the atom cloud in the magnetic trap.

The six MOT laser beams on the experiment are not aligned perfectly orthogonal (due to optical access constraints). The cloud is therefore not spherical and is slightly elongated in the x - direction. This coincides with the shape of the magnetic field contours in the same direction. (Figure 2.11 shows that the magnetic field contours are elongated in the x - direction.)

5.1.8 Evaporation

The radio-frequencies required for evaporation were generated by a frequency generator (Agilent E4400B). The signal is amplified by a Minicircuits amplifier (ZHL-5W-1 for 40 dB gain) and is transmitted to the atoms via a two-turn coil. A $10\ \Omega$ resistor was placed in series with the coil to impedance match the load to the source. This should reduce amplitude changes over the range of frequencies used. The evaporation ramps were calculated in Labview and then transferred continuously to the frequency generator via GPIB interface.

5.2 Control

When setting up an experiment a choice has to be made between an analogue or a digital basis for experimental synchronization. The difference between both approaches is: in the analogue setup the computer generates the analogue voltages and therefore external electronics (e.g. Schmitt triggers) are required to synchronize the equipment; whereas in the digital setup the computer generates the TTL signals required to synchronize the equipment, and external electronics are required to produce the analogue voltages.

The advantages of the digital philosophy is that TTL signals have a high fidelity and therefore there is no degradation of the signal along long BNC cables. It is straightforward to implement as there is no timing issues with TTL signals. Experiments based on the digital philosophy are very easy to run on a day-to-day basis as unknown experimental problems are simpler to solve when each section of the experiment can be disassociated from other sections.

5.2.1 Experimental Synchronization

This experiment was built using the digital philosophy. The experiment was synchronized using a Labview control program connected to the experiment with two data acquisition boards (a digital and an analogue board) and a GPIB board (see Appendix B). Two analogue outputs are used: ‘Labview Input Voltage’ for the

bias and baseball coil (Figure 5.14).

Labview

One of the advantages of using the Labview program to control the experiment is its user-friendly interface. The control program was written [120] by first setting up the correct experimental timing structure as in Figure 5.17. The timing delays (e.g. shutter delays, quad current turn on time etc) are then entered into a table which is incorporated into the program with the use of equation boxes. This means that any subsequent modifications in the timings does not involve a restructuring of the program.

5.2.2 Analogue Voltages

The digitization of the experiment does mean that other methods of generating the analogue voltages are required. A multiplexer circuit and a voltage switching circuit (see Table B.1, Appendix B) are used to generate analogue voltages. They both work on the same principle – applying a TTL signal switches between two analogue voltages (range -10 to 10 V). The voltages required are set using panel-mounted potentiometers. The multiplexer circuit uses two input TTL signals to switch between four analogue voltages. This circuit is used for the experimental MOT quad and shim coil voltages and the MOT laser detuning settings – each of which require 4 different experimental settings (i.e. for loading the MOT, CMOT, molasses and optical pumping). The voltage switching circuit (one TTL signal) is used for the pyramid quad and shim coils and the probe detuning, current and PZT feed forward values.

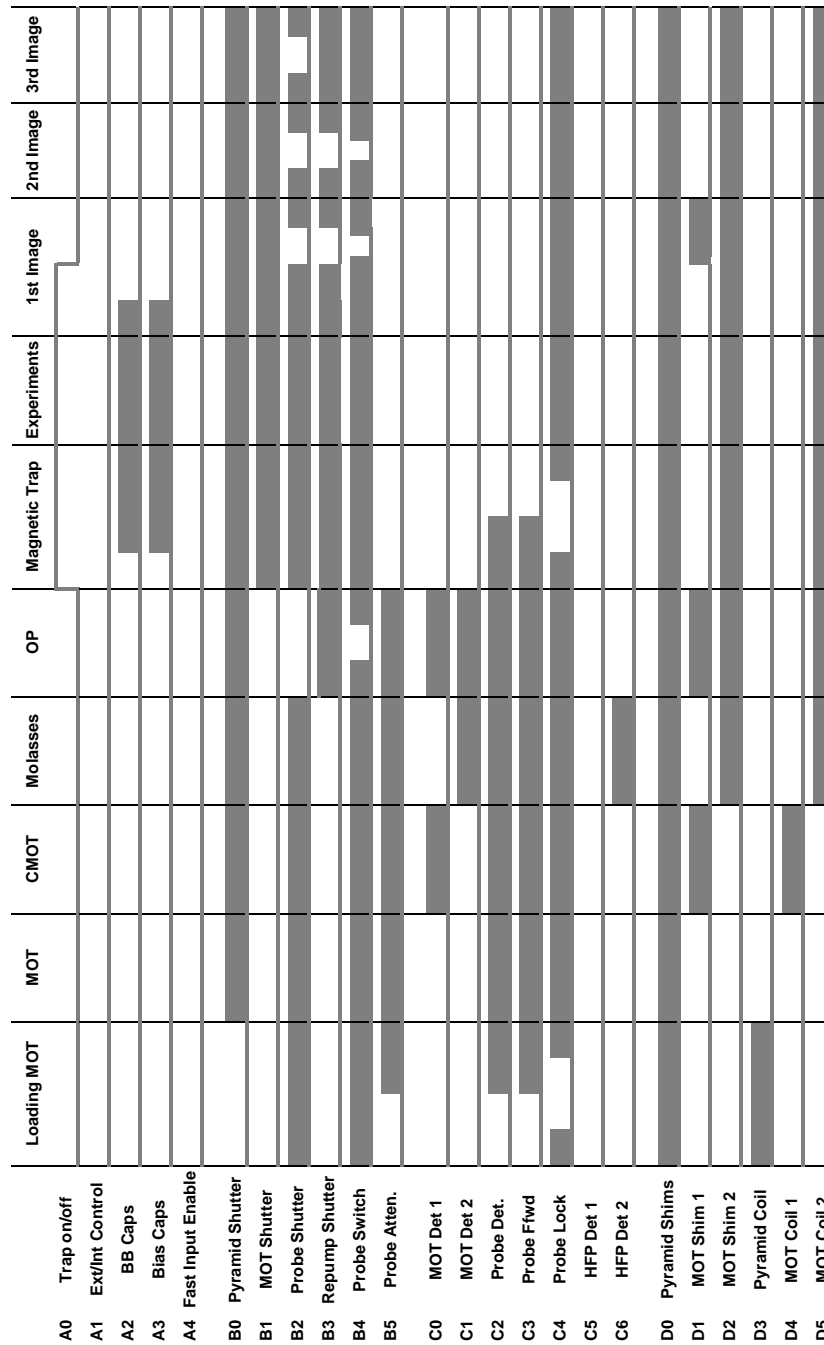


Figure 5.17: Idealized timing diagram. A grey line / grey box indicate a low / high level TTL signal. The logic state of the experiment at a particular time can be clearly observed by reading down the columns e.g. for the CMOT the digital signals are 0 0 0 0 0 1 0 1 etc.

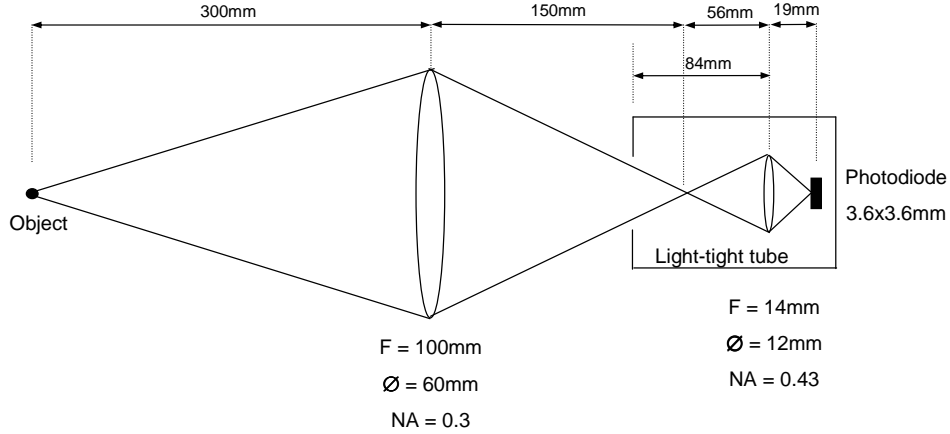


Figure 5.18: Fluorescence measurement setup for the experimental MOT. The relevant equations to convert the photodiode photocurrent into number are given in Reference [68].

5.3 Diagnostics

Most of the information that has been obtained on BECs and thermal clouds have been obtained by optical diagnostics. Two of the most important diagnostic methods are in-situ and time-of-flight (TOF) imaging. These correspond to imaging the cloud in its trapped state and then the subsequent ballistic expansion from the trapped state respectively.

5.3.1 Recapture

For diagnostic purposes it is important to be able to determine the number of atoms in the experimental MOT and also in the magnetic trap. The simplest diagnostic method for determining atom number is measuring the fluorescence emitted by the atoms. A large collection lens is placed as close as possible to the atoms and a photodiode is then placed at the focal point of the lens. Figure 5.18 illustrates our fluorescence setup, which includes two lenses and a light-tight tube to improve signal-to-noise ratio. The fluorescence measured by the photodiode is then converted into number with the equations given in Section C.3, Appendix C. These equations derive from Reference [68].

5.3.2 Absorption Imaging

Absorption imaging is the most commonly used method of diagnostics in atom optics experiments, because it not only yields information on number but also the cloud's spatial parameters.

Optical Depth

The optical depth (OD) at a point in the cloud is proportional to the column density at that particular point. The equation for the optical depth is:

$$I = I_0 \exp(-\text{OD}(x, z, \Delta)) \quad (5.2)$$

where I is the transmitted intensity and I_0 is the intensity of the incident beam. Equation 5.2 only holds for low intensities.⁶

Many factors affect the observed OD. Light is scattered not only from the atoms, but from any imperfections in any of the optical elements in the imaging system. The observed OD is therefore lower than the actual OD.

The maximum observable OD also depends on the size of the cloud. The smaller the cloud the lower the maximum observable OD, because it is easier for the light scattered at the edge of the cloud to fill in the centre of the shadow. High magnification imaging systems make this effect worse.

Interference fringes in the probe beam can cause problems when imaging. Fringes can occur due to diffraction from the glass cell, waveplates, mirrors, lenses and the CCD array window. If the fringe pattern is stable, i.e. if the fringes do not change between images, then subtracting an image of the probe beam from an image containing the atoms will eliminate the fringes. However, if the fringes do move then subtracting the image of the probe beam will actually worsen the effect. As long as the spatial size of the cloud is different to the spatial frequency of the fringes, fitting Gaussian distributions to the cloud tends to eliminate this effect.⁷

⁶For a detailed discussion on optical depth and saturation intensity see Reference [84].

⁷For a low optical depth cloud the effect is amplified as the apparent optical depth of the fringes will dominate the resulting profile.

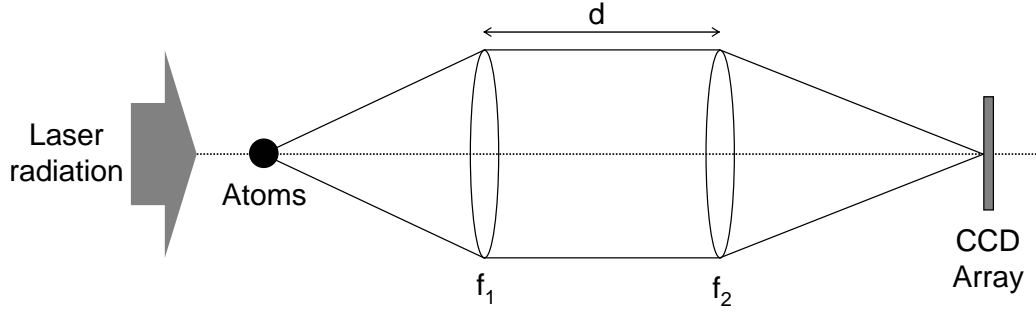


Figure 5.19: Schematic of the imaging setup.

Experimental Setup

The optical setup used for absorption is illustrated in Figure 5.19. The focal length of the two lenses are chosen depending on the magnification required. The magnification is the ratio of the two focal lengths (f_2/f_1).

To image the atoms, the current in the magnetic trap coils is turned off (in less than $300 \mu\text{s}$) and the atoms are pumped into the $F = 4$ sublevel with a $150 \mu\text{s}$ pulse of light resonant with the $6S_{1/2}, F = 3 \rightarrow 6P_{3/2}, F' = 4$ transition. The cloud is then probed by applying a $50 \mu\text{s}$ pulse of circularly polarized light resonant with the $6S_{1/2}, F = 4 \rightarrow 6P_{3/2}, F' = 5$ transition. An AOM is used for fast shuttering of the probe light.⁸ The intensity of the probe beam is generally no greater than 10% of the saturating intensity, and therefore Equation 5.2 is valid. The quantization field is the same as that required for the optical pumping. The shadow of the atoms in the beam is then imaged onto a CCD array.

The CCD array is part of a camera manufactured by Andor. The Andor camera on the experiment (DV437-FI, serial number: CCD-2611) is a frame-transfer camera and is ideal for fast imaging applications. The CCD array consists of 512×512 pixels and the pixel size is $13 \mu\text{m}^2$. The maximum frame readout per second is 3.2 which increases to 10.0 if 4×4 binning is used.

The control system for the the Andor camera is a Multi I/O Box (IO160). This in combination with the Labview program (which controls the experiment)

⁸A mechanical shutter is also included on the probe beam path (see Figure 5.7) to prevent any probe light from reaching the atoms when they are in the magnetic trap.

provides the means of controlling the image acquisition. The auxiliary output of the Multi I/O Box is set to low when the Andor software is ready for an image. Once an image is ready to be taken Labview sends a high TTL signal to the external trigger input of the Multi I/O Box to arm the camera. When the image is taken a high TTL signal is sent to the fire input of the Multi I/O Box. Once the images have been acquired Andor then sets the auxiliary output on the Multi I/O Box to high to prevent further images being taken before the images have been downloaded into the computer.

Normally three images are taken. The first image is taken after a controlled TOF (I_1), the second is an image of the probe beam taken as soon as possible after the first image (I_2), and the third image is of the background and scattered light (I_3). The background image is subtracted from both the first two images, the two files are then divided and then the natural log of the resulting file is taken (Equation 5.3):

$$\text{OD} = \ln \left(\frac{I_2 - I_3}{I_1 - I_3} \right) \quad (5.3)$$

This image is then summed in both directions and the resulting profiles are fitted with a Gaussian function (Equation 5.4) from which values for the peak optical depth and the widths can be extracted.

$$\text{Optical depth summed in the } y \text{ direction} = \exp \frac{-x^2}{2\sigma^2} \quad (5.4)$$

Knowing the magnification and the magnetic field parameters, physical quantities (e.g. density, temperature) can be derived from the data using the following equations:

$$\text{Radial Temperature, } T_r = \frac{m\omega_r^2\sigma_r^2}{k_B} \quad (5.5)$$

$$\text{Number, } N = \frac{2\pi\text{OD}_{\text{pk}}\sigma_r\sigma_z}{\sigma_0} \quad (5.6)$$

$$\text{Peak Density, } n_{\text{pk}} = N\omega_r^2\omega_z \left(\frac{m}{2\pi k_B T} \right)^{\frac{3}{2}} \quad (5.7)$$

where $\sigma_0 = 3\lambda^2/2\pi$, σ_z and σ_x are the widths of the cloud in the axial and radial directions respectively.

Focussing and Magnification

The imaging system needs to be focussed in order to obtain accurate values for the cloud widths. The focussing is done by firstly creating a very small cloud. The second lens of the imaging system (Figure 5.19) is mounted on a translation stage capable of micron precision adjustment. A graph is plotted of the radial width of the cloud versus the position of the second lens. The minimum in the radial width corresponds to the focussed position of the second lens.

The magnification of the imaging system can be determined by plotting the radial centre of the cloud versus the TOF. By fitting

$$s' = s + \frac{1}{2}g't^2$$

to the data, where s is the actual displacement, g' is the apparent acceleration due to gravity and t is the value of the TOF, a value for the apparent acceleration due to gravity (g') is obtained. The value obtained from the fit depends on the size of the pixel and the magnification of the imaging system. This value is then compared to the actual value of the acceleration due to gravity (g) to determine the magnification:

$$M = \frac{g'\Delta x}{g}$$

where M is the magnification, Δx is the pixel size in μm , and g is the acceleration due to gravity. For the data in Figure 5.20 the magnification is 1.008(7).

Lensing Effects

If the probe beam is detuned from resonance, the refractive index of the cloud is no longer 1 and because of the variations in the density across the cloud, the cloud acts like a lens. If the imaging system is focussed, no change in the shape of the cloud is observed when the probe beam is detuned. However, if the cloud is out of focus then the cloud shape becomes very distorted. This lensing effect can be used as another method of focussing the cloud i.e. the appearance of the cloud should not change with the detuning (red or blue) of the probe light when the imaging system is in focus.

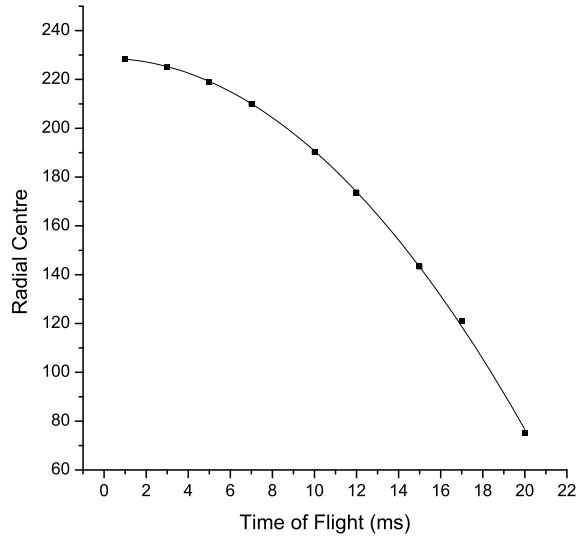


Figure 5.20: Determining the magnification of the imaging system. The acceleration due to gravity given by the fit is 0.76 m s^{-2} . This value must be compared to the actual acceleration due to gravity in order to determine the magnification.

5.3.3 Comparison of Recapture and Imaging

Most experimental results are obtained by imaging the cloud. However, recapture measurements can sometimes be the only method of reliably obtaining the atom number.

Imaging large atom densities is difficult as lensing effects can distort the number measurement. MOT recapture measurements do not suffer from this. Another advantage of MOT recapture measurements is that the fluorescence can be read straight off an oscilloscope connected directly to the photodiode (a photodiode circuit contains a current-to-voltage follower). To obtain the atom number there is therefore no need for a probe beam and expensive CCD camera or any data processing. The equations in Section C.3, Appendix C are used to determine the atom number. The fluorescence measurements can also be calibrated using the number obtained from absorption imaging.

However there are some disadvantages to recapturing atoms in the MOT:

- it is very difficult to measure small numbers of atoms due to the background noise from scattered light. This results in a poor signal-to-noise ratio.

- the MOT beam intensities change and it is difficult to determine the collection solid angle accurately. These values are required to determine the atom number [68].
- the method gives no information on the spatial size of the cloud, therefore the temperature of the atom cloud is unknown.⁹

For large optically thick clouds the best solution is to use absorption imaging and recapture in parallel. For the imaging – the probe light is detuned in order to accurately determine the widths whereas the number is determined from the MOT recapture. The obvious disadvantage of this method is that two identical clouds need to be created for each measurement.

5.4 Optimization and Characterization

It is possible to build and set up the apparatus as described above and succeed in loading the magnetic trap. However, the temperature of the atom cloud would be high, the number would be low, and strong heating would be observed because of the presence of other magnetically trappable states. Optimization is therefore required in order to prepare a high number, low temperature and pure (i.e. only $(3, -3)$ state) atom cloud. The following subsections describe the attainment of this goal.

5.4.1 Pyramidal MOT

Two factors that affect the number of atoms captured in the pyramidal MOT are the intensity and detuning of the laser radiation. Figure 5.21 illustrates the dependence of the number of atoms captured on the power (for a fixed beam size and intensity) and the detuning of the laser beam. The number of atoms is determined from fluorescence measurements. A collection lens of focal length 10 cm was placed at approximately 22 cm from the centre of the pyramid and a

⁹In a MOT the spatial size of the cloud is not enough to determine the temperature.

photodiode was placed at the focal point of the lens.¹⁰

5.4.2 Experimental MOT

The number of atoms collected in the experimental MOT depends on the detuning and power of the laser radiation, and the magnetic field gradient. The optimum conditions are determined experimentally. Figure 5.22 illustrates the dependence of the number on the detuning and the power of the laser light. The experimental MOT atom number also depends on the pyramid settings, and therefore the pyramid settings are fixed during optimization of the experimental MOT parameters. The pyramid settings for the data plotted in Figure 5.22 were 37.0 mW of cooling light and 1.3 mW of repumping light. Initially, increasing the power in the experimental MOT leads to an increase in the number of trapped atoms. However, once the power is greater than approximately 30 mW the number collected starts to drop. This is most likely due to radiation pressure in the cloud of atoms preventing further capture of atoms in the experimental MOT collection region.

5.4.3 Loading the Experimental MOT

The number of atoms collected in the experimental MOT not only depends on the experimental MOT parameters but also on the pyramidal MOT parameters. Figure 5.23 illustrates the dependence of the fluorescence¹¹ in the experimental MOT on the power and detuning of the pyramidal light. We found that there was a direct correlation between the maximum load and the number of atoms loaded in 10 s. Therefore when maximizing the total atom number loaded, we plotted the 10 s load against the experimental parameter under consideration. This not only saved time but prevented human error caused when deciding when the load in the MOT was at its maximum.

The number collected in the experimental MOT increases with increasing pyra-

¹⁰As explained in Section 5.1.5 the MOT must be moved, using the magnetic field generated by the shim coils, in order to observe the fluorescence.

¹¹For optimization, the fluorescence is generally plotted rather than the number as it is the position of the maximum that is required.

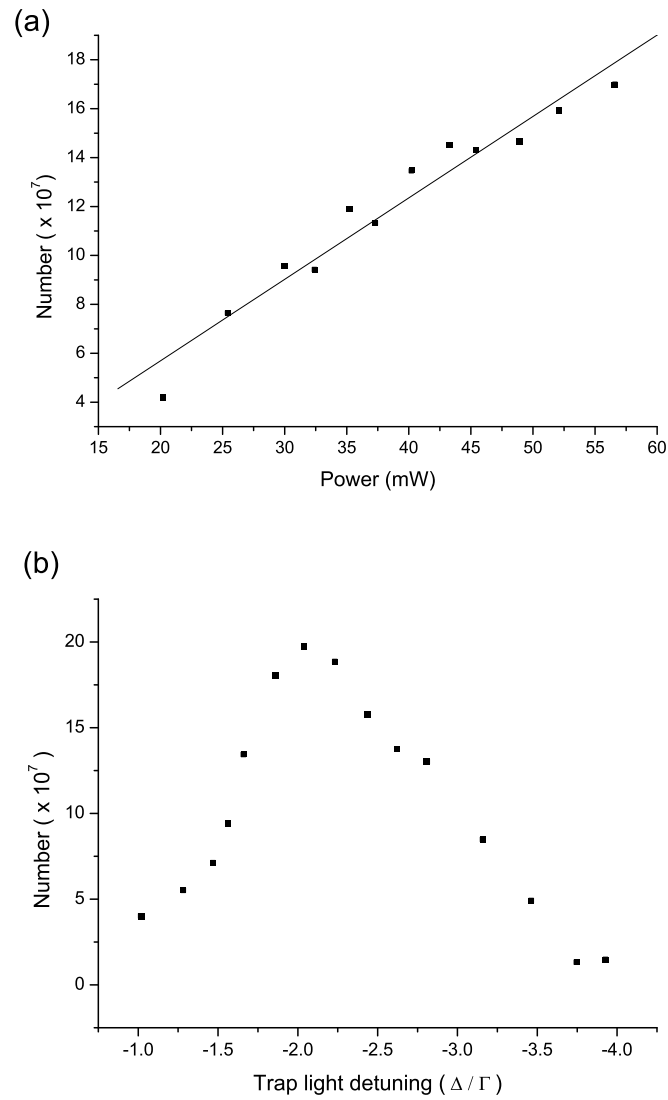


Figure 5.21: Optimization of the pyramid atom number. The dependence of the number on: a) power and b) laser detuning (the trap light detuning is given in units of Δ/Γ where Γ is the natural decay rate of the excited level).

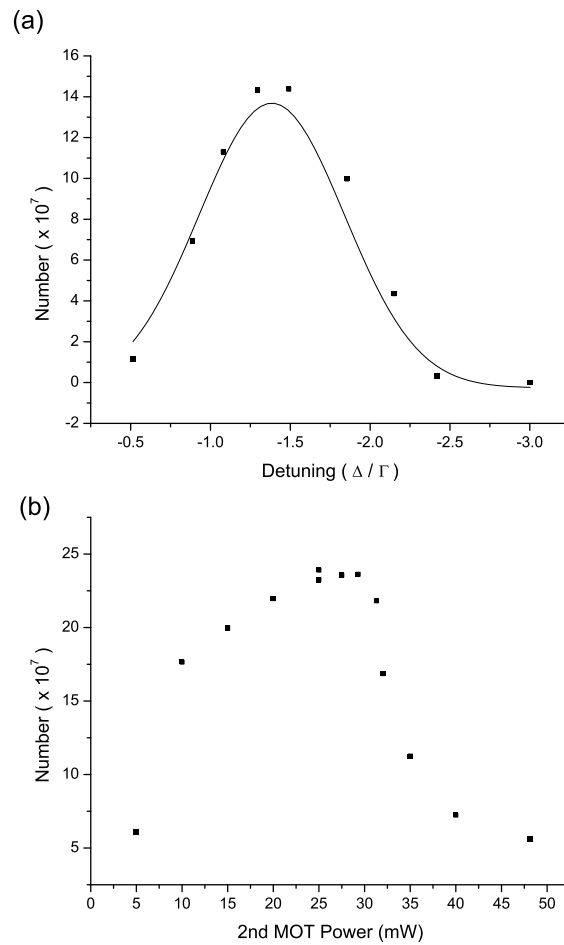


Figure 5.22: The optimum conditions for maximum number captured in the experimental MOT: a) optimum detuning is at $\approx -1.38\Gamma$ ($\equiv 7.2$ MHz) and b) the optimum power ≈ 29 mW (taken at a detuning of 8.1 MHz).

mid power (Figure 5.23 (b)), therefore the power on the experimental MOT is set to 28 mW and the remaining power is put on the pyramid (using the half-wave plate situated after the MOPA). Once the number collected was optimized, 10^9 atoms could be loaded in approximately 40 s.

5.4.4 Compressed MOT and Molasses

The MOT is optimized for capture of large atom number. This is not however, the optimum conditions for loading into the magnetic trap. Two stages are therefore required prior to loading the magnetic trap: compressed MOT (CMOT) and optical molasses.

The purpose of the compressed MOT (CMOT) is to increase phase-space density in the cloud and to match the centres of the MOT and magnetic trap. It is also beneficial to compress the cloud in order to improve the collision rate upon loading the magnetic trap. The parameters that affect the CMOT are: the quadrupole gradient, the laser radiation detuning (both cooling and repumping), and the duration.

The quadrupole gradient is increased from 10.2 G cm^{-1} to 20.6 G cm^{-1} and the duration of the CMOT stage is 30 ms. The duration of the CMOT stage is a balance between compression (increased collision rate), and an increase in heating and loss rate. During the CMOT stage the repumping laser is detuned in order to reduce the transition rate. This is equivalent to reducing the power of the repumping light.

The shim settings are varied in order to match the centre of the cloud with the magnetic trap centre. If these centres are not matched then sloshing occurs (Section 5.1.7). The amplitude of oscillation in one direction is plotted against the corresponding shim voltage. The data is fitted with a parabola and the position of the minimum in the amplitude of oscillation is noted. This is carried out for the two observable directions. However, the sloshing in the other direction must also be minimized. Because of the presence of cross-terms in the expression for the magnetic trap potential, slosh in the unseen direction translates into the visible

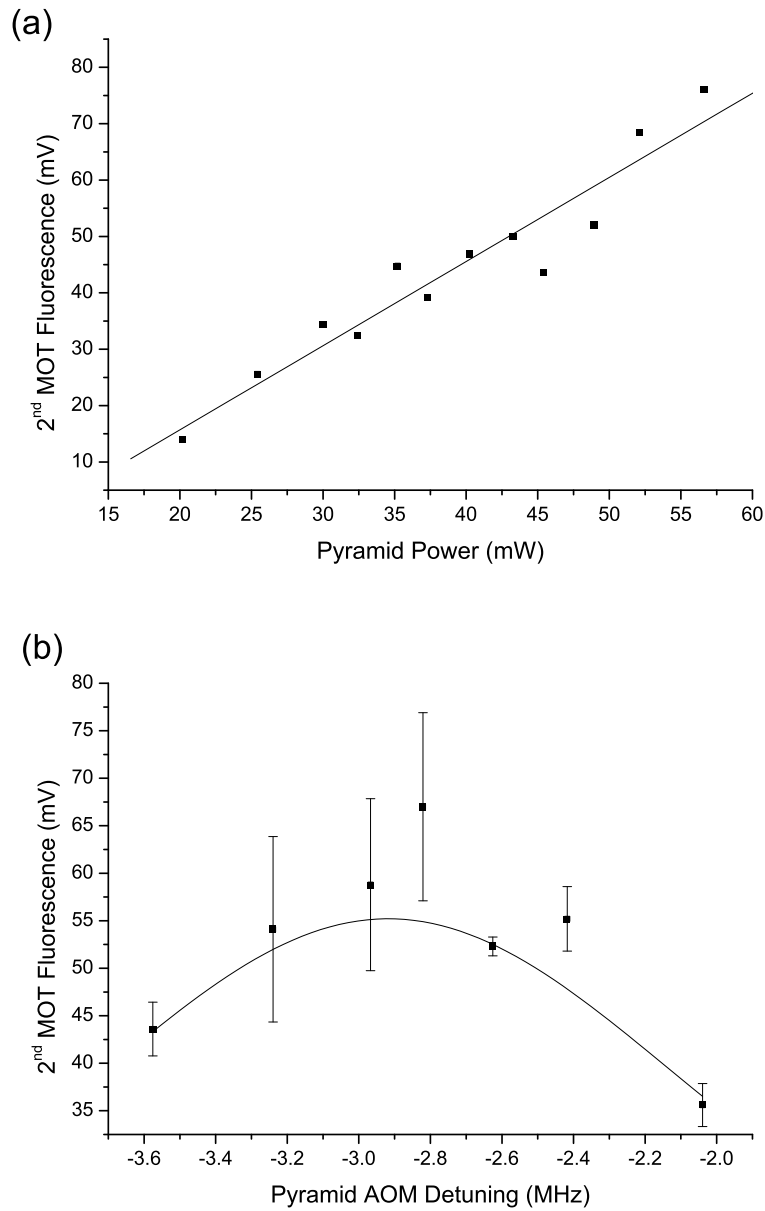


Figure 5.23: The dependence of the fluorescence in the experimental MOT (10 s load) on the pyramid power (a) and detuning (b).

directions. Therefore by observing one direction, it is possible to minimize the slosh in the other unseen direction. It is crucial to repeat the measurements and obtain the global minimum, as local minima can occur when slosh in two directions cancels.

As the CMOT stage causes heating of the cloud, the molasses stage is required in order to cool the atoms prior to loading the magnetic trap. For the molasses stage the quadrupole field is turned off, and the shim coils are left on and are adjusted for a smooth even expansion of the cloud. The optimization of the shim coil settings is done by sight. There are two infrared cameras observing the MOT from orthogonal directions, and therefore it is possible to observe the expansion of the cloud in all directions. The duration of the molasses stage is 15 ms. The optimum duration for the molasses is a balance between increased cooling and mode-matching the cloud with the magnetic trap.

5.4.5 Optical Pumping

In a MOT, the atoms can be in any magnetic substate (m_F), therefore on loading the magnetic trap many atoms are lost because of the increased rate of inelastic collisions. Atoms must therefore be optically pumped into a stretched state. In this case, the atoms are optically pumped into the $F = 3$, $m_F = -3$ state.

The atoms are optically pumped into the (3,-3) state by applying a 1.4 ms pulse of circularly polarized light resonant with the $6S_{1/2}, F = 3 \rightarrow 6P_{3/2}, F' = 3$ transition. The quantization field is produced by the appropriate MOT shim coil (y - z shim coil). A current of 2.09 A is required to produce a field of 2.61 G. During optical pumping the MOT beams are detuned to the $6S_{1/2}, F = 4 \rightarrow 6P_{3/2}, F' = 4$ transition in order to ensure that no atoms remain in the $F = 4$ state.

The efficiency of the optical pumping depends on a number of parameters: the detuning and power of the laser radiation, the pulse length, and the magnitude of the quantization field. These parameters are all optimized experimentally. Figure 5.24 illustrates the dependence of the loading efficiency in the magnetic trap on the detuning of the laser radiation and the pulse length. The measurements

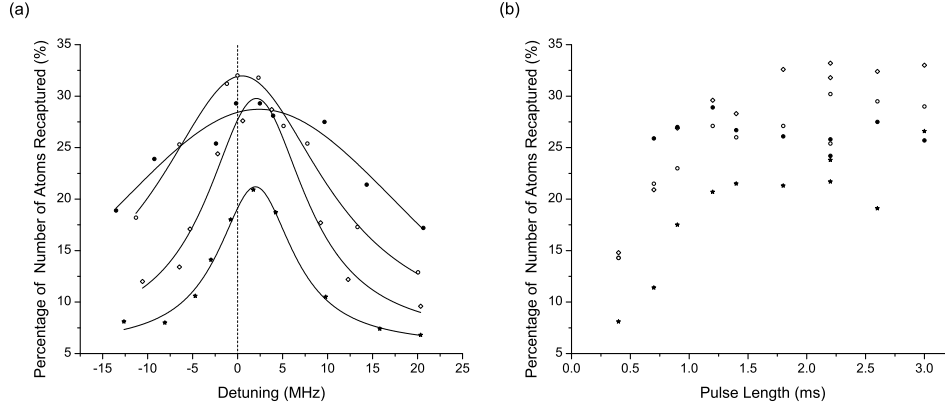


Figure 5.24: Graphs of the percentage of number of atoms recaptured against: (a) the detuning voltage from the $F=3 \leftrightarrow F'=3$ transition (pulse length = 0.9 ms) and (b) the pulse length (detuning = 2.3 MHz) – for different values of the AOM attenuation: 3.554 V (\star), 3.94 V (\diamond), 4.4 V (\circ) and 4.8 V (\bullet). The dotted line in graph (a) marks the position of the $F=3 \leftrightarrow F'=3$ transition.

are carried out by noting the fluorescence in the MOT, loading the magnetic trap, and then recapturing the atoms into the MOT in order to obtain the fluorescence measurement. The percentage of the number of atoms recaptured is then plotted.

5.4.6 Calibration of Magnetic Trapping Parameters

In order to determine many of the physical quantities such as temperature and density, it is important to know the parameters of the magnetic trap accurately.

Calibration of the Trap Bias Magnetic Field

The value of the bias magnetic field is determined by measuring the radio-frequency at which the atoms are expelled from the centre of the trap. To determine this value accurately, a graph of atom number versus frequency is plotted (Figure 5.25). Each point on the graph is obtained by varying the end frequency of an evaporation ramp.

Cutting from both sides of the cloud produces a graph consisting of two lines which should intersect at $y = 0$. The rf surface has a finite depth (≈ 10 kHz) which accounts for a small fraction of the gap seen in Figure 5.25. The majority of the gap is due to a resonance in the coil at that particular frequency. We

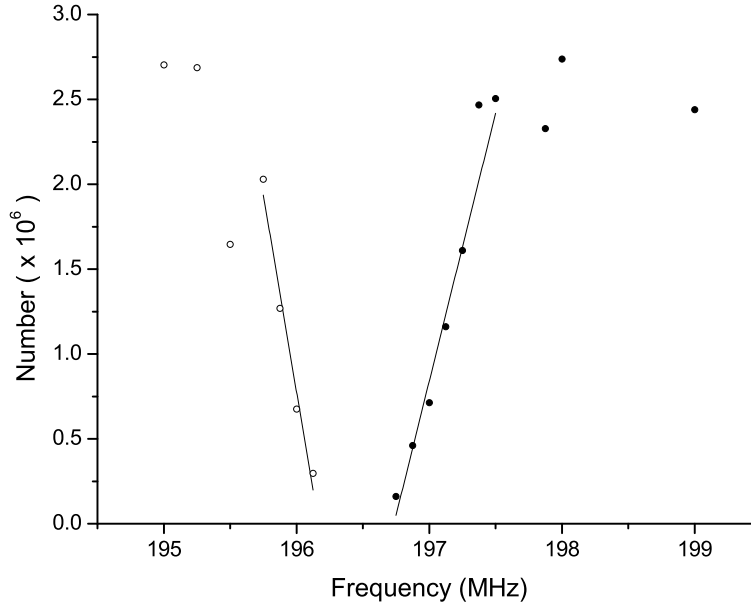


Figure 5.25: Magnetic field calibration. The point at which the straight lines cross the x -axis corresponds to the rf frequency that drives transitions at the bottom of the magnetic trap. The \circ and \bullet correspond to cutting from above and below the cloud respectively.

average the two values of the frequency at $y = 0$ and using the Breit-Rabi equation (Equation 2.6), the value of the magnetic field at the bottom of the trap can be computed. For Figure 5.25 the centre frequency is 196.451(18) MHz which corresponds to a magnetic field value of 509.870(43) G.

Calibration of the Magnetic Trap Frequencies

It is possible to calculate the field, and therefore the frequencies of the magnetic trap analytically. However, even when taking into account thickness and curvature of the baseball coil it is still not possible to determine the trap frequencies more accurately than within 10%. The most precise way of determining the magnetic trap frequencies is by using the atoms.

As mentioned previously, the trap frequencies can be determined from the sloshing frequencies. It is possible to induce sloshing upon loading the magnetic trap by modifying the trapping potential faster than the atoms can follow. Figure 5.26 is an example of a set of data taken to determine the trapping frequencies. Each

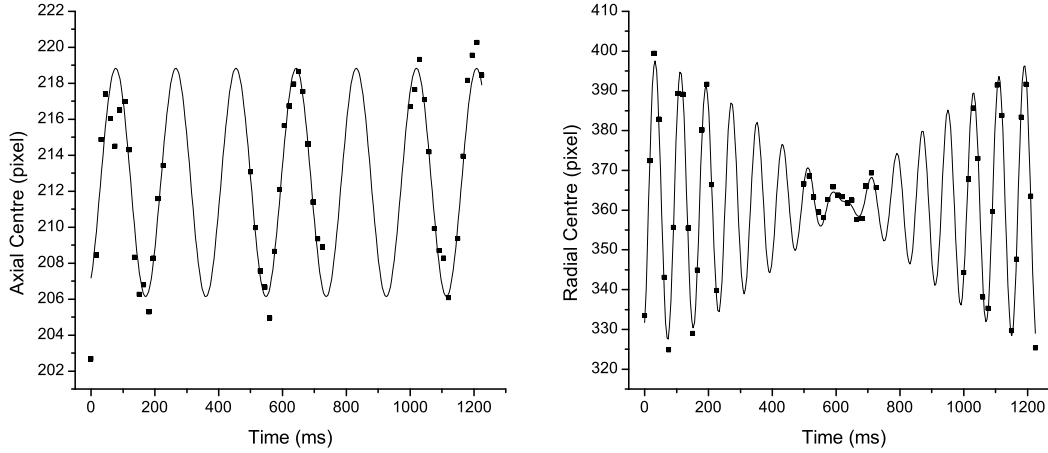


Figure 5.26: Determining the frequencies of the magnetic trap. From these plots it is possible to extract the axial and both radial trap frequencies. The axial trap frequency is 5.302(19) Hz and the radial frequencies are 12.194(33) Hz and 12.842(40) Hz.

point on the graph represents a single measurement (by imaging) of the positions of the centre of the cloud in the radial and axial directions. The axial frequency and both radial frequencies are determined from the plot. The values obtained for the trap frequencies are 5.302(19) Hz axially, and 12.194(33) Hz and 12.842(40) Hz radially.

Measurement of the Trap Lifetime

It is important to know the trap lifetime as this can limit the time available to evaporate and perform experiments.¹² The trap lifetime is determined by plotting the number versus the hold time in the magnetic trap. If an exponential decay is fitted to the data, the value for the trap lifetime can be extracted. The lifetime obtained from Figure 5.27 is 537 s (≈ 9 minutes).¹³

¹² τ_b is used in equations to evaluate the two-body and three-body inelastic loss rate coefficients (see Chapter 6).

¹³This lifetime is long compared to many other alkali metal experiments. We believe that the reason for the long lifetime is because initially when the experiment was being built, the vacuum system was baked out three times: initially without the glass cell; then with the glass cell attached; and then a further time as the pyramid mirrors were displaced during moving the vacuum system to the optical table, and therefore the mirrors were repositioned and the system baked out a final time.

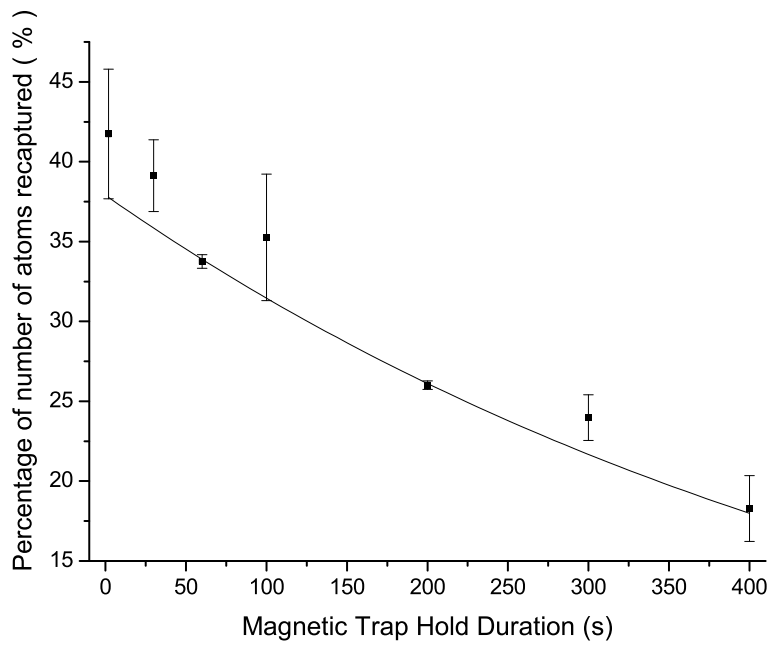


Figure 5.27: Determining the magnetic trap lifetime. A plot of percentage of number of atoms recaptured versus the hold time in the magnetic trap. The line is a weighted exponential fit and gives a value for the trap lifetime of $\tau_b = 537$ s. (The error bars are the standard deviation of the data.)

Loss Measurements

There were two main reasons for studying the magnetic field dependence of inelastic loss rates in caesium. Inelastic losses play a critical role in determining the success or failure of evaporative cooling and it is therefore essential to characterize the losses fully before finalizing the evaporation strategy. Also, due to the work carried out at Stanford [38] and the subsequent theoretical analysis at NIST [37] we felt that to characterize these losses experimentally would be of interest, not only to us but to other research groups studying the collisional properties of caesium.

Initially, the three resonances that occur between 105 and 145 G were mapped out using atomic caesium clouds at a temperature of 250 nK. These resonances had already been observed by Chu *et al.* at Stanford [38] and the resonance positions are therefore confirmed and with reduced uncertainty. The results are given and discussed in Section 6.2.

In the collisional structure of caesium, Feshbach resonances can show a significant shift in position and width with respect to temperature [37]. To demonstrate this shift experimentally, the resonance centred at approximately 118.5 G resonance is plotted for two further temperatures – 80 nK and 800 nK. Theoretical calculations were also undertaken by Julienne and the results are included and discussed in Section 6.3.

6.1 Inelastic Feshbach Resonances

Resonances are labelled using two quantum numbers, f and l where l is the orbital angular momentum of the colliding atoms and f is the total hyperfine quantum number given by $f = f_a + f_b$ where a and b denote the two colliding atoms individually. If the entrance and exit channels are identical i.e. $(f, l) = (f', l')$, then the interaction between the two atoms is due to the exchange forces, whereas if they are different the interaction is due to relativistic spin-dependent forces.

The scattering in ultra-cold bosonic atomic clouds is purely s -wave. However, the s -wave entrance channel can couple to higher partial waves (d, g) through spin-dipolar coupling.¹ These resonances tend to be narrow and if the equivalent higher wave basis² is not included in the analysis then these resonances are not theoretically observed.³ The three Feshbach resonances that occur in the $(3, -3)$ state between 105 and 145 G are d -wave resonances.

6.1.1 Comparison of Theoretical and Experimental Data

Generally, the theory quotes the event rate coefficient rather than the collision rate coefficient. The event rate is the number of inelastic collisions that occur in unit time and therefore the decay rate of the density n is:

$$\dot{n} = -2K_2n$$

The inelastic collision rate (dependent on K_2 and K_3 , and the density) specifies the number of atoms lost per unit time, therefore the decay rate of the density for two-body inelastic loss is:

$$\dot{n} = -K_2n$$

¹Only partial waves of even l are allowed for bosons because of the symmetry of the wavefunction.

²In order to observe a d -wave resonance, the d -wave basis functions must be included in the coupled channel calculations.

³Examples of d -wave resonances are given in Reference [103].

Two atoms are lost in a two-body collision (three atoms are lost in a three-body collision) therefore K_2 is equal to twice the event rate coefficient quoted:

$$K_2 = 2 \times \text{event rate coefficient}$$

6.2 Feshbach Resonances in the $F = 3, m_F = -3$ State

To determine the two-body inelastic collision rate coefficient K_2 , the evolution of the atomic cloud in the magnetic trap must be studied. The magnetic trap is loaded at 139 G from a MOT as described in Chapter 5. After an initial short evaporation ramp to eliminate all m_F states except $(3, -3)$ from the magnetic trap⁴ we are left with a pure cloud of approximately 2×10^8 atoms at a temperature of $40 \mu\text{K}$. Forced rf evaporation is then implemented until the temperature of the cloud reaches approximately 250 nK. The magnetic field is then changed by ramping the current in the baseball coil to a new value. After variable hold times in the magnetic trap, images are recorded of the cloud at the field under investigation. From the resulting computational analysis the number, temperature, and density as a function of time are obtained.

6.2.1 Determination of the Two-Body Inelastic Collision Rate Coefficient

Under the conditions of our experiment two-body collisions are the dominant inelastic loss process in caesium. Therefore for the analysis only two-body collisions and background collisions are assumed.⁵ Integrating Equation 4.4 (Chapter 4) yields an expression for the number of atoms remaining in the trap after time t :

$$\ln(N) + \frac{t}{\tau_b} = \ln(N_0) - K_2 \int \langle n \rangle dt \quad (6.1)$$

where N_0 is the initial number of atoms in the trap (i.e. the number of atoms at time $t = 0$) and $\langle n \rangle$ is the mean density. The background loss rate τ_b , is determined

⁴All evaporation details are given in Chapter 7.

⁵This is implemented by setting $K_3 = 0$.

separately from data taken at low density (Figure 5.27, Chapter 5), and is therefore fixed in the analysis (in this case $\tau = 537$ s). The mean density as a function of time (Figure 6.1 (a)) is fitted with Equation 6.2.

$$\langle n \rangle = y_0 + A_1 \exp(-t/\tau_1) \quad (6.2)$$

The time integral of the density in Equation 6.1 is determined by evaluating the area under the mean density curve (Figure 6.1 (a)) and is therefore equal to the integral of Equation 6.2:

$$\int \langle n \rangle dt = y_0 t + A_1 \tau_1 (1 - \exp(-t/\tau_1)) \quad (6.3)$$

After evaluating Equation 6.2, $\ln N + t/\tau_b$ is plotted against time and the resulting plot is fitted with Equation 6.4.

$$\begin{aligned} y &= P1 + P2 \left[\int \langle n \rangle dt \right] \\ &= P1 + P2 [y_0 t + A_1 \tau_1 (1 - \exp(-t/\tau_1))] \end{aligned} \quad (6.4)$$

Figure 6.1 is an example of a set of data taken at a single magnetic field. The dotted curve on the plot (Figure 6.1 (b)) is a fit of the data assuming three-body and background collisions ($K_2=0$). This clearly shows that the loss is indeed two-body in nature under the conditions of our experiment.

6.2.2 Experimental Results

Following the analysis described previously, the value of the two-body inelastic collision rate coefficient can be plotted as a function of magnetic field. For magnetic field values between 105 and 150 G, three resonances are observed and are plotted in Figure 6.2.⁶

The error bars in the plot represent only the uncertainty derived in fitting the K_2 data curve (Figure 6.1 (b)). Other sources of error, principally in the determination of the density lead to a larger error in the K_2 coefficient ($\approx 40\%$). The density can vary up to a factor of 10 across the magnetic field range chosen,

⁶The theoretical prediction is also included on the figure.

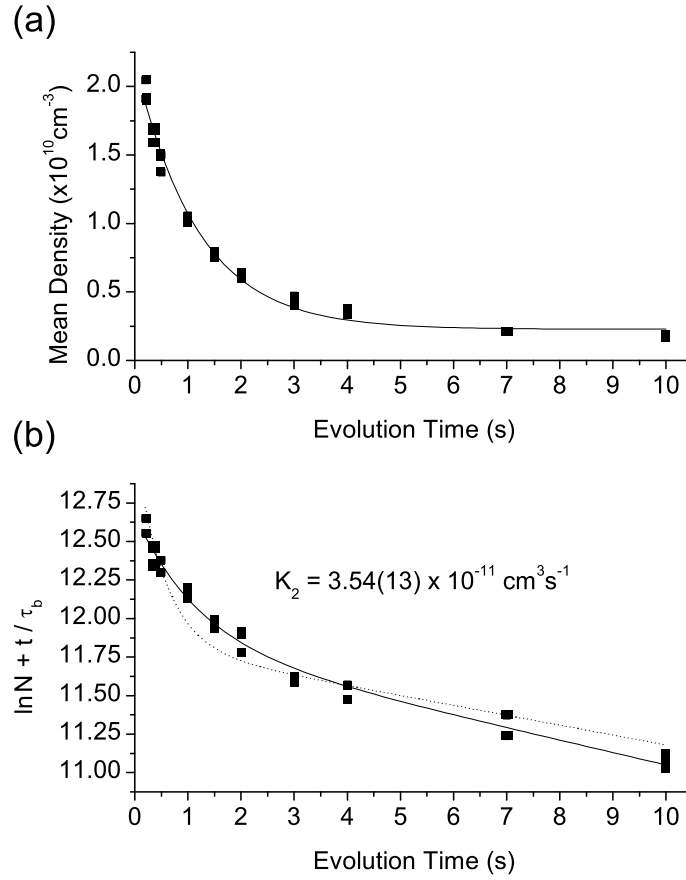


Figure 6.1: (a) A plot of the measured mean density against the evolution time of the cloud for a magnetic field value of 133.78 G. (b) Evaluation of K_2 . The solid/dotted curves show the results of a two-/three-body analysis of the data. The scatter in the the data points indicates the shot-to-shot reproducibility and is the dominant source of uncertainty.

this in turn affects the inelastic loss rate observed as the losses associated with two-body collisions are density dependent. This effect is significant for the resonance centred at 109 G as the cloud is ramped across both other resonances before the hold time in the magnetic trap. This is also true of the temperature – initially the temperature of the cloud is 250 nK, but ramping the magnetic field across the resonances can cause the temperature of the cloud to rise by 100 nK.

The centres (position) and widths (FWHM) of each resonance are determined by performing a weighted fit of a Lorentzian line shape to each of the resonances individually, allowing for the sloping background associated with a broad resonance

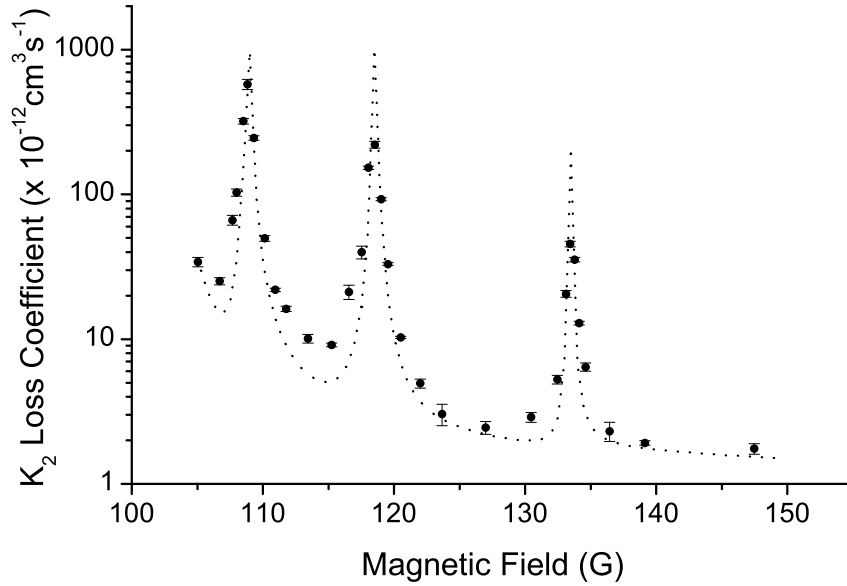


Figure 6.2: Two-body inelastic collision rate coefficient for $(3, -3)$ state as a function of the magnetic field. The dashed curve is the theoretical prediction by Julienne and co-workers [50] at 50 nK with the collisional parameters determined by the Stanford data [38].

at lower fields:

$$y = y_0 + mx + \frac{2A}{\pi} \frac{\gamma}{\gamma^2 + 4(x - x_c)^2} \quad (6.5)$$

The results obtained for the peak positions are given in Table 6.1. The errors of 0.03 to 0.06 G are largely due to the uncertainties in the calibration of the magnetic field. The FWHM of all three resonances are less than a Gauss. The predictions of the theoretical model [50] constrained by the data from the Stanford group [38], and their results [121] for the three resonances at a temperature of 250 nK are also given in Table 6.1. Our results are in good agreement with the previous experimental results and the theoretical predictions. The difference in errors between the Stanford data and the theoretical predictions is due to the fact that the theoretical predictions are made using very precise measurements of only three resonances. The three resonances discussed in this chapter were not used for the theoretical predictions. The error in the Stanford measurements of the three resonances used for the theoretical calculations is 20 mG, and therefore the theoretical predictions cannot quote an error of less than 20 mG. The three resonances discussed in this

$B_{\text{Oxford}}(\text{G})$	$B_{\text{Stanford}}(\text{G})$	$B_{\text{Theory}}(\text{G})$
108.87(6)	108.76(20)	108.97(2)
118.46(3)	118.05(20)	118.57(2)
133.52(3)	133.14(20)	133.48(2)

Table 6.1: Values for the inelastic Feshbach resonances in the $(3, -3) \times (3, -3)$ state of a pair of atoms between 105 and 135 G. The values in the first column are the results from our experiment in Oxford. Experimental values obtained from Reference [121] are given in the second column and the third column contains the theoretical values obtained from Reference [50].

chapter were not experimentally characterized as accurately which resulted in an error of 200 mG.

6.3 Temperature Dependence of the 118.5 G Resonance

Following the characterization of the three resonances, and the good agreement between the results and the theoretical predictions, it was decided to illustrate experimentally the dependence of the two-body inelastic collision rate coefficient on temperature. The magnetic field range chosen was 113 to 125 G in order to not only observe the temperature dependence of K_2 off-resonance, but also to observe the change in width, position and height of the resonance centred at approximately 118.5 G.

6.3.1 Experimental Results

The experimental procedure was similar to the procedure used to take the previous data. For this experiment atom clouds were prepared at temperatures of 80 nK or 800 nK by varying the rf evaporation ramps. The evolution of the cloud at different magnetic fields was plotted and the data then analyzed to determine K_2 for each temperature at each magnetic field value. Figure 6.3 is a plot of the two-body inelastic collision rate coefficient for the $(3, -3)$ state in caesium as a function of magnetic field. The plot consists of data taken at three different temperatures: 80,

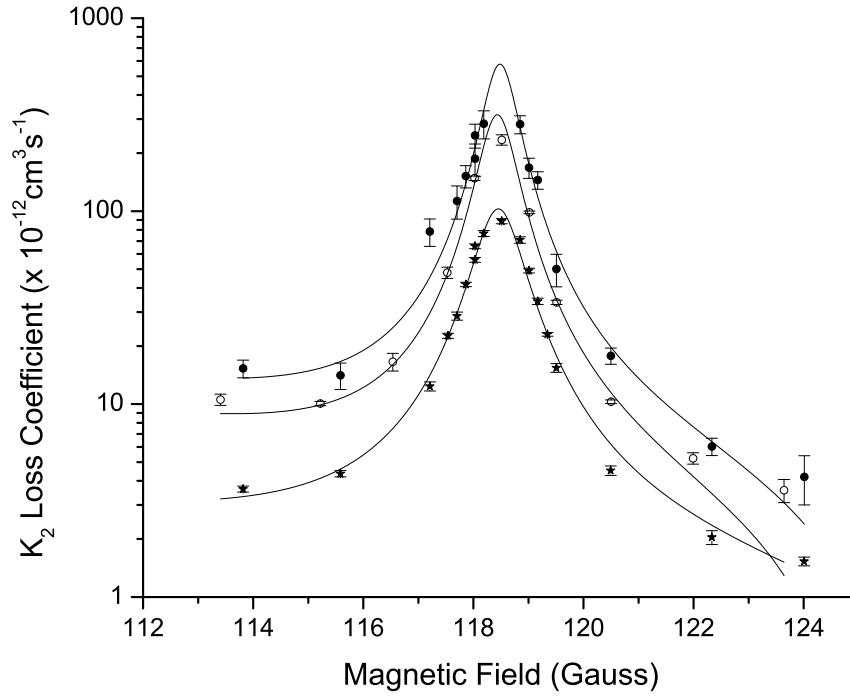


Figure 6.3: Two-body inelastic collision rate coefficient for $(3, -3)$ state as a function of magnetic field for three temperatures: 80 nK (\bullet), 250 nK (\circ), and 800 nK (\star). The fit may appear to be worse for high fields (right hand side of the graph) but this is simply a consequence of the logarithmic scale. Figure 6.4 contains plots of the resonance for each individual temperature on a linear scale.

250, and 800 nK.⁷

The 80 and 800 nK data contain an increased number of points in order to improve the accuracy of the fits. This is especially important for the 80 nK data as it is difficult to reproduce the starting conditions for the measurements accurately (this is reflected in the magnitude of the error bars). Also, there are no points at the peak of the 80 nK data because the lifetime of the cloud at the peak is less than 1 s. Figure 6.4 contains individual plots for each temperature. The error bars in the plots (Figure 6.3 and 6.4) represent only the statistical uncertainty derived in fitting the K_2 data.

The values obtained for the peak K_2 , background K_2 , centre and width of the resonance at each temperature are given in Table 6.2. As the energy of the collision

⁷The 250 nK data set is the original loss data measurements (Section 6.2.2) and the relevant data points from that data set are included in the plot.

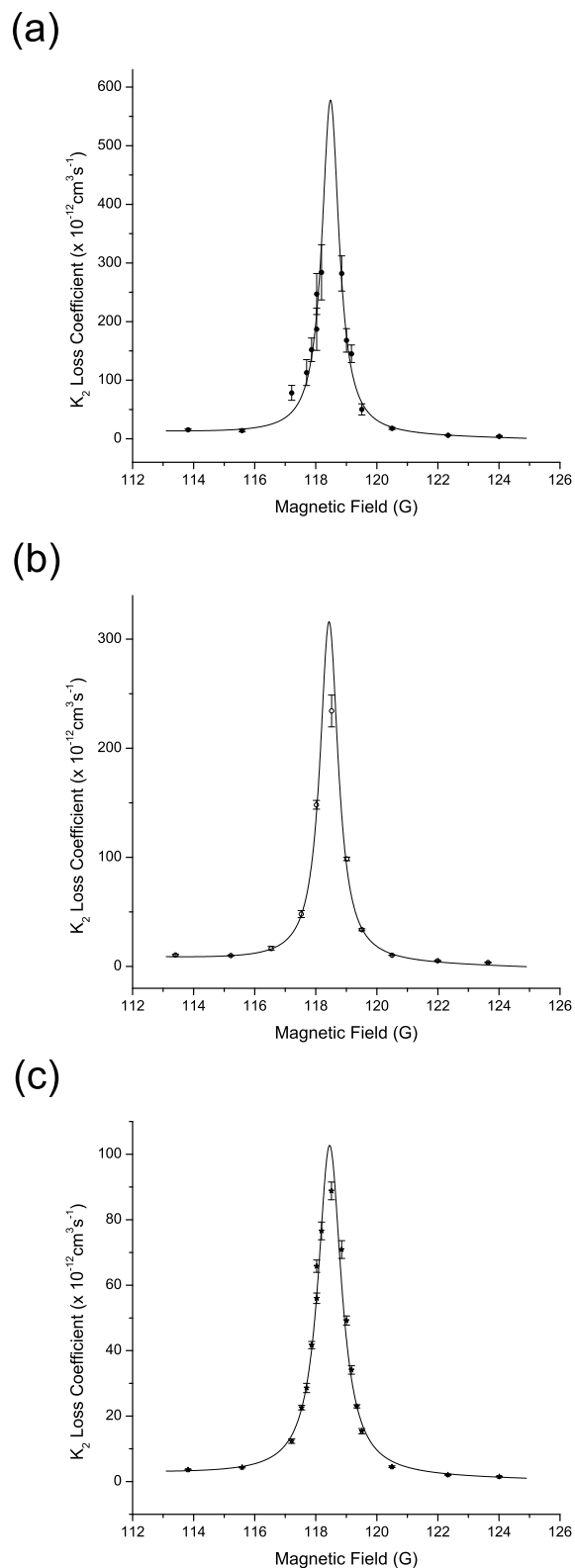


Figure 6.4: Two-body inelastic collision rate coefficient for (3,-3) state as a function of magnetic field for 80 nK (a), 250 nK (b), and 800 nK (c). (Note: these plots are on a linear scale whereas in Figure 6.3 the scale is logarithmic.)

Temperature (nK)	Position (mG)	Width (mG)	Peak K_2 ($\times 10^{-12} \text{ cm}^3 \text{ s}^{-1}$)	K_2 at 144 G ($\times 10^{-12} \text{ cm}^3 \text{ s}^{-1}$)
80	118.4822(189)	683(109)	578(104)	13.69(1.58)
250	118.4350(62)	726(28)	316(15)	8.94(31)
800	118.4538(52)	929(20)	103(3)	3.37(12)

Table 6.2: The table contains the values obtained for the position, width, peak and background K_2 for the resonance centred at approximately 118.5 G. This data is plotted with the theoretical results [50] in Figure 6.7

increases the magnitude of K_2 is greater. The peak K_2 is the value of K_2 at the central position of the resonance as determined by the fit (not by the amplitude of the Lorentzian line shape). The background K_2 is the value of the K_2 coefficient at 114 G (chosen arbitrarily to provide comparison with enhancement at the peak).⁸ The errors in K_2 are principally due to the determination of the density which in turn leads to a larger error in the K_2 coefficient, while the errors in the positions and widths of the resonance are the statistical uncertainties of the Lorentzian fit. The errors are discussed in more detail in Section 6.3.3.

6.3.2 Theoretical Results

Following the excellent agreement between the theory and the experimental data for the three resonances situated between 105 and 150 G, Paul Julienne (NIST) generated data of the inelastic two-body inelastic collision rate coefficient at five different temperatures and at magnetic field values between 114 and 124 G. Figure 6.5 is a plot of the theoretical data and the results of the fit for the peak K_2 , background K_2 , width, and position of the resonance are given in Table 6.3.

Figure 6.6 is a plot of the theoretical and experimental results of the two-body inelastic collision rate coefficient for the $(3, -3)$ state in caesium as a function of

⁸The data is fitted with a Lorentzian line shape allowing for a sloping background, therefore the background value of K_2 is only a guideline.

Temperature (nK)	Position (mG)	Width (mG)	Peak K_2 ($\times 10^{-12} \text{ cm}^3 \text{ s}^{-1}$)	K_2 at 114 G ($\times 10^{-12} \text{ cm}^3 \text{ s}^{-1}$)
80	118.4795	704	405(36)	11.7
250	118.4661	708	245(20)	6.8
500	118.4580	705	166(13)	4.5
800	118.4527	702	124(10)	3.3
1200	118.4482	699	96(7)	2.5

Table 6.3: The table contains the values obtained from the fit of the theoretical data for the position, width, peak and background K_2 for the resonance centred at approximately 118.5 G. This data is plotted with the experimental results (Table 6.2) in Figure 6.7.

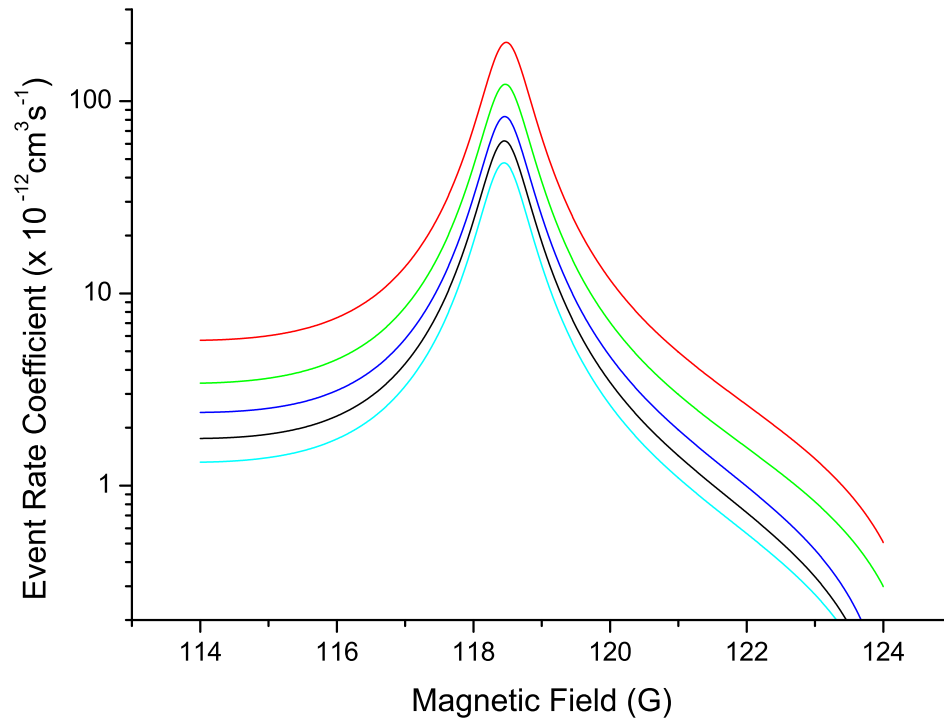


Figure 6.5: A plot of the theoretical event rate coefficient against magnetic field. The theoretical data is fitted with Lorentzian line shapes. The red, green, blue, black and cyan lines correspond to temperatures of 80 nK, 250 nK, 500 nK, 800 nK and 1200 nK respectively.

magnetic field. There is good agreement between the theory and the experimental results.

The errors quoted for the peak K_2 values in Table 6.3 are the statistical errors associated with the fit. The background K_2 is the value of the K_2 coefficient at 114 G (for comparison with the experimental data). This value is obtained from the fit and not directly from the theoretical data to allow for direct comparison with the experimental data. The difference between the two values at each temperature is no more than 4%. The error in the width due to the statistical uncertainty of the Lorentzian fit is no more than 5 mG, however the actual error is difficult to quantify. The theoretical data is constrained by the Stanford data [38] and as the error in their field calibration is 20 mG, the theoretical data cannot quote an accuracy greater than 20 mG in position. However a more realistic estimate of the error in position would be 100 mG [50].

6.3.3 Experimental and Theoretical Results

Figure 6.6 and Figure 6.7 contain the experimental and theoretical results obtained. The values of the resonance parameters for each individual temperature have already been stated in Table 6.2 and Table 6.3.

One of the major contributions to the experimental error is the difference in the initial conditions at each new value of the magnetic field and at each temperature. After the evaporation and after ramping to a new magnetic field the density of the cloud is of the order 10^{10} cm^{-3} . However, the variation in the initial densities at 80 nK is 18% while at 250 nK and 800 nK the variation is approximately 30%. This leads to large errors in determining the density and the number. Other factors that will have an effect on the number of atoms calculated is the variations in the intensity of the probe laser (I), the detuning of the probe laser (Δ), and any unwanted optical pumping effects that could occur. Also if any atoms are in magnetic substates other than the $(3, -3)$ state then the inelastic loss rate in the cloud will be significantly higher.

The error quoted for the width of the resonance is the statistical uncertainty of

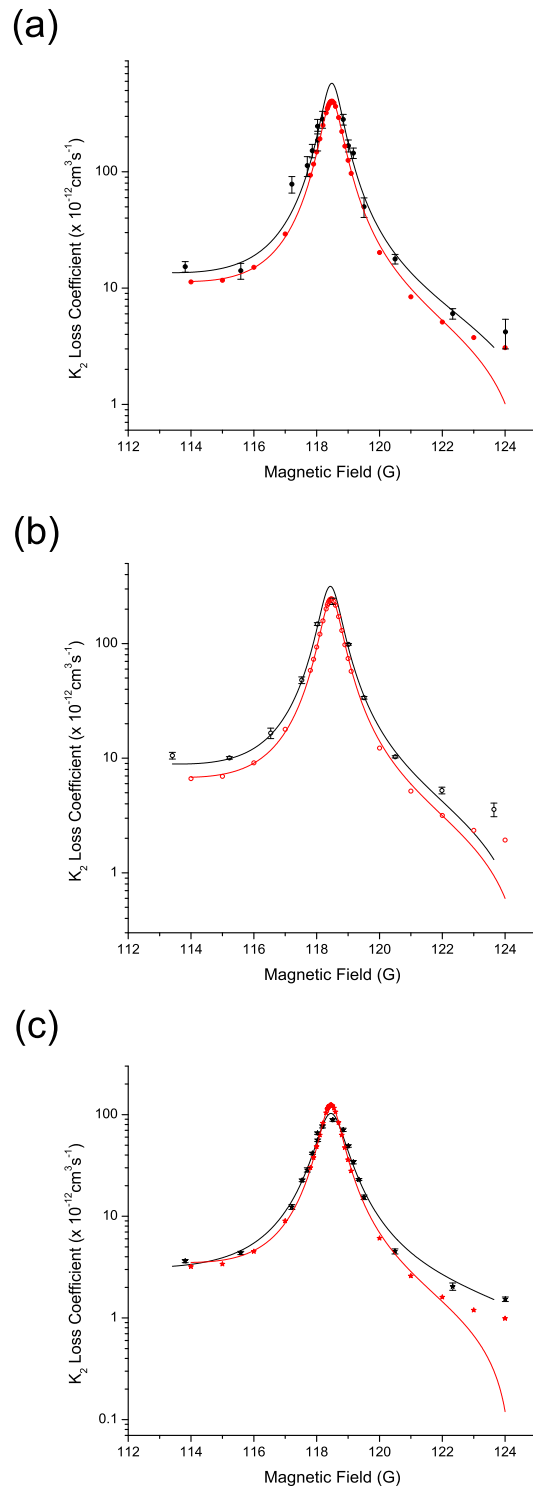


Figure 6.6: Two-body inelastic collision rate coefficient for $(3, -3)$ state as a function of magnetic field for 80 nK (a), 250 nK (b), and 800 nK (c). The black data points are the experimental results and the red data points are the theoretical results. (As mentioned previously the fit appears inaccurate on the right side of the plot as a consequence of the logarithmic scale.)

the fit, however the actual error will be greater. As the atom clouds are supported against gravity with a magnetic field gradient, a large atom cloud will span a large range of magnetic field values. For example, in a 12 Hz trap (radially) a 80 nK cloud has a FWHM of $30\mu\text{m}$. Therefore with a magnetic field gradient of 31 G cm^{-1} this leads to a spread of 92 mG across the FWHM. For a 800 nK cloud the FWHM is $93\mu\text{m}$ and therefore the spread across the cloud is 290 mG. This fully explains the large increase in width ($\approx 200\text{ mG}$) observed between the data at 80 nK and 800 nK (Table 6.2 and Figure 6.7).

Another source of error is due to the cloud sloshing in the magnetic trap. Even though the ramps to new fields should be adiabatic, some sloshing can occur. Analyzing individual data sets gives a value of 8 pixels for the standard deviation of the cloud position from the average position. This leads to a magnitude of ≈ 15 pixels for the maximum slosh, which gives a spread in the magnetic field value of $\approx 600\text{ mG}$. However, many data points are taken at different evolution times at different magnetic fields and therefore a more realistic value of the maximum slosh is 4 pixels, giving a spread in the magnetic field of $\approx 150\text{ mG}$.

As the energy of the collision increases the resonance should occur at a smaller magnetic field. The general trend in Figure 6.7 (c) indicates this, however there is a discrepancy in the 250 nK data. The 250 nK data was taken a year prior to the other data, and therefore a change in the calibration of the magnetic field (of the order of 30 mG) could account for this difference.

The results in Figure 6.7 clearly show the dependence of the resonance parameters on the collision energy. The good agreement between the theory and the experimental results further confirms the dependence of the two-body inelastic collision rate coefficient on temperature. The discrepancy in the 250 nK position data and the increase in the width for the cloud at 800 nK have been accounted for.

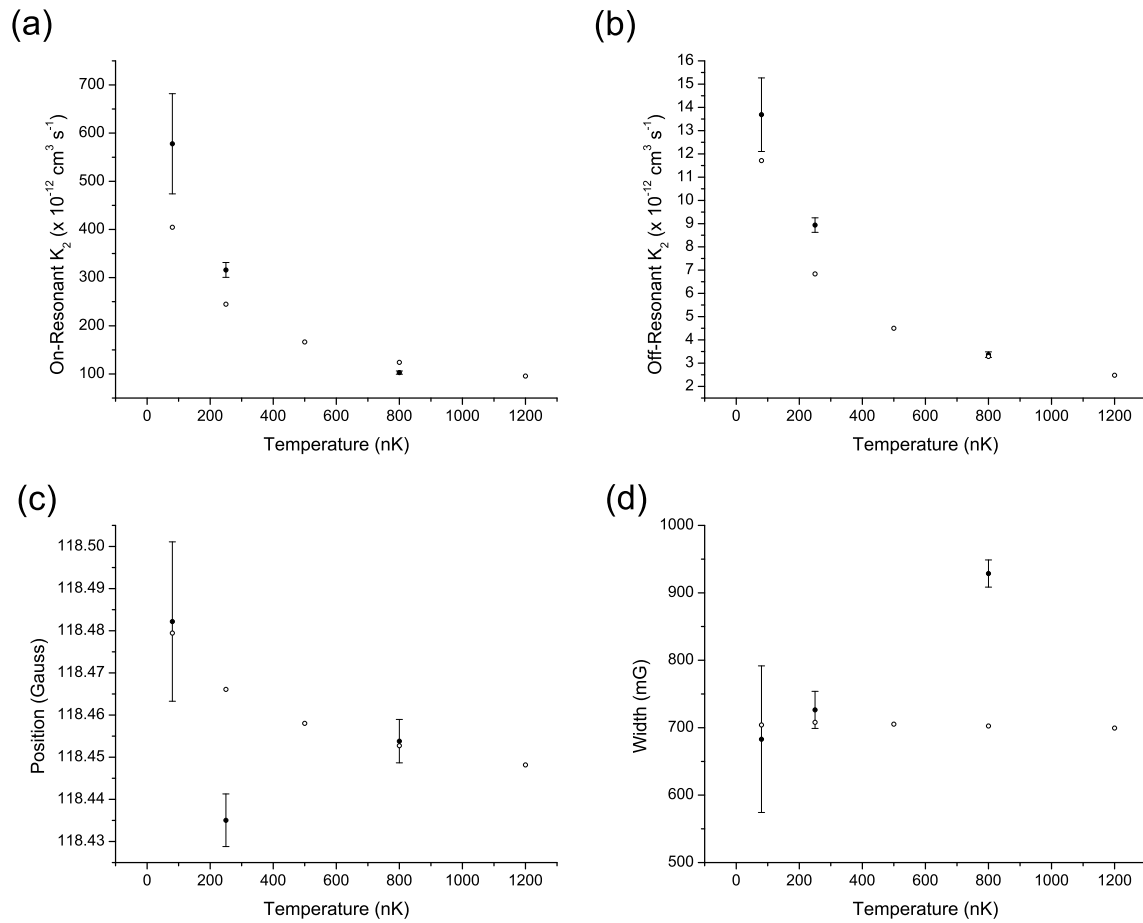


Figure 6.7: Graphs illustrating the dependence on temperature of the: peak K_2 (a), background K_2 (b), position (c), and width (d) of the resonance at 118.5 G.

6.3.4 Discussion

The Feshbach resonance at 118 G is a d -wave symmetry bound level and therefore it was believed that only including the s - and d -waves in the coupled channel calculations was sufficient to obtain accurate characterization of the resonance. Previously, it had been found that adding g -waves to the basis caused a small shift in position but little increase in the width of the resonance. However, the original theoretical data⁹ did not match our experimental data – the widths were a factor of three smaller and the background two-body inelastic collision rate coefficient was also a significant factor smaller. Professor Paul Julienne at NIST has used his computer code to compare the results of s - and d -wave basis and the s -, d - and g -wave basis for the resonance we have measured.¹⁰ Figure 6.8 illustrates the results.

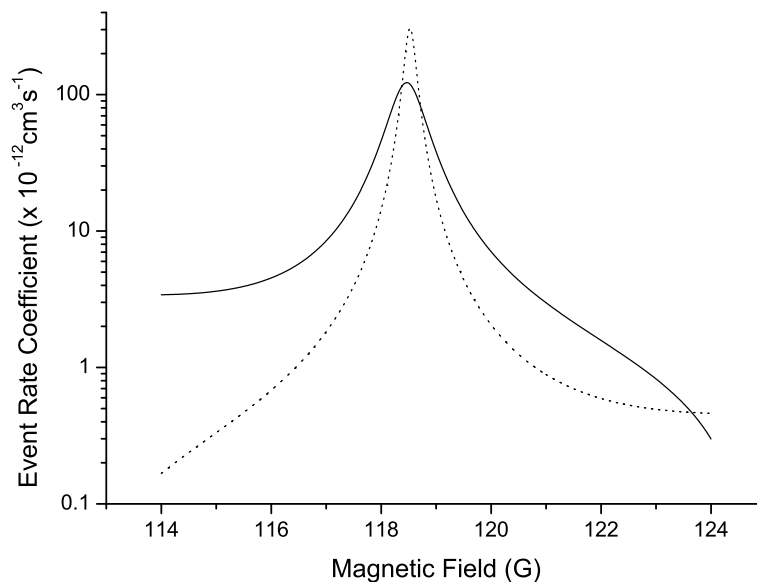


Figure 6.8: A comparison of the theoretical results obtained by including s - and d - waves (\cdots) and s -, d - and g -waves ($—$) in the basis of coupled channel calculations.

At a 114 G the inelastic collision rate associated with g -wave exit channels is nearly twice that of d -wave channels and therefore including the g -waves gives a

⁹The original theoretical data only included the s - and d -waves in the basis.

¹⁰Including the g -waves requires a 74 channel calculation for a single energy and magnetic field value.

value of the event rate coefficient that is nearly three times that of the calculation including s - and d -waves only. The width of the resonance also increases by approximately a factor of three.¹¹ The reason why including g -waves had not been observed to cause such a large effect previously was that fitting specific line shapes to resonances with such a high degree of precision had not been implemented prior to this work. It had been noted that the positions were shifted slightly when including g -waves but experimental error in the calibration of the magnetic field is larger than the shift observed in position.

As a result of this work, it has been shown that including g -waves as well as s - and d - waves in the basis of the coupled channel model is crucial to determine accurately the line shape of the d -wave resonance centred at 118.5 G. This is likely to be generally true for all d -wave resonances.

¹¹The widths of these resonances depend sensitively on the second-order spin-orbit operator.

Evaporation Results

This chapter is devoted to our attempts to condense caesium in the magnetically trappable $F = 3$, $m_F = -3$ state. A primary reason for our group to return to the magnetic trapping of caesium was provided by the more recent observation and precise measurement of over 25 Feshbach resonances in caesium in several internal states by the Stanford group [38]. These results accurately determined the scattering potentials for caesium. Inspection of the predicted collisional properties for the $(3, -3)$ state indicate that for some bias magnetic field values, caesium has favourable collisional properties for evaporative cooling, particularly if the magnetic trap geometry is chosen with care.

Initially, we investigated the evaporative cooling of caesium in a weak magnetic trap at high bias fields. A PSD within a factor of 10 of the onset of quantum degeneracy was attained (Section 7.1). The results suggested that the primary obstacle to the realization of BEC was the reduction in the cooling efficiency as the gas entered the hydrodynamic regime. The following experiments then focussed on minimizing the effect of the hydrodynamic regime: by making the evaporation three-dimensional (Section 7.2), and reducing the scattering length and the two-body inelastic losses by operating in a very weak trap at a high bias magnetic field (Section 7.3).

7.1 Initial Evaporative Cooling Attempt

Taking all the factors affecting the evaporation performance (discussed in Chapter 4) into consideration, the evaporation strategy was to operate in weak magnetic trapping potentials at high bias fields where the two-body inelastic collision rate is comparatively favourable [37]. It was decided to load the magnetic trap at ≈ 139 G as at this field the ratio of elastic to inelastic collisions was relatively high and all the resonances were at lower fields (Figure 1.1, Chapter 1). Operating at a magnetic field higher than the position of all the resonances gave us the option in future experiments of increasing the magnetic bias field and also weakening the trap without having to ramp the magnetic field through any resonances.¹ A current of 234 A is run through the baseball coil generating trap frequencies of 12.2 Hz radially and 5.3 Hz axially. The magnetic field is 139.19 G and the scattering length is predicted to be $2525 a_0$.

7.1.1 Experimental Procedure

Upon loading the magnetic trap an initial short high-powered stage of evaporation is performed in order to expel all atoms in magnetic substates other than $m_F = -3$ from the trap. Following this stage 2×10^8 atoms at approximately $40 \mu\text{K}$ remain in the magnetic trap. To evaporatively cool the atoms, individual stages are implemented to halve the temperature of the cloud while maximizing the number of remaining atoms.

The frequency of the rf surface as a function of time $f(t)$ for each evaporation stage was set to have the form of an exponential decay:

$$f(t) = f_{\text{base}} + (f_{\text{start}} - f_{\text{base}}) \times \exp\left(\frac{-t}{T}\right) \quad (7.1)$$

where

$$T = \frac{-t_{\text{stage}}}{\ln\left(\frac{f_{\text{stop}} - f_{\text{base}}}{f_{\text{start}} - f_{\text{base}}}\right)}$$

¹Figure 6.7, Chapter 6 illustrated the dependence of the amplitude of a resonance on collision energy. It is therefore advisable not to ramp cold atom clouds through resonances as this increases the inelastic loss rate in the cloud, leading to heating and atom loss.

Stage	f_{start} (MHz)	f_{stop} (MHz)	f_{base} (MHz)	t_{stage} (s)	Cumulative time (s)	rf amplit- ude (dBm)	Tempera- ture (nK)
1	55.000	54.200	50.000	15	15	-15	40000
2	54.200	52.250	50.000	60	75	-25	20000
3	52.250	51.670	50.500	40	115	-25	10000
4	51.670	51.125	50.500	25	140	-25	5000
5	51.125	50.785	50.200	17.5	157.5	-25	2500
6	50.785	50.538	50.200	11	168.5	-25	1050
7	50.538	50.405	50.200	7	175.5	-20	450
8	50.405	50.330	50.200	3	178.5	-20	250
9	50.330	50.270	50.200	2	180.5	-20	100
10	50.270	50.245	50.200	1.5	182	-20	50
11	50.245	50.227	50.200	1.25	183.25	-20	25

Table 7.1: The evaporation parameters used for the normal evaporation trajectory (bias magnetic field = 139.2 G).

The four parameters that specify the exponential curve (Equation 7.1) are the start frequency (f_{start}), the stop frequency (f_{stop}), the base frequency (f_{base}), and the duration of the ramp (t_{stage}). Generally, the start frequency is set to be the stop frequency of the previous ramp. For the initial ramp after loading the magnetic trap and for the first evaporation ramp at a different magnetic field, the start frequency is set to be the resonance frequency of atoms at the edge of the cloud. The stop frequency is set so that each evaporation stage cooled the atom cloud by roughly a factor of 2. The base frequency is normally set to be the resonance frequency of atoms at the centre of the cloud as this means that the evaporation occurs at constant η . The parameters that are varied in order to maximize the number of atoms remaining after each stage are: the base frequency (f_{base}), the duration of the stage (t_{stage}) and the power of the rf.² The set of optimized evaporation ramps is shown in Table 7.1 and plotted in Figure 7.1.

²When varying the base frequency, the duration of the stage, and the rf power, the stop frequency often needs to be altered in order to keep the final temperature equal to half the initial temperature.

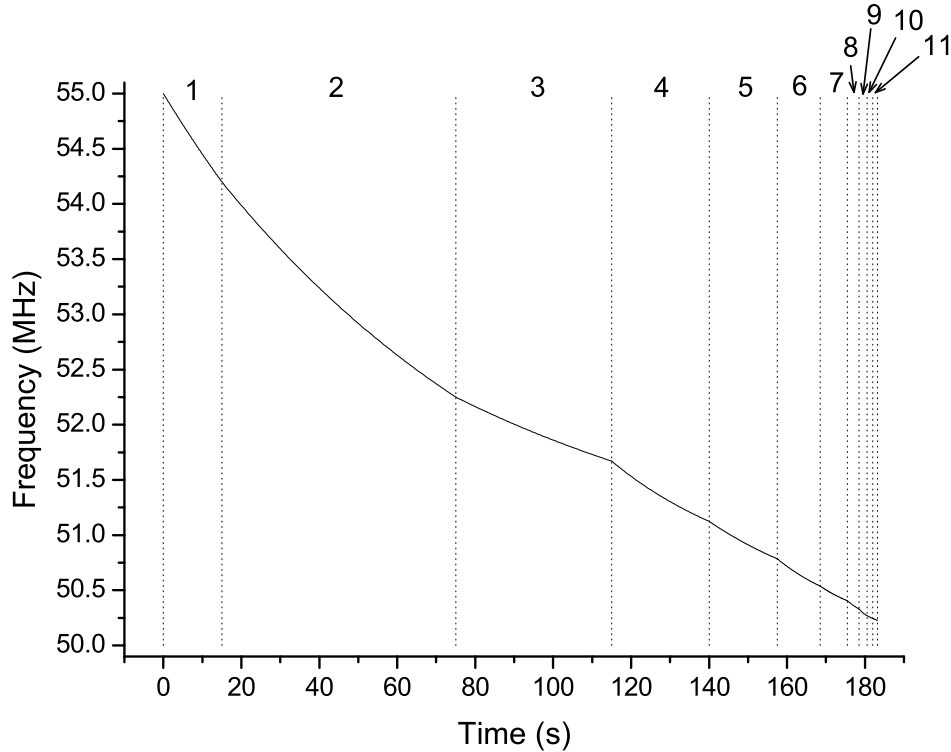


Figure 7.1: A plot of the radio-frequency as a function of time. (This is a plot of the values in Table 7.1.)

7.1.2 Results

A phase-space density of 0.1 could be reliably achieved, with approximately 1500 atoms cooled to a temperature of 8 nK. The evaporation trajectory, normalized phase-space density against number, is plotted in Figure 7.2. The ratio of the increase in PSD (P) to the fall in number (N) is the evaporative cooling efficiency denoted by γ :

$$\gamma = -\frac{d(\ln P)}{d(\ln N)} \quad (7.2)$$

γ is the logarithmic gradient of the trajectory in graphs of PSD against number of atoms.

Initially the evaporation efficiency (γ) is consistent with other alkali experiments despite our low densities and increased evaporation time (over 3 minutes). However, as the evaporation progresses the efficiency begins to decrease.

The lines (— and \cdots) on Figure 7.2 indicate the results of a simple rate equa-

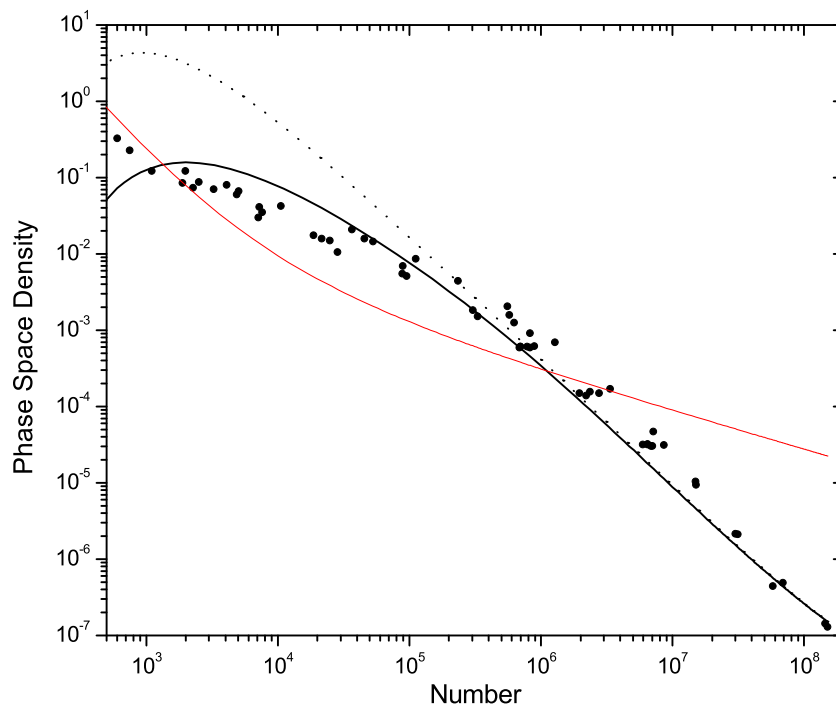


Figure 7.2: A plot of the normalized phase-space density against atom number at a field of 139.2 G. The results of a simple rate equation model are also shown, with (—) and without (\cdots) the hydrodynamic regime. The red curve corresponds to a collision rate of 12 Hz. Above this curve the cloud enters the hydrodynamic regime.

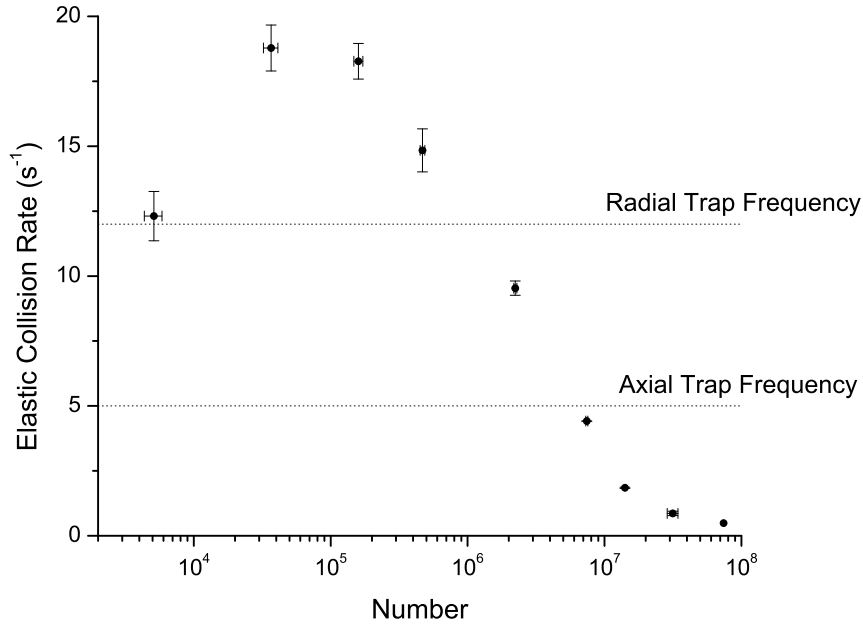


Figure 7.3: A plot of the elastic collision rate against number at a field of 139.2 G.

tion model of the evaporation [122]. The solid line includes the hydrodynamic behaviour by simply smoothly limiting the elastic collision rate to the value of the trap frequency. The evaporation parameters are then tuned so that the model approximately matches the evaporation trajectory. The hydrodynamic limit is then removed from the model while maintaining the same loss terms and evaporation parameters (dotted line). The dotted trajectory is essentially linear right up to the BEC transition, despite the large loss terms. The experimentally observed flattening of the trajectory thus appears to be associated with the hydrodynamic problem. This conclusion is supported by looking at the evolution of the elastic collision rate in the gas during evaporation (Figure 7.3). The collision rate increases slowly, becoming comparable to the radial trap frequency between 10^5 and 10^6 atoms, precisely where the slope efficiency of the evaporation starts to roll off.³

³Above the red curve on Figure 7.2 the cloud enters the hydrodynamic regime.

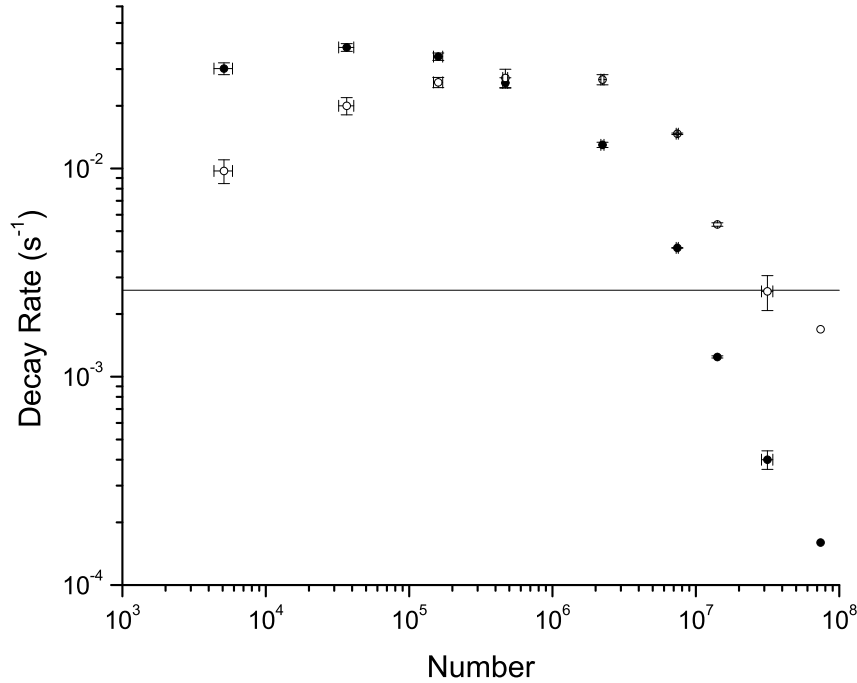


Figure 7.4: Individual decay rates during evaporation. The background loss rate (—), two-body decay (●) and three-body decay (○).

If we look at the ratio of the elastic collision rate to each of the individual loss rates (Figure 7.4) we see that initially the evaporation performance is limited by collisions with the background gas.⁴ When the number of atoms is between roughly 4×10^5 and 2×10^7 the loss rates are dominated by three-body collisions. As the density falls (Figure 7.5), the three-body losses are reduced due to their strong dependence on the density and the main loss process is two-body inelastic collisions.

⁴Most BEC experiments are limited by background gas collisions in the early stages of evaporation.

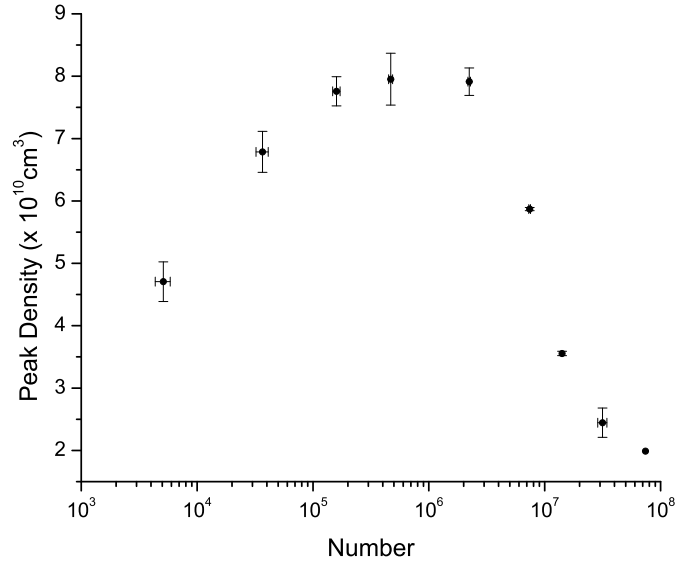


Figure 7.5: The evolution of the peak density in the atom cloud during evaporation.

7.2 Two-Frequency Evaporation

In Section 2.5.3, Chapter 2 the effect of gravity on the dimensionality of the evaporation surface is mentioned. If there were no loss processes in an atom cloud, one-dimensionality of the evaporation surface would just lead to longer evaporation times. However, in the presence of strong inelastic losses, 1D evaporation leads to a dramatic reduction in the evaporation efficiency. To study the effects of dimensionality a second evaporation surface positioned above the centre of the cloud was introduced. Figure 7.6 illustrates the positioning of the evaporation surfaces. The top evaporation surface is only in contact with a small area of the surface of the cloud, whereas the bottom evaporation surface is in full contact with the cloud. As the bottom evaporation surface is also large it should mean that any hot diffuse atoms are expelled completely from the trap. Even though the two-frequency evaporation setup is not fully two dimensional, the results should give an indication of the effect of dimensionality on the efficiency of the evaporation.

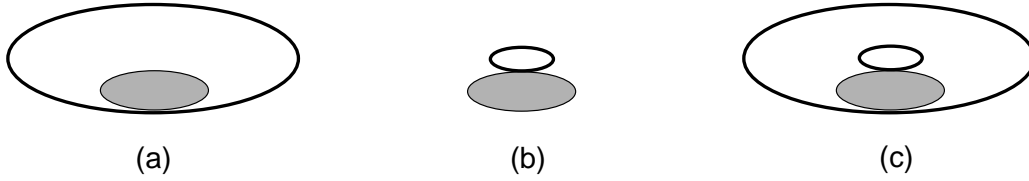


Figure 7.6: A simplified illustration of the evaporation surface: (a) cutting from below, (b) cutting from above, and (c) cutting from both directions.

7.2.1 Experimental Procedure and Results

For the bottom evaporation surface, the coupling of the rf into the glass cell is described in Section 5.1.8, Chapter 5. For the top evaporation surface a near identical setup⁵ was built and the second coil was positioned immediately above the glass cell because of space constraints. The two systems therefore allowed for independent control of the frequencies.

Temperature=170 nK					
Cutting Direction	f_{start} (MHz)	f_{stop} (MHz)	f_{base} (MHz)	t_{stage} (s)	rf amplitude (dBm)
Below	50.785	50.330	50.200	20	-25
Above	49.750	50.020	50.200	20	-10
Temperature=25 nK					
Cutting Direction	f_{start} (MHz)	f_{stop} (MHz)	f_{base} (MHz)	t_{stage} (s)	rf amplitude (dBm)
Below	50.785	50.245	50.200	25	-25
Above	49.750	50.075	50.200	25	-10

Table 7.2: Ramp details of the two-frequency evaporation studies. The results are given in Table 7.3. (The difference in the gain of the amplifiers is 15 dB. Therefore the rf surface power is the same for both cutting from above and below.)

To quantify the effect of two-frequency evaporation an extra stage of evaporation was set up to either cut from above, from below, or from both directions simultaneously. After the first five stages of evaporation (as given in Table 7.1) the centre and both edges of the cloud are determined. The evaporation ramps are then tailored so that the cutting into the cloud from both directions occurs at the

⁵The amplifier is a MiniCircuits amplifier (ZHL-3A with a gain of 24 dB).

same rate (equal η) and with the same power. The experiment was undertaken at two different temperatures: 170 nK and 25 nK. The ramp details are given in Table 7.2,⁶ and the experimental results are given in Table 7.3.

Temperature=170 nK				
Cutting Direction	Number ($\times 10^5$)	Temperature (nK)	PSD ($\times 10^{-3}$)	PSD Ratio
Below	1.72(5)	168(3)	2.63(6)	1
Both	1.19(10)	171(6)	1.70(6)	0.65
Above	1.56(6)	202(1)	1.35(7)	0.51
Temperature=25 nK				
Cutting Direction	Number ($\times 10^3$)	Temperature (nK)	PSD ($\times 10^{-3}$)	PSD Ratio
Below	7.43(1.11)	25.5(2.2)	35.6(3.5)	1
Both	8.18(0.13)	28.9(4)	24.4(6)	0.68
Above	31.8(1.84)	68.6(2.3)	7.1(4)	0.20

Table 7.3: Summary of two-frequency evaporation performance results for an atom cloud at a temperature of 170 nK and 25 nK.

The results clearly illustrate that while cutting from above alone yields poor evaporation performance, cutting from both above and below simultaneously is still not as efficient as cutting from below only. At first glance this is a surprise as it is always assumed that an increase in the dimensionality of the evaporation surfaces is beneficial. However, further consideration of the trapping geometry, inelastic two-body collisions and the hydrodynamic regime offer a possible explanation.

7.2.2 Discussion

There are two coupled contributory factors to the efficiency of two-frequency evaporation: the hydrodynamic regime and the non-linearity of the Zeeman splitting at high magnetic fields.

Let us firstly consider the non-linearity of the Zeeman effect. At high magnetic fields the non-linearity of the Zeeman effect lifts the degeneracy of the transition frequency between adjacent Zeeman sublevels. The frequency associated with

⁶The ramp details for cutting from above and below simultaneously are the same as the ramp details of cutting from above and below individually.

a particular m_F transition is then described by the Breit-Rabi equation (Equation 2.6, Chapter 2). The ordering of the transition frequencies is given by:

$$\omega_{-3 \rightarrow -2} > \omega_{-2 \rightarrow -1} > \omega_{-1 \rightarrow 0} > \omega_{0 \rightarrow +1} > \omega_{+1 \rightarrow +2} > \omega_{+2 \rightarrow +3} \quad (7.3)$$

The frequency of the transition from $m_F = -3$ to $m_F = -2$ is 50.148 MHz at 139 G, which is ≈ 550 kHz larger than the transition from $m_F = -2$ to $m_F = -1$. This means that atoms can be transferred from $m_F = -3$ to $m_F = -2$ but are unlikely to be transferred to other states. This can have an adverse effect on the evaporation efficiency and can completely interrupt the evaporation process [93].

One solution to this problem is to use hyperfine microwave evaporation as incorporated in the ^7Li experiments [3]. Another solution is to use many different frequencies tuned to each transition in order to transfer an atom to an un-trapped state. Boyer *et al.* condensed ^{87}Rb using a three-frequency rf knife [123]. They studied the evaporation using a three-frequency rf surface scheme which they simplified to one carrier and two sideband frequencies. This scheme works as ^{87}Rb has 5 magnetic sublevels therefore three frequencies can transfer an atom from $m_F = -2$ into an anti-trapped state. The disadvantage of the simplified scheme is that the two sideband frequencies will not exactly match the transition frequencies. However the scheme worked well at 56 G and resulted in the creation of a BEC where the standard one-frequency rf knife method had failed [123].

How does the hydrodynamic regime affect the two-frequency evaporation? Three different scenarios present themselves when considering cutting from above only:

- linear Zeeman effect
- non-linear Zeeman effect
- non-linear effect and large collision cross-section

The best case scenario involves the linear Zeeman effect. By applying the exact transition frequency an atom undergoes an adiabatic transition from the $(3, -3)$ state directly to the anti-trapped $(3, +3)$ state. The atom is therefore expelled from

the trap in random directions and does not necessarily pass through the cloud of atoms.

At high fields the non-linearity of the Zeeman effect has a large effect on the direction the un-trapped atoms are expelled from the trap. If the difference between the $m_F = -3 \leftrightarrow -2$ and $m_F = -2 \leftrightarrow -1$ transition frequency is large enough, the atoms only undergo Majorana transitions to the $m_F = -2$ state. The spatial position of the centre of the trap for $m_F = -2$ atoms is lower than $m_F = -3$ atoms, therefore the expelled atoms will fall through the cloud. Under normal conditions (i.e. many trap oscillations between collisions) it is unlikely that the $m_F = -2$ atoms would cause an observable detrimental effect.

The final scenario is the worst-case scenario and is the one that we interpret to be our situation. When trapped atoms that have a large collisions cross-section encounter the rf surface and undergo Majorana transitions to the $m_F = -2$ state they have an increased probability of colliding with $m_F = -3$ trapped atoms. This leads to a dramatic increase in the number of two-body inelastic collisions occurring in the trapped atom cloud. When cutting from below, the atoms fall down away from the cloud and therefore neither the non-linearity of the Zeeman transitions or the large collision cross-section has an effect. When cutting from above however, both of these effects must be considered as the atoms have an increased probability of only undergoing Majorana transitions to the $m_F = -2$ state and therefore falling through the cloud. Also, if the cloud has entered the hydrodynamic regime there is a high probability the un-trapped atom will collide with trapped atoms while falling through the cloud.

The next question is why cutting from above and below simultaneously is better than cutting from above only, but worse than cutting from below only?

When cutting from above, the $m_F = -2$ atoms fall through the cloud undergoing collisions with other atoms. However, if an $m_F = -2$ atom were to cross the cloud without undergoing another collision then it could oscillate past its trapped position (which is below the $m_F = -3$ trapped position as illustrated in Figure 7.7) and could travel back into the cloud thus increasing the chance of undergoing an

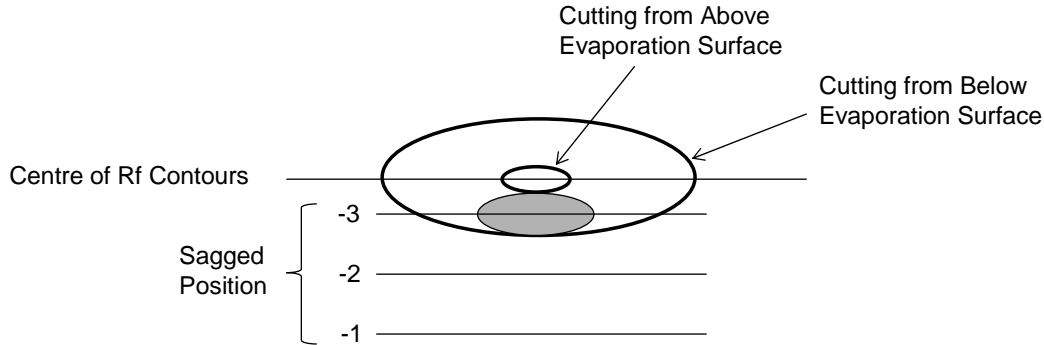


Figure 7.7: A simplified illustration of the two-frequency principle illustrating the sagged positions of each magnetically trappable m_F state.

inelastic collision with a cold trapped atom. However, if a surface where rf drives transitions at the bottom of the cloud is present, the $m_F = -2$ atom is unlikely to succeed in crossing the rf surface on the way out of the cloud and crossing it again on the way back into the cloud. Figure 7.7 illustrates the position of both rf surfaces and the positions of all magnetically trappable m_F states, taking account of sagging under gravity.

7.2.3 Heating

To test the hypothesis that hot atoms remain in the trap when cutting from above, a comparison of cutting from above and below was carried out by observing the resultant heating rate in the cloud. After completing evaporation stages 1 to 5 (Table 7.1) an evaporation stage incorporating cutting from above was implemented. An equivalent ramp cutting from below was also implemented as a control experiment.⁷ The ramp parameters for this stage are given in Table 7.4. Following completion of the extra stage, the rf was turned off and the magnetic trap hold duration (prior to imaging) was varied. The results are plotted in Figure 7.8.

The results of this experiment (as shown in Figure 7.8) support our hypothesis that cutting from above is less efficient than from below, and it is this effect that causes the resulting heating observed in the cloud. When atoms encounter the

⁷The same coil, amplifier and rf synthesizer was used for both cutting from above and from below.

Cutting Direction	f_{start} (MHz)	f_{stop} (MHz)	f_{base} (MHz)	t_{stage} (s)	rf amplitude (dBm)
Below	50.785	50.337	50.200	21	-25
Above	49.750	50.020	50.200	21	-10

Table 7.4: Details of the cutting from above and below ramp parameters. The results are given in Figure 7.8

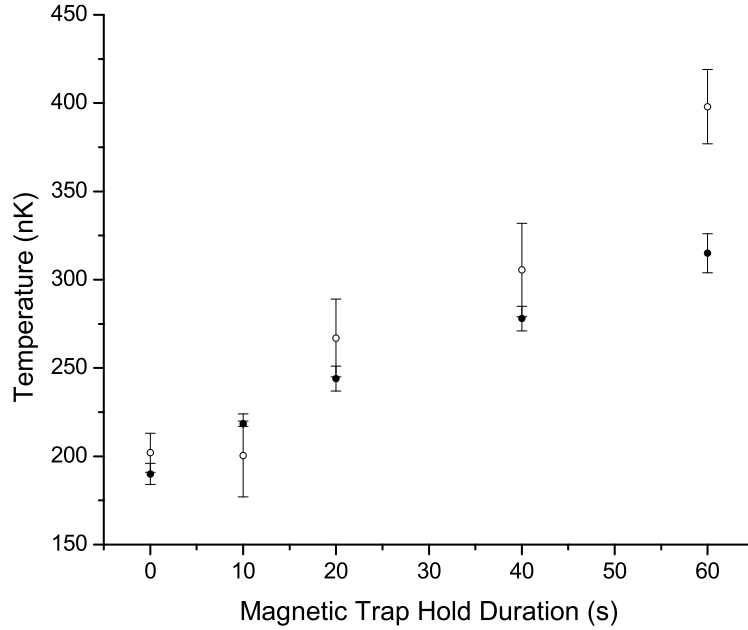


Figure 7.8: A plot of the axial temperature of the cloud against magnetic trap hold duration for cutting from above (○) and below (●) the cloud.

rf surface they undergo Majorana transitions to other states. If they undergo transitions to $m_F = -2, -1, \text{ and } 0$, the atoms will fall due to gravity, and if the evaporation surface is at the top of the cloud, the un-trapped atoms will fall through the cloud. The presence of other m_F states in the cloud causes an increase in the rate of two-body inelastic collisions, leading to atom loss and an increase in the temperature of the atom cloud.

7.3 Very Weak Trap

Following the failure to condense caesium at 139.2 G and the problems associated with introducing extra evaporation surfaces, it was decided to evaporate in a very weak trap and at a higher magnetic field: lowering the trap frequencies delays the onset of the hydrodynamic regime (Chapter 4), while at higher magnetic fields the two-body inelastic losses are lower (Figure 1.1, Chapter 1) which was the dominant loss process later on in the evaporation. Operating at high bias fields where the scattering length is lower, and reducing the trap frequencies and therefore the density would also further reduce the three-body inelastic loss rate in the cloud.

7.3.1 Experimental Procedure

To weaken the magnetic trapping potential the baseball current was reduced (Equation 2.13, Chapter 2). To increase the bias magnetic field, current was run through the bias coils, adding to the bias magnetic field produced by the baseball coil. Numerical calculations of the trapping potentials suggested that that the lower limit for the trap frequencies were ≈ 4 Hz.⁸ There is a further constraint on the radial trapping frequency. The amount of sag is inversely proportional to the square of the radial trapping frequency (Equation 2.15, Chapter 2), therefore weakening the trap too much causes the atom cloud to hit the bottom of the glass cell.

The baseball current was reduced from 234 A to 209.83 A and the bias current set to be 232.25 A.⁹ The magnetic field was 510.545(55) G and the measured trap frequencies at this field were: 4.193(18) Hz radially, and 3.952(16) Hz axially.

The first five stages in the original evaporation strategy have comparable efficiencies to other BEC experiments, therefore it was decided to continue loading the magnetic trap at 139.2 G (Labview Baseball Voltage = -3.957 V) and performing stages 1 through 5 prior to moving to the new field. For the early stages of

⁸If the trap frequencies were reduced further then the potential would no longer trap the atoms.

⁹The bias current was increased incrementally until a loss in atom number was observed corresponding to the atom cloud hitting the bottom of the cell. The bias current was then set to be a value slightly lower than the threshold value.

Stage	f_{start} (MHz)	f_{stop} (MHz)	f_{base} (MHz)	t_{stage} (s)	Cumulative time (s)	rf amplitude (dBm)
6	198.400	197.450	196.500	30	30	-30
7	197.450	197.150	196.500	21	51	-30
8	197.150	196.925	196.500	18	69	-30
9	196.925	196.750	196.500	16	85	-30
10	196.750	196.690	196.500	16	101	-30
11	196.690	196.580	196.500	25	126	-30

Table 7.5: Summary of evaporation parameters used in the weak trap, high-field evaporation. The evaporation was performed at a magnetic field of 511 G and the axial and radial trapping frequencies were 4.0 Hz and 4.2 Hz respectively.

evaporation it is crucial to operate in a relatively tight trap as the background loss rate is the dominant loss mechanism. Following evaporation stage 5 at the original field, the baseball current was ramped to 209.83 A (Labview Baseball Voltage = -3.500 V) and bias current was turned on and increased to a current of 232.25 A (Labview Bias Voltage = -4.000 V) in 750 ms.¹⁰

The evaporation at the new field proceeds as described previously: the temperature is halved while maximizing the number of atoms remaining. The ramp details for this new field are given in Table 7.5. These stages were performed at a lower rf amplitude so that the evaporation surface was shallower enabling more precise cutting.

The atom cloud could not be imaged at the weak field as the position of the cloud was below the incident position of the probe beam. It was not advisable to move the probe beam as not only was the position of the atom cloud very close to the bottom of the glass cell which would lead to diffraction effects and reduce the resolution of the imaging system, the probe laser was also used to optically pump the atoms into the $(3, -3)$ prior to loading the magnetic trap. As we were continuing to load the magnetic trap at 139 G moving the probe beam would have led to a reduction in efficiency of the optical pumping. The atom cloud was therefore imaged by ramping the magnetic field back to 139 G¹¹ and imaging at

¹⁰The ramp duration is determined by studying the heating and number loss following different ramp durations.

¹¹The magnetic field was ramped adiabatically in order to preserve the PSD in the cloud.

the original field.

It was possible to image the atoms without ramping back to the original field by turning the bias current off and changing the baseball current to 234 A rapidly. This caused a deformation of the trapping potential and an upwards velocity was imparted to the atoms. When the atom cloud travelled back into the field of view it was then imaged. The disadvantage of this method is that information about the spatial size of the cloud in the weak trap is lost and therefore this method cannot be used independently. We used both methods in conjunction – we used the widths obtained from the data taken when the magnetic field was ramped back to its original value, but the number obtained from the data when the magnetic field was not ramped back.

7.3.2 Data Analysis

Of course when we image the cloud of atoms that have been evaporated at a high bias field and weak trap we only obtain information about the collision properties in the gas at the imaged field. However, by consideration of the scaling laws of adiabatic compression we can extract the necessary scaling factors in order to obtain accurate information about the collision rates in the atom cloud in the weak trapping potential.

During adiabatic compression ω/T is a constant (Chapter 4) and therefore we can state:

$$\frac{T'}{T} = \frac{\omega'}{\omega} \quad (7.4)$$

$$= \frac{\omega_r'^2 \omega_z'}{\omega_r^2 \omega_z} \quad (7.5)$$

where the original temperature and geometrical mean of the trap frequencies are denoted by T and ω respectively, and the temperature and geometrical mean of the trap frequencies following adiabatic compression by T' and ω' respectively. The elastic collision rate (Equation 4.1, Chapter 4) can be expressed as follows:

$$\Gamma_{\text{elastic}} = \frac{N\omega^3 m\sigma}{\pi^2 k_B T} \quad (7.6)$$

During adiabatic compression ω/T is constant and therefore the ratio of the elastic collision rates is given by:

$$\frac{\Gamma'_{\text{elastic}}}{\Gamma_{\text{elastic}}} = \left(\frac{\omega'}{\omega}\right)^2 \frac{\sigma'}{\sigma} \quad (7.7)$$

When the elastic collision cross-section is independent of temperature Equation 7.7 becomes trivial. The elastic collision cross-section however, does change because of the change in scattering length (from $2525 a_0$ to $1525 a_0$) and because of the change in temperature.¹² The observed elastic collision rate must therefore be modified accordingly in order to determine the correct collision rate. The cross-section is given by Equation 3.23, Chapter 3 and restated here for completeness:

$$\sigma = \frac{8\pi a^2}{1 + k^2 a^2}$$

The ratio of elastic collision rates during adiabatic compression is described by Equation 7.8:

$$\frac{\Gamma'_{\text{elastic}}}{\Gamma_{\text{elastic}}} = \left(\frac{\omega'}{\omega}\right)^2 \left(\frac{a'}{a}\right)^2 \frac{1 + (ka)^2}{1 + (k'a')^2} \quad (7.8)$$

		Normal Trap 139 G	Weak Trap 511 G
Radial frequency	ω_r	$2\pi \times 12.194$	$2\pi \times 4.193$
Axial frequency	ω_z	$2\pi \times 5.302$	$2\pi \times 3.952$
Scattering Length	a	$2525 a_0$	$1525 a_0$

Table 7.6: Summary of the trap parameters and scattering length in the normal trap (at 139 G) and in the weak trap (at 511 G).

Using the values given in Table 7.6 and the fact that ω/T is a constant during adiabatic compression it is possible to obtain an expression for the ratio of the elastic collision rates:

$$\frac{\Gamma'_{\text{elastic}}}{\Gamma_{\text{elastic}}} = \frac{0.0722 (1 + 25.1114 T)}{1 + 4.07629 T} \quad (7.9)$$

where T is the temperature of the cloud at the imaged field.

¹²The collisional cross-section in caesium is temperature dependent.

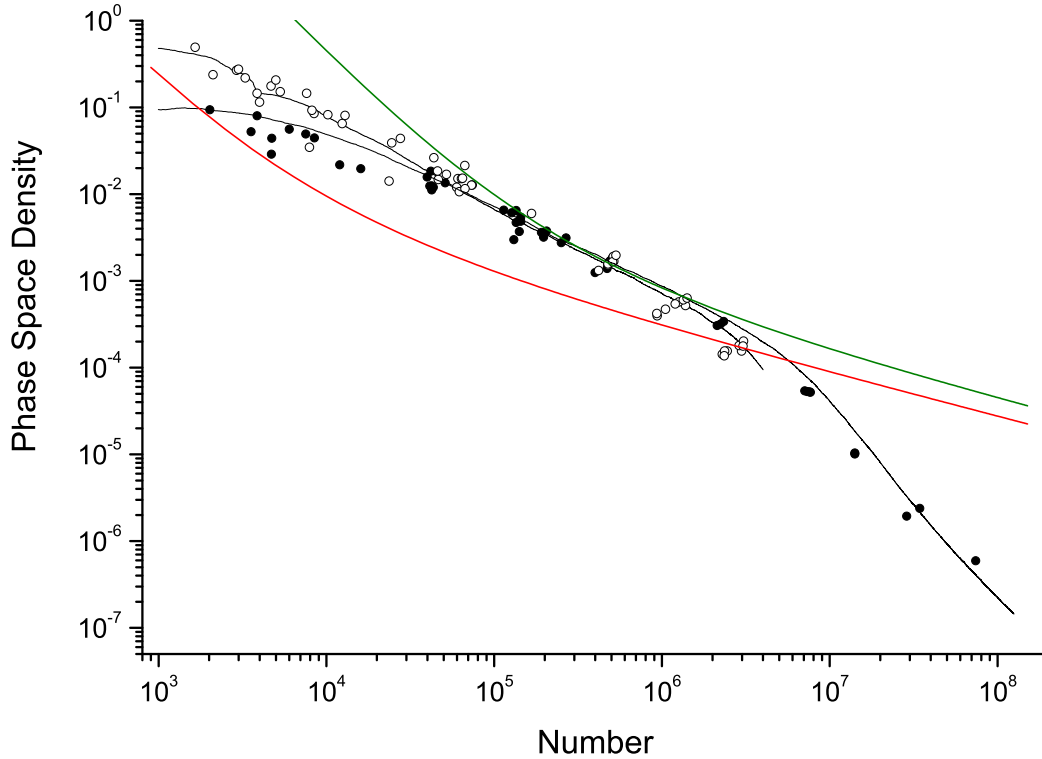


Figure 7.9: Evaporation trajectory for ^{133}Cs atoms trapped in $12 \times 12 \times 5$ Hz (\bullet) and $4 \times 4 \times 4$ Hz (\circ) magnetic traps. The solid curves show the results of the simulation [52] for 180s of evaporative cooling. The red and green curves correspond to a collision rate of 12 Hz ($12 \times 12 \times 5$ Hz trap) and 4 Hz ($4 \times 4 \times 4$ Hz trap) respectively. Above these curves the cloud enters the hydrodynamic regime

7.3.3 Results

To compare accurately the original evaporation trajectory and the very weak trap results,¹³ the data points are taken alternately from the original evaporation ramps (Table 7.1) and the new evaporation ramps (Table 7.5). The data is plotted in Figure 7.9.

Weakening the trap clearly improves the end PSD attained by a factor of three, however there is still a roll-off in the performance of the evaporation. Figure 7.10 illustrates the evolution of the elastic collision rate during the evaporation. The flattening of the trajectory in Figure 7.9 happens later on in the evaporation for a

¹³The original evaporation trajectory (Figure 7.2) was taken a year previously and therefore it was decided to repeat the measurements in order to obtain an accurate indication of the weak trap evaporation performance.

weak trap (compared to the original evaporation trajectory in Figure 7.2), but we are still unable to reach a PSD of 1.

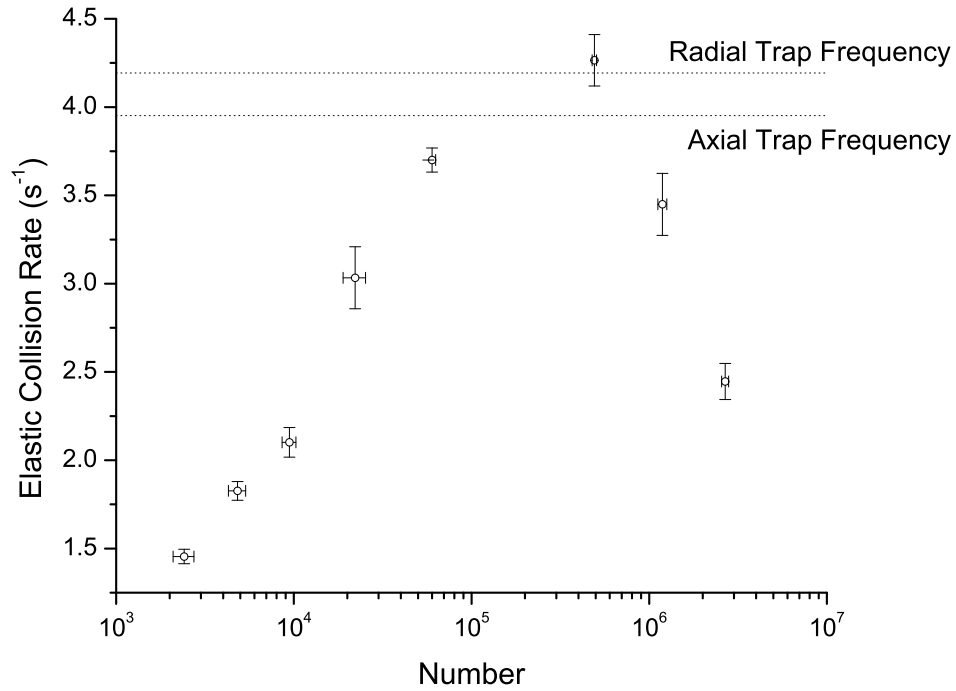


Figure 7.10: A plot of the elastic collision rate against number at a field of 510.5 G. (The collision rate was scaled as described in Section 7.3.2.)

7.3.4 Discussion

Following the failure to condense caesium at 139 G and 510 G it was decided to try and simulate the evaporation and determine what, if any, parameter could be varied in order to improve the evaporation performance [124].¹⁴ In Figure 7.9, the simulation accurately reproduces the experimental results. Both the experimental data and the simulation result show that the evaporation performance is slightly improved if the trap frequencies are weakened. Also, the results show a decrease in the efficiency of the evaporation as the cloud enters the hydrodynamic regime.

To investigate the detrimental effect of entering the hydrodynamic regime on the evaporation performance, simulations were performed on atom clouds with different initial phase-space densities. Even when the initial PSD (after stage 1) was varied by a factor of 10, the evaporative cooling curves all cross one another when the cloud enters the hydrodynamic regime (Figure 4 (b) in Reference [52]).

The duration of the evaporation was varied experimentally and the evaporation trajectory simulated in order to determine whether the duration was optimum. To vary the total duration of the evaporation, the individual ramp durations were scaled accordingly.¹⁵ Figure 7.11 illustrates the result of varying the evaporation time experimentally and theoretically. The evaporation performance is not very sensitive to the evaporation duration, although there is an optimum value (in the simulation) of around 150 s in a $12 \times 12 \times 5$ Hz trap.

Another important factor in the evaporation performance is the dimensionality of the evaporation surface. The simulation results for one-dimensional cutting from one side of the cloud, one-dimensional cutting from both sides of the cloud¹⁶ and three-dimensional cutting in a 12 Hz spherical trap were compared. The results suggested that BEC could be realized with three-dimensional cutting [52].

¹⁴The simulation was performed by Z.-Y. Ma and the full results are published in Reference [52], while the relevant simulations for the experimental results are included in Figure 7.9 and 7.11.

¹⁵Ramp 1 was not modified as its function is to remove other m_F states, and is therefore not part of the evaporation.

¹⁶Equivalent situation as the experimental setup explained in Section 7.2.

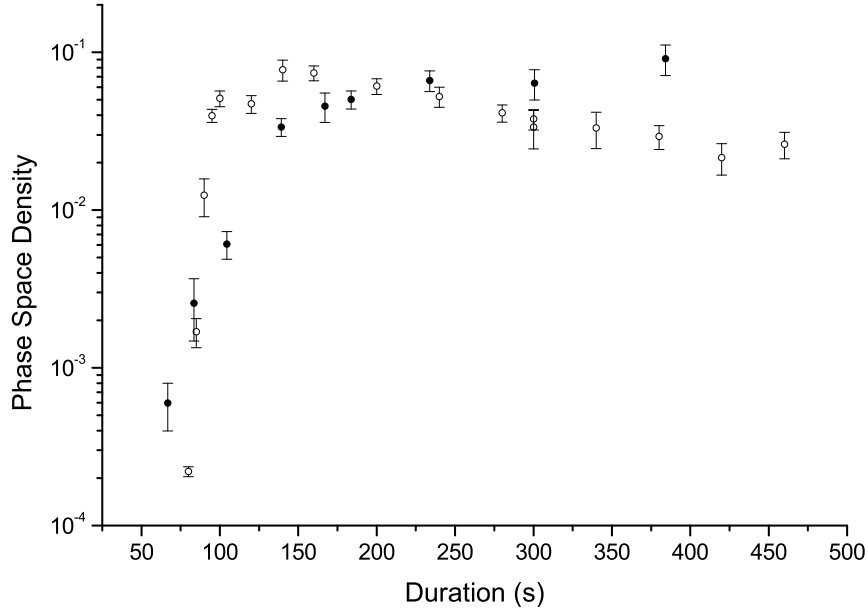


Figure 7.11: The final phase space density as a function of the evaporation time in a $12 \times 12 \times 5$ Hz trap: experiment (●) and simulation (○)

We achieved a PSD of 0.3 which is a factor of 10 higher than previous Cs experiments in the magnetically trappable states (Table 4.2, Chapter 4). This increase was achieved by careful consideration of the ratio of elastic to inelastic collisions in various loss regimes and by delaying the onset of the hydrodynamic regime by operating in weak magnetic traps.

The three main factors that conspire to decrease the efficiency of the evaporation and ultimately the failure to condense caesium in the magnetically trappable $F = 3, m_F = -3$ state are: the onset of the hydrodynamic regime, the high rate of two-body inelastic losses and the dimensionality of the evaporation surface.

Conclusion

We have evaporatively cooled a magnetically trapped sample of caesium atoms in the $F = 3, m_F = -3$ state to a PSD within a factor of four of the BEC transition, which is at least ten times higher than previous magnetically trapped caesium experiments. We have shown that previous experiments did not work because the cloud of trapped atoms was in the hydrodynamic regime. The increase in the PSD that we achieved was due to careful consideration of the optimum conditions for evaporative cooling. We operated with a weak magnetic trap at high magnetic fields to reduce the two-body inelastic loss rates and delay the onset of the hydrodynamic regime in the evaporative cooling stage.

A numerical simulation of evaporative cooling was developed that accurately reproduced our experimental observations [124]. The simulation results indicated that the main obstacle to the realization of quantum degeneracy in the $(3, -3)$ state was the reduction in the evaporative cooling efficiency in the hydrodynamic regime.

A lower dimensionality of the evaporation surface was also detrimental to the cooling efficiency. The effects of the non-linearity of the Zeeman effect and the presence of extra evaporation surfaces was studied and it was observed that at high magnetic fields and when the cutting surface is above the atom cloud the evaporation is less efficient.

During the course of this work we have characterized the two-body losses at magnetic fields ranging from approximately 105 to 150 G, confirming the positions of three previously identified resonances [38] and the validity of theoretical predictions [37]. We have also studied the dependence of two-body inelastic loss rates on the collisional energy. The resonance centred at 118.5 G was plotted at three different temperatures and the widths, position, peak and background K_2 compared for each temperature. The results indicate that with increasing collision energy the two-body loss rate decreases both on and off-resonance. The position of the resonance occurs at higher fields for decreasing collisional energy. The results are in good agreement with the theoretical predictions [50].

The importance of including g -waves in the basis of the theoretical analysis was realized during the course of this work. Previously it was thought that including s and d exit channels in d -wave resonance calculations was sufficient to accurately determine the shape and position of the resonance. Following our work in fitting a specific shape to a resonance with a high level of precision, theoretical calculations were undertaken by Julianne at NIST which included the g -wave exit channels for the d -symmetry resonance level. He discovered that including the g -waves in the analysis shifted the position of the resonance slightly, changed the K_2 value both on and off-resonance and significantly changed the width of the resonance.

8.1 Outlook

Is it possible to condense caesium in the $(3, -3)$ state? By analyzing the limitations of the present experiment there are a few changes that could be made to improve the evaporative cooling efficiency.

Reference [52] states that condensing caesium in the magnetically trappable state is possible if the evaporation is three dimensional. However, in order to avoid the hydrodynamic regime, evaporation must take place in weak magnetic trap and therefore gravity will always make the evaporation one-dimensional. One improvement would be to operate in a pancake shape trap (very tight in the vertical direction and weak in the other two directions). This would not only reduce the

gravitational sag but the evaporation surface would be very large and would be in full contact with the bottom of the cloud thus reducing the hydrodynamic problem. Unfortunately it is impossible to generate a weak trapping potential in two directions while maintaining a strongly confining potential in the third direction in a baseball trap. Varying the current to the baseball coil changes all three trapping frequencies. The bias coils permit modification of the trapping frequencies but once again all three directions are inter-dependent. The only trap that allows complete independent control of each trapping frequency is the cloverleaf trap [83]. Also the design of the cloverleaf allows significantly better optical access¹ to the trapped atoms than that available with the baseball and bias coils.

Such modifications would improve the efficiency of the evaporative cooling, but it is unknown as to whether this factor would be enough to observe BEC.

BEC has been achieved in caesium in the $(3, +3)$ state and the advantages of operating in this state are obvious. The greatest versatility to control BEC interactions exist as there is a large broad Feshbach resonance between 0 and 50 G where the scattering length changes from negative to positive. The scattering length is zero at 17 G leading to the possibility of study of non-interacting condensates. There exists a narrow Feshbach resonance at a higher magnetic field (48 G) which allows for the creation of molecules. Both of these resonances occur at magnetic fields that are experimentally easy to access. Also in the Innsbruck experiment the bias magnetic field can be changed without altering the trap frequencies (Appendix A).

Why therefore would it be of benefit to work with caesium in the $(3, -3)$ state? There are many experiments involving cold atoms, but not necessarily a BEC, that could be carried out using a caesium atom cloud.

The hydrodynamic regime is an area of collisional physics that is not very well understood. Caesium is well suited to hydrodynamic regime studies because of its large scattering length, therefore the entry of the cloud into the hydrodynamic regime is almost unavoidable.

¹The cloverleaf trap allows 360° optical access.

To observe quantum tunnelling effects a BEC is normally loaded into an optical lattice. However, the temperatures that can be attained by evaporatively cooling caesium is much lower than the critical temperatures for all other BEC experiments. It could therefore be interesting to load an extremely cold caesium atom cloud (less than 50 nK) into an optical lattice and compare the resulting effects with a BEC loaded into an equivalent lattice.

The scattering properties of Cs in many internal states has been studied in detail [37, 38], and both the $(3, -3)$ and the $(3, +3)$ state possess collisional features that are not only experimentally but also theoretically interesting. Both states contain Feshbach resonances that are experimentally accessible. A wealth of physics has opened up due to the ability to use Feshbach resonances to tune inter-atomic interactions: molecules are created, collision gates in quantum computing manipulated, and the collapse and revival of condensates studied. Caesium is one of the most versatile alkali metals and its cold collision properties holds great prospects for future research in the field of quantum gases.

Bose-Einstein Condensation in Caesium

A Bose-Einstein condensate of caesium atoms was created on the 5th of October, 2002 in Innsbruck [12]. Grimm *et al.* achieved BEC by evaporative cooling using optical trapping techniques. This appendix is a summary of their experiment and illustrates how they achieved BEC and the difficulties they overcame along the way.

The $F = 3$, $m_F = +3$ state in caesium is the lowest internal state and therefore the absence of internal energy leads to full suppression of inelastic two-body loss. Therefore the important loss rates in the trap are due to background gas collisions, three-body collisions, and photon scattering from the dipole trap.¹

A.1 Experimental Setup

The initial experimental procedure is similar to other alkali metal experiments. Following cooling in the MOT and an optical molasses stage, approximately 10^8 atoms at a temperature of $10 \mu\text{K}$ are loaded into an optical lattice. Raman sideband cooling is then implemented to both cool and polarize the atoms [40]. 2×10^7 atoms at a temperature of $1 \mu\text{K}$ are then loaded into an optical trap by adiabatic release of the atoms from the optical lattice.

¹The large laser detuning from resonance of the CO_2 beams results in a negligibly small photon scattering rate.

The optical trap is based on a crossed-beam CO₂ trap. Each beam is generated by a 100 W CO₂ laser and the beams cross at 90° (Figure A.1 (a)). A magnetic levitation field to support the atoms against gravity is essential as the optical forces in the CO₂ trap are much lower than the gravitational force. A levitation trap (LEVT) is created by generating a magnetic gradient using a pair of coils in an anti-Helmholtz configuration [1, 41]. A combination of the optical trap and the LEVT results in a shallow large volume trap which can be loaded with a large number of atoms.² The effective volume is approximately 1 mm³, the trap depth is 10 μK, and the geometrical mean of the trap frequencies is 14 Hz.

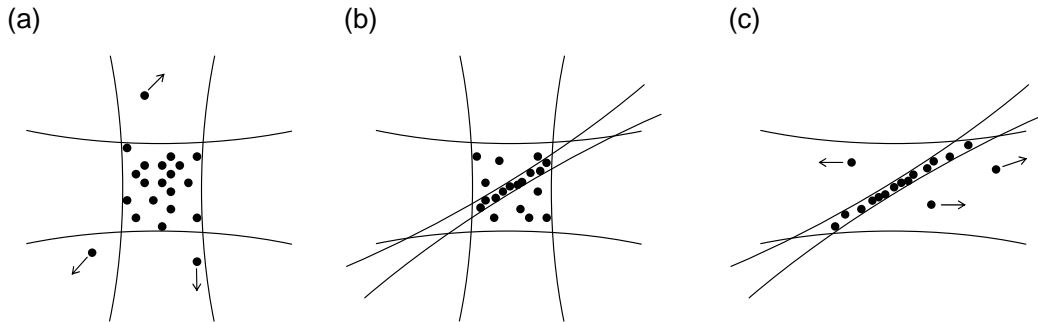


Figure A.1: An illustration of the setup of the laser beams in the Innsbruck experiment: (a) the crossed-beam CO₂ trap, (b) loading the “dimple” trap, and (c) evaporation in the “dimple” trap. This figure is modified from Reference [12].

An extra pair of coils in a Helmholtz arrangement is used to tune the bias magnetic field. This results in the bias magnetic field value being freely adjustable without altering the trap frequencies, and therefore B_0 is a free parameter.

A.2 Evaporation

Initially, evaporation proceeds on loading the CO₂ trap.³ For 10 s, atoms are evaporated out of the trap at a constant trap depth, resulting in a cloud of 3×10^6

²The LEVT cancels gravity for the (3,+3) state and as the optical trapping forces are so weak no other m_F states are supported against gravity. This results in a pure (3,+3) atom cloud in the optical trap.

³On loading the CO₂ trap the scattering length is chosen to be $1200 a_0$ (at 75 G) in order to obtain a sufficient collision rate in the atom cloud.

atoms at a temperature of $1\ \mu\text{K}$ ($\text{PSD} \approx 10^{-3}$). Forced rf evaporation is then implemented, but because of the vertical levitation gradient the rf surface is only resonant with atoms at the bottom of the cloud leading to one-dimensional evaporation. They achieved a PSD of 0.3 with 2500 atoms remaining.

In their initial work the achievement of Bose-condensation was prevented by three-body recombination. Theory predicts that the three-body loss rate scales as a^4 [125] and a large scattering length therefore leads to a large loss in number and heating. In three-body recombination a diatomic molecule forms from two of the atoms and the third one takes away the binding energy of the molecule. In a deep trap this third atom remains in the trap causing heating. A shallower trap allows the third atom to escape. Grimm *et al.* then implemented three improvements: optimization of the trap depth and the scattering length, implementing efficient three-dimensional evaporation, and avoiding the hydrodynamic regime.

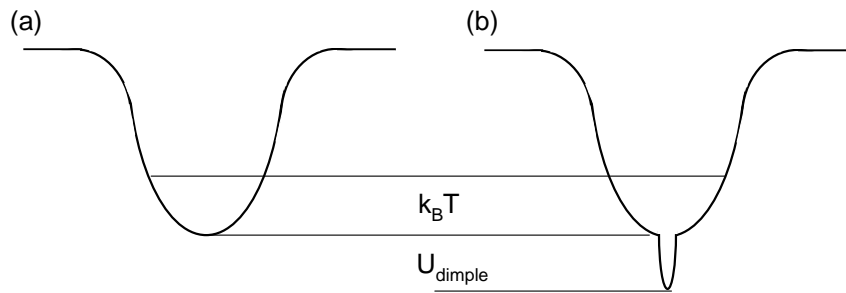


Figure A.2: An illustration of the principle of the “dimple” trap.

Deforming the trapping potential can result in an increase in PSD without a loss in number [126]. Grimm *et al.* created a narrow and deep potential well [127] in the center of the CO_2 trap by focussing a beam of wavelength 1064 nm, produced by an Ytterbium fibre laser, into the sample. Figure A.1 (b) illustrates the positioning of the 1064 nm beam in the CO_2 , and Figure A.2 illustrates the resulting potential. The adiabatically deformed potential (called the “dimple” trap) results in a large gain in PSD as the density in the trap is greatly increased.⁴ The new PSD (P) is

⁴The temperature in the atom cloud does increase slightly but the effect is negligible compared to the increase in the density.

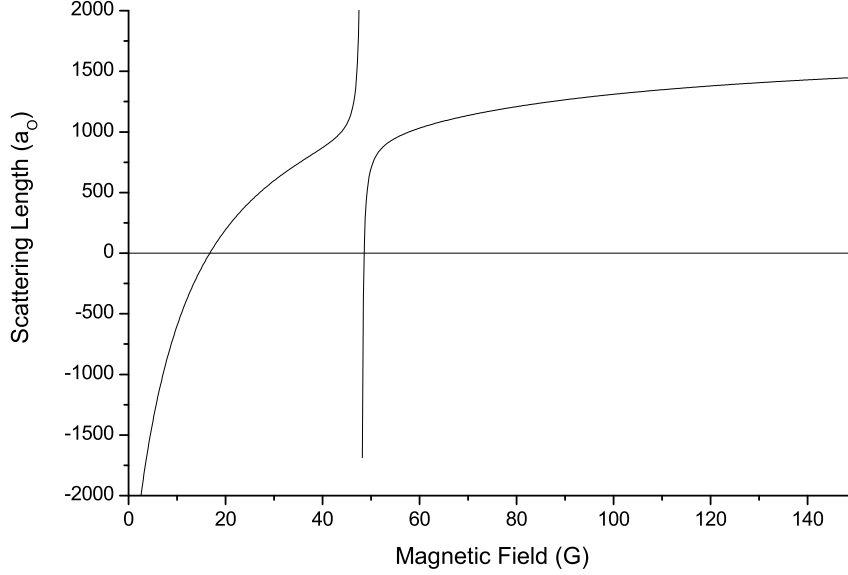


Figure A.3: The scattering length as a function of magnetic field for the (3, +3) state in caesium. The resonances are situated at 17 G and 48 G.

related to the old PSD (P_0) by the following expression:

$$P \approx P_0 \exp\left(\frac{U_{\text{dimple}}}{k_B T}\right)$$

where U_{dimple} is the potential depth of the dimple. The “dimple” trap allows for better initial conditions prior to evaporation, a higher PSD and density, and also allows for three-dimensional evaporation.

One of the CO₂ beams is then turned off (Figure A.1 (c)) and a dense sample ($\approx 10^{12} \text{ cm}^{-3}$) of 3×10^5 Cs atoms remain trapped in the combined field of the 1064 nm beam and the CO₂ laser beam. The result is a cigar shaped cloud with tight radial confinement provided by the 1064 nm beam and the axial confinement provided by the remaining CO₂ laser. The radial and axial trapping frequencies are 320 Hz and 6 Hz respectively.

Evaporation begins with 3×10^5 atoms at a temperature of $1.5 \mu\text{K}$ ($\text{PSD} \approx 10^{-2}$) and the power of the 1064 nm beam is 90 mW. Forced evaporative cooling is achieved by ramping down the power of the 1064 nm laser beam. At a power of 1 mW and after 17 s of evaporation a pure condensate is observed consisting of 16 000 atoms.

The creation of a BEC of caesium was achieved at a bias magnetic field of 23 G ($a = 300 a_0$). It was only possible to condense at magnetic fields between 21 and 25 G. Below 21 G the elastic collision cross-section was too small, whereas for magnetic fields greater than 25 G the increase in scattering length leads to an increase in three-body collisions and the entry of the cloud into the hydrodynamic regime. Figure A.3 illustrates the resonance structure of the (3,+3) state in caesium.

A.3 Comparison

Even though the Oxford and Innsbruck experiments operate in different traps and magnetic states, both face similar problems. One-dimensional evaporation is an inherent problem in both traps and the temperature dependence of the elastic collisional cross-section leads to an increase in the rethermalization time. The main difference between both experiments is the magnetic states that are trapped. Innsbruck trap the (3, +3) state which is the stable against two-body inelastic collisions, whereas in Oxford the (3, -3) state is trapped magnetically. Their dominant collisions are three-body recombination whereas our dominant loss process is due to two-body inelastic collisions.

Figure A.4 illustrates our results and the experimental results of the caesium experiment at Innsbruck. Their original results with one-dimensional evaporation are comparable to our results, and it is only when they implemented efficient three-dimensional evaporation that they succeeded in Bose-condensing Cs.⁵

⁵In the summer of 2002 there were many conferences at which both experiments were represented. This led to many collaborative discussions about the problems in each experiment. We were already trying to implement a three-dimensional evaporation scheme. It is difficult to implement three-dimensional evaporation successfully in a magnetic trap, however it was possible in an optical trap to implement the “dimple” trap to allow three-dimensional evaporation.

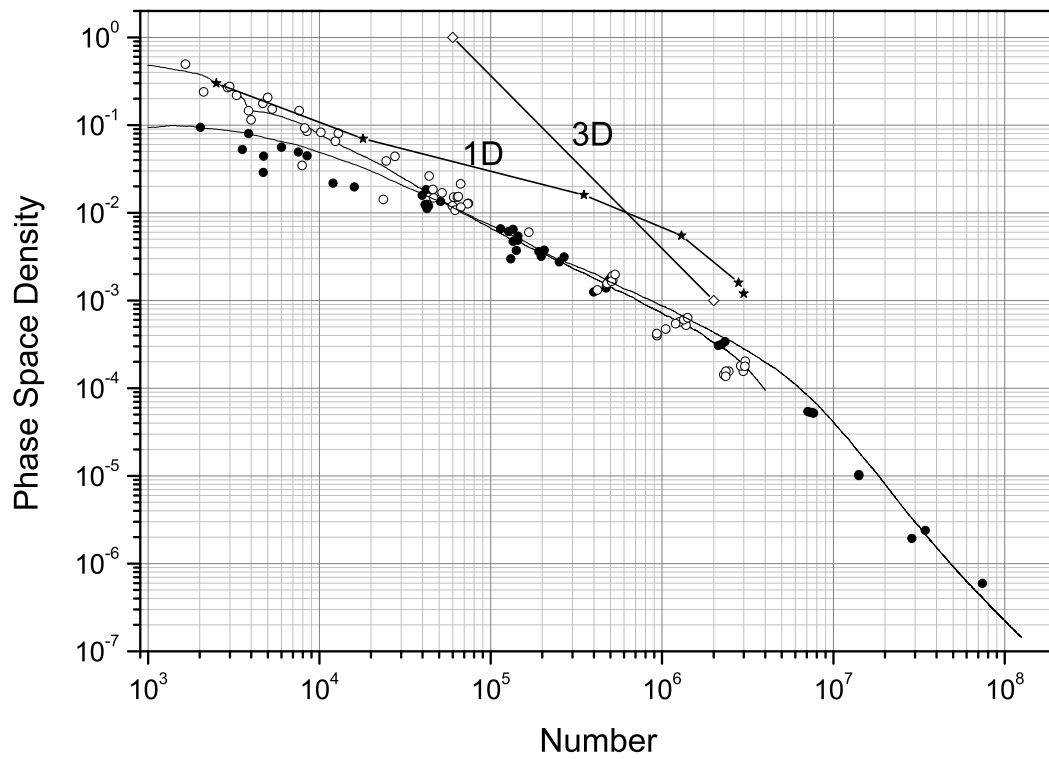


Figure A.4: The evaporation trajectory for ^{133}Cs atoms in our magnetic trap at Oxford (from Figure 7.9) and the optical trap at Innsbruck. The Innsbruck results are denoted by \star (one-dimensional evaporation) and \diamond (three-dimensional evaporation).

Experimental Equipment Details

B.1 Computer Control Boards

The computer boards are from ‘National Instruments’. The control computer contains three different boards (see below) which are all controlled by the Labview software program.

PCI-GPIB A high-performance GPIB interface. The rf values from the Labview control program to the frequency-generator are transferred via GPIB.

PCI-6713 A 12-Bit, 1 MS/s per channel analog output board. It consists of 8 analogue channels and 8 digital channels. The analogue channels are used for the magnetic trap Labview input voltages (Figure 5.14, Chapter 5).

PCI-DIO-32HS A high-speed pattern I/O and handshaking board. This board consists of 32 digital outputs and it generates the TTL signals required to control the experiment.

B.2 Electronic Equipment Details

Table B.1 contains all the names and part numbers of the circuits made in Central Electronics, Physics Department, Oxford University.

Circuit Name	Central Electronics Number
Voltage Reference Switching Unit	EW1288
Photodiode Amplifier	EW1287
Double Photodiode Amplifier	EW1302
Voltage Level Multiplexer	no part number
Shutter Driver	EW1301
Magnetic Trap - Reference Voltage	EW1285
250 A Coil Driver, Main Feedback Board	EW1282
Current Source. 5A Max	EW1284
Laser Diode Supply (positive polarity)	EW1291
Laser Diode Supply (negative polarity)	EW1206
DAVLL Sidelock Laser - Input Board	EW1303
Laser Diode Stabiliser	EW1225
Laser Diode Temperature Controller	EW1251

Table B.1: A summary of the circuits and part numbers made in Central Electronics.

Caesium Atomic Data and Experimental Equations

C.1 Atomic Parameters

Name	Symbol	Value	Unit
Resistivity	ρ_E	1.72×10^{-8}	$\Omega \text{ m}$
Density	ρ	8920	kg m^{-3}
Specific heat of copper	C	3.9×10^2	$\text{J kg}^{-1} \text{ K}^{-1}$
Specific heat of water	C	4.2×10^3	$\text{J kg}^{-1} \text{ K}^{-1}$
Wavelength	λ	852	nm
Natural linewidth of $6\text{P}_{3/2}$	Γ	$2\pi \times 5.22$	MHz
Saturation intensity for $6\text{S}_{1/2} 4, 4 \rangle \rightarrow 6\text{P}_{3/2} 5, 5 \rangle$	I_S	1.1	mW cm^2
Nuclear Spin	I	7/2	
* Nuclear Gyromagnetic Ratio	g_I	0.00039885395(52)	
† Electron Gyromagnetic Ratio	g_J	2.0023193043718(75)	
Ground State Hyperfine Splitting	ν_{HFS}	9.192631770×10^9	GHz

Table C.1: * and † constants obtained from Reference [128] and [129] respectively.

C.2 Magnetic Field Calculations

The on-axis field produced by a single coil of radius R is given by:

$$B_z = \frac{\mu_0}{2} \frac{nIR^2}{(A^2 + R^2)^{\frac{3}{2}}} \quad (\text{C.1})$$

where n is the number of turns, I is the magnitude of the current flowing through the coil, and A is the distance along the axis of the coil from the centre

The field gradient for a pair of coils in an anti-Helmholtz arrangement with radius R and separation $2A$ is given by:

$$\left. \frac{\partial B}{\partial z} \right|_{z=0} = \frac{3nIR^2A\mu_0}{(A^2 + R^2)^{\frac{5}{2}}} \quad (\text{C.2})$$

For the experimental setup described in the thesis, Table C.2 states all the relevant parameters of the quadrupole and shim coils.

	Number of Turns	Dimensions (cm)	Separation / Distance from atoms (cm)	B (G cm ⁻¹)
Pyramid Quad	15	R = 5.6	2A = 5	0.51 G/cm/A
Pyramid Shim	100	R = 7.8	A = 10	1.87 G/A
2nd MOT Quad	80	R = 2.5	2A = 7	4.48 G/cm/A
2nd MOT Shim	50	R = 18	A = 9	1.25 G/A

Table C.2: A summary of the magnetic coil parameters on the experiment

C.3 Number of Atoms

The number of atoms in a MOT can be calculated from the fluorescence measurement [68]. A summary of the required equations are given below.

The power radiated by an atom in a MOT is given by:

$$P_{\text{at}} = \frac{\hbar\omega_L\Gamma}{2} \frac{C_1^2\Omega_{\text{tot}}^2/2}{\delta^2 + \Gamma^2/4 + C_2^2\Omega_{\text{tot}}^2/2} \quad (\text{C.3})$$

where

$$\Omega_{\text{tot}}^2 = \frac{\Gamma^2}{2} \frac{I}{I_s} \quad (\text{C.4})$$

The constants C_1 and C_2 are determined experimentally [68]:

$$C_1^2 = C_2^2 = 0.73(10)$$

Substituting Equation C.4 into Equation C.3 yields the result:

$$P_{\text{at}} = \frac{\hbar\omega_L\Gamma}{2} \frac{C_1^2 I / I_s}{1 + C_2^2 I / I_s + 4\delta^2 / \Gamma^2} \quad (\text{C.5})$$

The power incident on the photodiode is:¹

$$P = NP_{\text{at}} \frac{\Omega}{4\pi} \quad (\text{C.6})$$

where Ω is the solid angle subtended by the collection lens and is equal to

$$\frac{\pi d^2}{4x^2} \quad (\text{C.7})$$

d is the diameter of the collection lens and x is the distance from the atoms to the collection lens.

The light incident on the photodiode gives rise to a signal S given by:

$$S(V) = PR(\lambda)R_{\text{load}} \quad (\text{C.8})$$

where $R(\lambda)$ is the responsivity of the photodiode and R_{load} is the load resistance.

Combining Equations C.7 and C.8, we obtain the following expression for N:

$$N = \frac{S(V)}{R(\lambda)R_{\text{load}}} \frac{16x^2}{d^2} \frac{1}{P_{\text{at}}} \quad (\text{C.9})$$

where P_{at} is as stated in Equation C.5.

¹Due to the limited solid angle of the collection optics the power incident on the photodiode is a fraction of the actual power radiated by the atoms.

Bibliography

- [1] M. H. ANDERSON, J. R. ENSHER, M. R. MATTHEWS, C. E. WIEMAN, AND E. A. CORNELL, “Observation of Bose-Einstein condensation in a dilute atomic vapor”, *Science* **269**, 198 (1995).
- [2] K. B. DAVIS, M.-O. MEWES, M. R. ANDREWS, N. J. VAN DRUTEN, D. S. DURFEE, D. M. KURN, AND W. KETTERLE, “Bose-Einstein condensation in a gas of sodium atoms”, *Phys. Rev. Lett.* **75**, 3969 (1995).
- [3] C. C. BRADLEY, C. A. SACKETT, J. J. TOLLETT, AND R. G. HULET, “Evidence of Bose-Einstein condensation in an atomic gas with attractive interactions”, *Phys. Rev. Lett.* **75**, 1687 (1995), *ibid.* **79**, 1170 (1997).
- [4] S. L. CORNISH, N. R. CLAUSSEN, J. L. ROBERTS, E. A. CORNELL, AND C. E. WIEMAN, “Stable ^{85}Rb Bose-Einstein condensates with widely tunable interactions”, *Phys. Rev. Lett.* **85**, 1795 (2000).
- [5] S. JOCHIM, M. BARTENSTEIN, A. ALTMAYER, G. HENDL, S. RIEDL, C. CHIN, J. H. DENSCHLAG, AND R. GRIMM, “Bose-Einstein condensation of molecules”, *Science* **302**, 2101 (2003).
- [6] M. ZWIERLEIN, C. STAN, C. SCHUNK, S. RAUPACH, S. GUPTA, Z. HADZIBABIC, AND W. KETTERLE, “Observation of Bose-Einstein condensation of molecules”, *Phys. Rev. Lett.* **91**, 250401 (2003).
- [7] D. FRIED, T. KILLIAN, L. WILLMANN, D. LANDHUIS, S. MOSS, D. KLEPPNER, AND T. GREYTAK, “Bose-Einstein condensation of atomic hydrogen”, *Phys. Rev. Lett.* **81**, 3811 (1998).

-
- [8] A. ROBERT, O. SIRJEAN, A. BROWAEYS, J. POUPARD, S. NOWAK, D. BOIRON, C. I. WESTBROOK, AND A. ASPECT, “A Bose-Einstein condensate of metastable atoms”, *Science* **292**, 461 (2001).
- [9] F. P. D. SANTOS *et al.*, “Bose-Einstein condensation of metastable helium”, *Phys. Rev. Lett.* **86**, 3459 (2001).
- [10] G. MODUGNO, G. FERRARI, G. ROATI, R. J. BRECHA, A. SIMONI, AND M. INGUSCIO, “Bose-Einstein condensation of potassium atoms by sympathetic cooling”, *Science* **294**, 1320 (2001).
- [11] C. REGAL, M. GREINER, AND D. JIN, “Observation of resonance condensation of fermionic atom pairs”, *Phys. Rev. Lett.* **92**, 040403 (2004).
- [12] T. WEBER, J. HERBIG, M. MARK, H.-C. NÄGERL, AND R. GRIMM, “Bose-Einstein condensation of cesium”, *Science* **299**, 232 (2003).
- [13] S. BOSE, “Plancks Gesetz und Lichtquantenhypothese”, *Z. Phys.* **26**, 178 (1924).
- [14] A. EINSTEIN, “Quantentheorie des einatomigen idealen Gases. Zweite Abhandlung”, *Sitzungber. Preuss. Akad. Wiss.* **1925**, 3 (1925).
- [15] M.-O. MEWES, M. R. ANDREWS, D. M. KURN, D. S. DURFEE, C. G. TOWNSEND, AND W. KETTERLE, “Output coupler for Bose-Einstein condensed atoms”, *Phys. Rev. Lett.* **78**, 582 (1997).
- [16] S. INOUE, M. R. ANDREWS, J. STENGER, H.-J. MIESNER, D. M. STAMPER-KURN, AND W. KETTERLE, “Observation of Feshbach resonances in a Bose-Einstein condensate”, *Nature* **392**, 151 (1998).
- [17] J. L. ROBERTS, N. R. CLAUSSEN, S. L. CORNISH, E. A. DONLEY, E. A. CORNELL, AND C. E. WIEMAN, “Controlled collapse of a Bose-Einstein condensate”, *Phys. Rev. Lett.* **86**, 4211 (2001).

-
- [18] E. DONLEY, N. CLAUSSEN, S. CORNISH, J. ROBERTS, E. CORNELL, AND C. WIEMAN, “Dynamics of collapsing and exploding Bose-Einstein condensates”, *Nature* **412**, 295 (2001).
- [19] E. DONLEY, N. CLAUSSEN, S. THOMPSON, AND C. WIEMAN, “Atom-molecule coherence in a Bose-Einstein condensate”, *Nature* **417**, 529 (2002).
- [20] M. GREINER, C. REGAL, AND D. JIN, “A molecular Bose-Einstein condensate emerges from a Fermi sea”, *Nature* **426**, 537 (2003).
- [21] K. GIBBLE AND S. CHU, “Future slow-atom frequency standards”, *Metrol.* **29**, 201 (1992).
- [22] P. JULIENNE AND F. MIES, “Collisions of ultracold trapped atoms”, *Phys. Rev. A* **6**, 2257 (1989).
- [23] E. TIESINGA, A. MOERDIJK, B. J. VERHAAR, AND H. T. C. STOOF, “Conditions for Bose-Einstein condensation in magnetically trapped atomic cesium”, *Phys. Rev. A* **46**, R1167 (1992).
- [24] J. SÖDING, D. GUÉRY-ODELIN, P. DESBIOLLES, G. FERRARI, AND J. DALIBARD, “Giant spin relaxation of an ultracold cesium gas”, *Phys. Rev. Lett.* **80**, 1869 (1998).
- [25] M. ARNDT, M. B. DAHAN, D. GUÉRY-ODELIN, M. W. REYNOLDS, AND J. DALIBARD, “Observation of a zero-energy resonance in Cs-Cs collisions”, *Phys. Rev. Lett.* **79**, 625 (1997).
- [26] P. BANCE, *Evaporative Cooling of Caesium in a TOP Trap: Prospects for BEC*, Ph.D. thesis, University of Oxford, 1998.
- [27] A. J. MOERDIJK AND B. J. VERHAAR, “Collisional two- and three-body decay rates of dilute quantum gases at ultralow temperatures”, *Phys. Rev. A* **53**, R19 (1996).

-
- [28] H. BOESTEN, A. MOERDIJK, AND B. VERHAAR, “Dipolar decay in two recent Bose-Einstein condensation experiments”, *Phys. Rev. A* **54**, R29 (1996).
- [29] C. J. MYATT, E. A. BURT, R. W. GHRIST, E. A. CORNELL, AND C. E. WIEMAN, “Production of two overlapping Bose-Einstein condensates by sympathetic cooling”, *Phys. Rev. Lett.* **78**, 586 (1997).
- [30] E. TIESINGA, B. J. VERHAAR, AND H. T. C. STOOF, “Threshold and resonance phenomena in ultracold ground-state collisions”, *Phys. Rev. A* **47**, 4114 (1993).
- [31] J. ARLT, P. BANCE, S. HOPKINS, J. MARTIN, S. WEBSTER, A. WILSON, K. ZETIE, AND C. J. FOOT, “Suppression of collisional loss from a magnetic trap”, *J. Phys. B* **31**, L321 (1998).
- [32] C. R. MONROE, E. A. CORNELL, C. A. SACKETT, C. J. MYATT, AND C. E. WIEMAN, “Measurement of Cs-Cs elastic scattering at $T = 30\mu\text{K}$ ”, *Phys. Rev. Lett.* **70**, 414 (1993).
- [33] D. GUERY-ODELIN, J. SODING, P. DESBIOLLES, AND J. DALIBARD, “Strong evaporative cooling of a trapped cesium gas”, *Opt. Express* **2**, 323 (1998).
- [34] O. LUITEN, M. REYNOLDS, AND J. WALRAVEN, “Kinetic theory of the evaporative cooling of a trapped gas”, *Phys. Rev. A* **53**, 381 (1996).
- [35] D. GUÉRY-ODELIN, J. SÖDING, P. DESBIOLLES, AND J. DALIBARD, “Is Bose-Einstein condensation of atomic cesium possible?”, *Europhys. Lett.* **44**, 26 (1998).
- [36] S. J. J. M. F. KOKKELMANS, B. J. VERHAAR, AND K. GIBBLE, “Prospects for Bose-Einstein condensation in cesium”, *Phys. Rev. Lett.* **81**, 951 (1998).
- [37] P. LEO, C. WILLIAMS, AND P. JULIENNE, “Collision properties of ultracold ^{133}Cs atoms”, *Phys. Rev. Lett.* **85**, 2721 (2000).

-
- [38] C. CHIN, V. VULETIĆ, A. KERMAN, AND S. CHU, “High resolution Feshbach spectroscopy of cesium”, *Phys. Rev. Lett.* **85**, 2717 (2000).
- [39] H. PERRIN, A. KUHN, I. BOUCHOULE, T. PFAU, AND C. SALOMON, “Raman cooling of spin-polarized cesium atoms in a crossed dipole trap”, *Europhys. Lett.* **46**, 141 (1999).
- [40] A. KERMAN, V. VULETIĆ, C. CHIN, AND S. CHU, “Beyond optical molasses: 3D Raman sideband cooling of atomic cesium to high phase-space density”, *Phys. Rev. Lett.* **84**, 439 (2000).
- [41] D. HAN, M. DEPUE, AND D. WEISS, “Loading and compressing Cs atoms in a very far-off-resonant light trap”, *Phys. Rev. A* **63**, 023405 (2001).
- [42] M. HAMMES, D. RYCHTARIK, V. DRUZHININA, U. MOSLENER, I. MANEK-HÖNNINGER, AND R. GRIMM, “Optical and evaporative cooling of caesium atoms in the gravito-optical surface trap”, *Journal of Modern Optics* **47**, 2755 (2000).
- [43] Y. CASTIN, J. I. CIRAC, AND M. LEWENSTEIN, “Reabsorption of light by trapped atoms”, *Phys. Rev. Lett.* **80**, 5305 (1998).
- [44] Y. B. OVCHINNIKOV, I. MANEK, AND R. GRIMM, “Surface trap for Cs atoms based on evanescent-wave cooling”, *Phys. Rev. Lett.* **79**, 2225 (1997).
- [45] Y. B. OVCHINNIKOV, S. SHUL’GA, AND V. BALYKIN, “An atomic trap based on evanescent light waves”, *J. Phys. B: At. Mol. Opt. Phys.* **24**, 3173 (1991).
- [46] P. W. H. PINKSE, A. MOSK, M. WEIDEMÜLLER, M. W. REYNOLDS, T. W. HIJMANS, AND J. T. M. WALRAVEN, “One-dimensional evaporative cooling of magnetically trapped atomic hydrogen”, *Phys. Rev. A* **57**, 4747 (1998).

-
- [47] A. DEREVIANKO, W. JOHNSON, M. SAFRONOVA, AND J. BABB, “High-precision calculations of dispersion coefficients, static dipole polarizabilities, and atom–wall interaction constants for alkali–metal atoms”, *Phys. Rev. Lett.* **82**, 3589 (1999).
- [48] F. MIES, C. WILLIAMS, P. JULIENNE, AND M. KRAUSS, “Estimating bounds on collisional relaxation rates of spin-polarized ^{87}Rb atoms at ultra-cold temperatures”, *J. Res. Natl. Inst. Stand. Tech.* **101**, 521 (1996).
- [49] P. LEO, E. TIESINGA, P. JULIENNE, D. WALTER, S. KADLECEK, AND T. WALKER, “Elastic and inelastic collisions of cold spin-polarized ^{133}Cs atoms”, *Phys. Rev. Lett.* **81**, 1389 (1998).
- [50] P. Julienne and co-workers at NIST Gaithersburg, *Private communication*.
- [51] A. THOMAS, S. HOPKINS, S. CORNISH, AND C. FOOT, “Strong evaporative cooling towards Bose-Einstein condensation of a magnetically trapped caesium gas”, *J. Opt. B: Quantum Semiclass. Opt.* **5**, S107 (2003).
- [52] Z.-Y. MA, A. THOMAS, C. FOOT, AND S. CORNISH, “The evaporative cooling of a gas of caesium atoms in the hydrodynamic regime”, *J. Phys. B* **36**, 3533 (2003).
- [53] W. KETTERLE, K. DAVIS, M. JOFFE, A. MARTIN, AND D. PRITCHARD, “High densities of cold atoms in a *dark* spontaneous-force optical trap”, *Phys. Rev. Lett.* **70**, 2253 (1993).
- [54] S. CHU, J. E. BJORKHOLM, A. ASHKIN, AND A. CABLE, “Experimental observation of optically trapped atoms”, *Phys. Rev. Lett.* **57**, 314 (1986).
- [55] R. GRIMM, M. WEIDEMÜLLER, AND Y. OVCHINNIKOV, “Optical dipole traps for neutral atoms”, *Adv. At. Mol. Opt. Phys.* **42**, 95 (2000).
- [56] W. KETTERLE AND D. PRITCHARD, “Atom cooling by time-dependent potentials”, *Phys. Rev. A* **46**, 4051 (1992).

-
- [57] T. W. HÄNSCH AND A. L. SCHAWLOW, “Cooling of gases by laser radiation”, *Opt. Commun.* **13**, 68 (1975).
- [58] S. CHU, L. HOLLBERG, J. BJORKHOLM, A. CABLE, AND A. ASHKIN, “Three-dimensional viscous confinement and cooling of atoms by resonance radiation pressure”, *Phys. Rev. Lett.* **55**, 48 (1985).
- [59] J. PRODAN AND W. PHILLIPS, “Chirping the light fantastic - recent NBS atom cooling experiments”, *Prog. Quant. Elect.* **8**, 231 (1984).
- [60] W. ERTMER, R. BLATT, J. L. HALL, AND M. ZHU, “Laser manipulation of atomic beam velocities: Demonstration of stopped atoms and velocity reversal”, *Phys. Rev. Lett.* **54**, 996 (1985).
- [61] R. WATTS AND C. WIEMAN, “Manipulating atomic velocities using diode lasers”, *Opt. Lett.* **11**, 291 (1986).
- [62] V. S. BAGNATO, G. P. LAFYATIS, A. G. MARTIN, E. L. RAAB, R. N. AHMAD-BITAR, AND D. E. PRITCHARD, “Continuous stopping and trapping of neutral atoms”, *Phys. Rev. Lett.* **58**, 2194 (1987).
- [63] W. PHILLIPS AND H. METCALF, “Laser deceleration of an atomic beam”, *Phys. Rev. Lett.* **48**, 596 (1982).
- [64] P. LETT, W. PHILLIPS, S. ROLSTON, C. TANNER, R. WATTS, AND C. WESTBROOK, “Optical molasses”, *J. Opt. Soc. Am. B* **6**, 2084 (1989).
- [65] J. DALIBARD AND C. COHEN-TANNOUJDI, “Laser cooling below the Doppler limit by polarization gradients: simple theoretical models”, *J. Opt. Soc. Am. B* **6**, 2023 (1989).
- [66] E. L. RAAB, M. PRENTISS, A. CABLE, S. CHU, AND D. E. PRITCHARD, “Trapping of neutral sodium atoms with radiation pressure”, *Phys. Rev. Lett.* **59**, 2631 (1987).

-
- [67] K. LINDQUIST, M. STEPHENS, AND C. WIEMAN, “Experimental and theoretical study of the vapor-cell Zeeman optical trap”, *Phys. Rev. A* **46**, 4082 (1992).
- [68] C. G. TOWNSEND *et al.*, “Phase-space density in the magneto-optical trap”, *Phys. Rev. A* **52**, 1423 (1995).
- [69] C. G. TOWNSEND, N. H. EDWARDS, K. P. ZETIE, C. J. COOPER, J. RINK, AND C. J. FOOT, “High-density trapping of cesium atoms in a dark magneto-optical trap”, *Phys. Rev. A* **53**, 1702 (1996).
- [70] C. MONROE, W. SWANN, H. ROBINSON, AND C. WIEMAN, “Very cold trapped atoms in a vapor cell”, *Phys. Rev. Lett.* **65**, 1571 (1990).
- [71] F. SHIMIZU, K. SHIMIZU, AND H. TAKUMA, “Four-beam laser trap of neutral atoms”, *Opt. Lett.* **16**, 339 (1991).
- [72] K. LEE, J. KIM, H. NOH, AND W. JHE, “Single-beam atom trap in a pyramidal and conical hollow mirror”, *Opt. Lett.* **21**, 1177 (1996).
- [73] J. REICHEL, W. HÄNSEL, AND T. HÄNSCH, “Atomic micromanipulation with magnetic surface traps”, *Phys. Rev. Lett.* **83**, 3398 (1999).
- [74] J. ARLT, O. MARAGÒ, S. WEBSTER, S. HOPKINS, AND C. FOOT, “A pyramidal magneto-optical trap as a source of slow atoms”, *Opt. Comm.* **157**, 303 (1998).
- [75] E. FISCHER, “The three dimensional stabilizing of charge particles in a quadropole field”, *Zeitschrift fur Physik* **156**, 1 (1959).
- [76] A. L. MIGDALL, J. V. PRODAN, W. D. PHILLIPS, T. H. BERGEMAN, AND H. J. METCALF, “First observation of magnetically trapped neutral atoms”, *Phys. Rev. Lett.* **54**, 2596 (1985).
- [77] W. WING, “On neutral particle trapping in quasistatic electromagnetic fields”, *Prog. Quant. Elec.* **8**, 181 (1984).

-
- [78] G. BREIT AND I. RABI, “Measurement of nuclear spin”, *Phys. Rev.* **38**, 2082 (1931).
- [79] E. MAJORANA, “Atomi orientati in campo magnetico variabile”, *Nuovo Cimento* **9**, 43 (1932).
- [80] W. PETRICH, M. ANDERSON, J. ENSHER, AND E. CORNELL, “Stable, tightly confining magnetic trap for evaporative cooling of neutral atoms”, *Phys. Rev. Lett.* **74**, 3352 (1995).
- [81] T. BERGEMAN, G. EREZ, AND H. METCALF, “Magnetostatic trapping fields for neutral atoms”, *Phys. Rev. A* **35**, 1535 (1987).
- [82] J. ROBERTS, *Bose-Einstein Condensates with Tunable Atom-atom Interactions: The first experiments with ^{85}Rb BECs*, Ph.D. thesis, University of Colorado, 2001.
- [83] M.-O. MEWES, M. R. ANDREWS, N. J. VAN DRUTEN, D. M. KURN, D. S. DURFEE, AND W. KETTERLE, “Bose-Einstein condensation in a tightly confining dc magnetic trap”, *Phys. Rev. Lett.* **77**, 416 (1996).
- [84] H. METCALF AND P. VAN DER STRATEN, *Laser Cooling and Trapping* (Springer, 1999).
- [85] H. F. HESS, “Evaporative cooling of magnetically trapped and compressed spin-polarized hydrogen”, *Phys. Rev. B* **34**, 3476 (1986).
- [86] N. MASUHARA, J. DOYLE, J. SANDBERG, D. KLEPPNER, T. GREYTAK, H. HESS, AND G. KOCHANSKI, “Evaporative cooling of spin-polarized atomic hydrogen”, *Phys. Rev. Lett.* **61**, 935 (1988).
- [87] K. DAVIS, M. MEWES, M. JOFFE, AND W. KETTERLE, in *Fourteenth International Conference on Atomic Physics (ICAP XIV)*, EDITED BY D. WINELAND, C. WIEMAN, AND S. SMITH (Springer-Verlag, 1994), Book of Abstracts, 1M–3.

-
- [88] W. PETRICH, M. ANDERSON, J. ENSHER, AND E. CORNELL, in *Fourteenth International Conference on Atomic Physics (ICAP XIV)*, EDITED BY D. WINELAND, C. WIEMAN, AND S. SMITH (Springer-Verlag, 1994), Book of Abstracts, 1M-7.
- [89] J. DOYLE, J. SANDBERG, I. YU, C. CESAR, D. KLEPPNER, AND T. GREYTAK, “Hydrogen in the submillikelvin regime: Sticking probability on superfluid ^4He ”, *Phys. Rev. Lett.* **67**, 603 (1991).
- [90] O. J. LUITEN, H. G. C. WERIJ, I. D. SETIJA, M. W. REYNOLDS, T. W. HIJMANS, AND J. T. M. WALRAVEN, “Lyman- α spectroscopy of magnetically trapped atomic hydrogen”, *Phys. Rev. Lett.* **70**, 544 (1993).
- [91] I. SETIJA, H. WERIJ, O. LUITEN, M. REYNOLDS, T. HIJMANS, AND J. WALRAVEN, “Optical cooling of atomic hydrogen in a magnetic trap”, *Phys. Rev. Lett.* **70**, 2257 (1993).
- [92] K. DAVIS, M.-O. MEWES, M. JOFFE, M. ANDREWS, AND W. KETTERLE, “Evaporative cooling of sodium atoms”, *Phys. Rev. Lett.* **74**, 5202 (1995).
- [93] B. DESRUELLE, V. BOYER, S. G. MURDOCH, G. DELANNOY, P. BOUYER, AND A. ASPECT, “Interrupted evaporative cooling of ^{87}Rb atoms trapped in a high magnetic field”, *Phys. Rev. A* **60**, R1759 (1999).
- [94] E. SURKOV, J. WALRAVEN, AND G. SHLYAPNIKOV, “Collisionless motion and evaporative cooling of atoms in magnetic traps”, *Phys. Rev. A* **53**, 3403 (1996).
- [95] D. Manolopoulos, “Quantum Scattering Dynamics” lecture notes, <http://physchem.ox.ac.uk/mano/>.
- [96] C. PETHICK AND H. SMITH, *Bose-Einstein Condensation in Dilute Gases* (Cambridge, 2002).

-
- [97] R. FEYNMAN, R. LEIGHTON, AND M. SANDS, *The Feynman Lectures on Physics, Vol. III* (Addison-Wesley Publishing, Reading, Massachusetts, 1965).
- [98] R. NEWTON, “Analytic properties of radial wave functions”, *J. Math. Phys.* **1**, 319 (1960).
- [99] C. RAMSAUER, “Über den wirkungsquerschnitt der gasmoleküle gegenüber langsamen elektronen”, *Ann. d. Physik* **64**, 513 (1921).
- [100] J. TOWNSEND AND V. BAILEY, “The motion of electrons in argon”, *Philos. Mag.* **43**, 593 (1922).
- [101] A. KERMAN, *Raman Sideband Cooling and Cold Atomic Collisions in Optical Lattices*, Ph.D. thesis, University of Stanford, 2002.
- [102] J. ROBERTS, N. CLAUSSEN, J. BURKE JR., C. GREENE, E. CORNELL, AND C. WIEMAN, “Resonant magnetic field control of elastic scattering of cold ^{85}Rb ”, *Phys. Rev. Lett.* **81**, 5109 (1998).
- [103] A. MARTE, T. VOLZ, J. SCHUSTER, S. DÜRR, G. REMPE, E. VAN KEMPEN, AND B. VERHAAR, “Feshbach resonances in rubidium 87: Precision measurement and analysis”, *Phys. Rev. Lett.* **89**, 283202 (2002).
- [104] M. HOUBIERS, H. T. C. STOOF, W. I. MCALEXANDER, AND R. G. HULET, “Elastic and inelastic collisions of Li-6 atoms in magnetic and optical traps”, *Phys. Rev. A* **57**, R1497 (1998).
- [105] K. O’HARA, S. HEMMER, S. GRANADE, M. GEHM, J. THOMAS, V. VENTURI, E. TIESINGA, AND C. WILLIAMS, “Measurement of the zero crossing in a Feshbach resonance of fermionic ^6Li ”, *Phys. Rev. A* **66**, 041401(R) (2002).
- [106] T. LOFTUS, C. A. REGAL, C. TICKNOR, J. L. BOHN, AND D. S. JIN, “Resonant control of elastic collisions in an optically trapped Fermi gas of atoms”, *Phys. Rev. Lett.* **88**, 173201 (2002).

-
- [107] H. WU AND C. FOOT, “Direct simulation of evaporative cooling”, *J. Phys. B* **29**, L321 (1996).
- [108] M. HOLLAND, J. WILLIAMS, K. COAKLEY, AND J. COOPER, “Trajectory simulation of kinetic equations for classical systems”, *Quantum Semiclass. Opt.* **8**, 571 (1996).
- [109] H. WU, E. ARIMONDO, AND C. FOOT, “Dynamics of evaporative cooling for Bose-Einstein condensation”, *Phys. Rev. A* **56**, 560 (1997).
- [110] C. A. SACKETT, C. C. BRADLEY, AND R. G. HULET, “Optimization of evaporative cooling”, *Phys. Rev. A* **55**, 3797 (1997).
- [111] W. KETTERLE, M. R. ANDREWS, K. B. DAVIS, D. S. DURFEE, D. M. KURN, M.-O. MEWES, AND N. J. VAN DRUTEN, “Bose-Einstein condensation of ultracold atomic gases”, *Phys. Scr.* **T66**, 31 (1996).
- [112] L. LANDAU AND E. LIFSHITZ, *Mechanics*, 3rd Ed. (Pergamon Press, Oxford, 1976).
- [113] J. DOYLE, J. SANDBERG, I. YU, C. CESAR, D. KLEPPNER, AND T. GREYTAK, “Evaporative cooling of atomic hydrogen: Theory of cooling and progress towards the Bose-Einstein transition”, *Physica B* **194-196**, 13 (1994).
- [114] G. BIRD, *Molecular Gas Dynamics and the Direct Simulation of Gas Flows* (Oxford: Oxford Science Publications, 1998).
- [115] T. WEBER, J. HERBIG, M. MARK, H.-C. NÄGERL, AND R. GRIMM, “Three-body recombination at large scattering lengths in an ultracold atomic gas”, *Phys. Rev. Lett.* **91**, 123201 (2003).
- [116] C. WIEMAN AND L. HOLLBERG, “Using diode lasers for atomic physics”, *Rev. Sci. Instrum.* **62**, 1 (1991).

-
- [117] K. B. MACADAM, A. STEINBACH, AND C. WIEMAN, “A narrow band tunable diode laser system with grating feedback, and a saturated absorption spectrometer for Cs and Rb”, *Am. J. Phys.* **60**, 1098 (1992).
- [118] W. DEMTRÖDER, *Laser Spectroscopy* (Springer-Verlag, New York, 1996).
- [119] K. CORWIN, Z.-T. LU, C. HAND, J. EPSTEIN, AND C. WIEMAN, “Frequency-stabilized diode laser with the zeeman shift in an atomic vapor”, *Appl. Opt.* **37**, 3295 (1998).
- [120] The Labview control program was written by M. Büchner and S.L. Cornish with modifications by A.M. Thomas.
- [121] C. CHIN, *Cooling, Collisions and Coherence of Cold Cesium Atoms in a Trap*, Ph.D. thesis, Stanford University, 2001.
- [122] K. B. DAVIS, M.-O. MEWES, AND W. KETTERLE, “An analytical model for evaporative cooling of atoms”, *Appl. Phys. B* **60**, 155 (1995).
- [123] V. BOYER, S. MURDOCH, Y. L. COQ, G. DELANNOY, P. BOUYER, AND A. ASPECT, “Multifrequency evaporative cooling to Bose-Einstein condensation in a high magnetic field”, *Phys. Rev. A* **62**, 021601(R) (2000).
- [124] The simulation was written by Z.-Y. Ma and S.L. Cornish.
- [125] P. O. FEDICHEV, Y. KAGAN, G. V. SHLYAPNIKOV, AND J. T. M. WALRAVEN, “Influence of nearly resonant light on the scattering length in low-temperature atomic gases”, *Phys. Rev. Lett.* **77**, 2913 (1996).
- [126] P. W. H. PINKSE, A. MOSK, M. WEIDEMÜLLER, M. W. REYNOLDS, T. W. HIJMANS, AND J. T. M. WALRAVEN, “Adiabatically changing the phase-space density of a trapped Bose gas”, *Phys. Rev. Lett.* **78**, 990 (1997).
- [127] D. M. STAMPER-KURN, H.-J. MIESNER, A. P. CHIKKATUR, S. INOUE, J. STENGER, AND W. KETTERLE, “Reversible formation of a Bose-Einstein condensate”, *Phys. Rev. Lett.* **81**, 2194 (1998).

-
- [128] E. ARIMONDO, M. INGUSCIO, AND P. VIOLINO, “Experimental determinations of the hyperfine structure in the alkali atoms”, *Rev. Mod. Phys.* **49**, 31 (1977).
- [129] <http://physics.nist.gov/cuu/constants/index.html>.